Sea Grant Program on Marine Corrosion
FINAL REPORT

Volume Two — Calcareous Deposits

Edited by
S. C. Dexter
and
W. H. Hartt

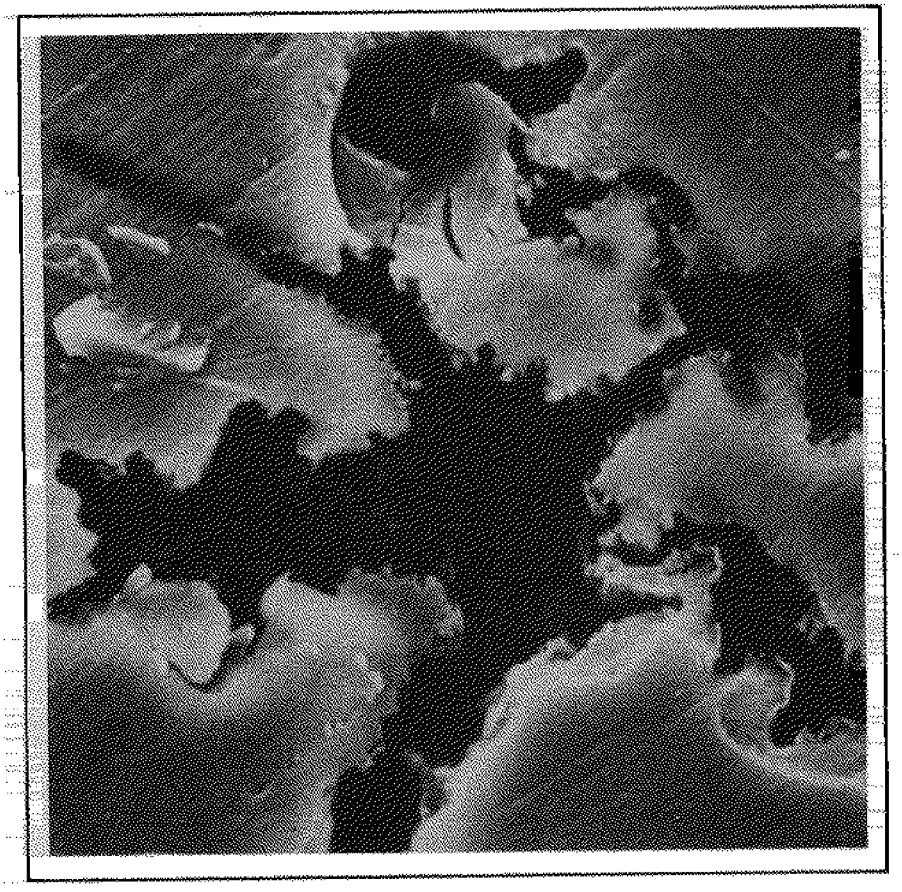

Submitted to
THE OFFICE OF SEA GRANT PROGRAMS
NATIONAL OCEANIC AND ATMOSPHERIC ADMINISTRATION
UNITED STATES DEPARTMENT OF COMMERCE

JUNE 1987
UNIVERSITY OF DELAWARE
Sea Grant College Program
LEWES, DELAWARE 19958

SEA GRANT PROGRAM ON MARINE CORROSION
FINAL REPORT

VOLUME TWO--CALCAREOUS DEPOSITS

submitted to

The Office of Sea Grant Programs
National Oceanic and Atmospheric Administration
United States Department of Commerce

Overall Program Leader:
Stephen C. Dexter
University of Delaware

Calcareous Deposits Principal Investigators:
William H. Hartt
Florida Atlantic University
Project Leader

Charles H. Culberson
University of Delaware

Samuel W. Smith
Florida Atlantic University

June 1987
University of Delaware
Sea Grant College Program
Lewes, Delaware 19958
DEL-SG-13-87

PREFACE

The Sea Grant Program on Marine Corrosion began in the fall of 1980 as a cooperative research project involving eight principal investigators from both academia and industry. An important component of the Program has been establishment of an Industrial Advisory Panel, whose primary functions were to keep the investigators aware of developing industrial problems in the area of marine corrosion and to assist the investigators in technology transfer. The Program was to last for three years and was viewed by both the National Sea Grant Office and by the investigators themselves as an experiment in forging closer ties between a substantial academic research effort and its ultimate beneficiaries in industry.

The overall report consists of four volumes and serves (1) to document the technical results from the three years of research by the eight principal investigators and their associates and students, (2) to evaluate the success of the Program and (3) to determine whether the structure of the Program should be continued and perhaps used as a model in other fields of research.

The present volume (Volume II) of the overall report is a stand-alone document which summarizes the experiments and experimental results of this program in the area of calcareous deposits. Volume I, on the other hand, is a summary and evaluation for the overall program, whereas Volumes III and IV address corrosion of aluminum alloys and stainless steels, respectively.

Stephen C. Dexter
Overall Program Leader

Sea Grant Program on

Marine Corrosion

FINAL REPORT

Table of Contents

PREFACE

VOLUME TWO Calcareous Deposits

EXECUTIVE SUMMARY

The efficiency and effectiveness of cathodic protection for marine service is in most instances predicated upon formation of calcareous deposits. At the same time relatively little is known about the fundamental nature of these surface films and the dependence of properties and protective character upon conditions and variable of formation. For this reason it was considered timely that an investigation of calcareous deposits be undertaken.

The research plan involved four principal investigators at three institutions with most experiments focusing upon relatively small carbon steel specimens. Three different facets of calcareous deposits were investigated, which were (1) nature and properties (2) influences upon fatigue and (3) modeling. For the first of these the occurrence and nature of calcareous deposits was assessed by cathodic polarization to the potential of interest and monitoring the current density change with time and as a function of variable of interest, including potential, flow state and temperature. In the second category an initial model has been developed for predicting the occurrence of calcareous deposit induced crack closure. With regard to the latter an initial model has been developed which predicts cathodic current density trends with time as a consequence of the calcareous deposit formation process. Based upon the data and associated analyses conclusions hve been reached regarding the properties of calcareous deposits which form under a given set of experimental conditions, and these are discussed within a perspective of present and future marine cathodic protection practice.

I. INTRODUCTION

I.A. Project Goals and Objectives.

For structures such as ships, port facilities, pipelines, offshore structures and others exposed to open sea water, accepted techniques for corrosion control include 1) proper design, 2) proper materials selection, 3) coatings and 4) cathodic protection. In a large number of applications, steel has been judged to be the most economically effective material of construction; and on this basis the most widely employed corrosion prevention technique for the submerged zone is cathodic protection. Despite the importance of cathodic protection to maintaining marine systems, relatively little fundamental research attention has been devoted to this topic. The present research project was undertaken for the purpose of contributing to our understanding of this important aspect of marine engineering and coeering and corrosion control.

A unique feature of cathodic protection in sea water, as compared to other electrolytes, is development of a calcareous deposit upon the metal surface. Such a surface film contributes to the effectiveness and efficiency of marine cathodic protection systems (Humble, 1948; LaQue, 1950; Doremus, et al, 1967; Compton, 1975; LaQue, 1975). However, while the importance of calcareous deposits is generally recognized, relatively few research efforts have been undertaken for the express purpose of studying these films per se. That information which has developed has often been piecemeal and incomplete. In view of this it is timely that a comprehensive investigation of calcareous deposits which form on cathodic surfaces in sea water be undertaken. It was with this perspective in mind that the present research was undertaken. Specific objectives include the following:

1. To better understand the fundamental properties of calcareous deposits including their chemistry, structure, formation rate and effective resistance, as a function of electrochemical, chemical and physical variables of exposure. Such variables include current density and potential, pH, temperature, sea water chemistry and hydrodynamic flow characteristics.

2. To investigate preferential formation of calcareous deposits within corrosion fatigue cracks in cathodically protected structural steel and to determine how such deposit occurrence might contribute to enhanced structural reliability and safety for situations involving dynamic loadings in sea water.

3. To investigate techniques for mathematical modeling of the potential and current density history of steel surfaces upon which calcareous deposits form.

I.B. Background Information.

For most cathodic surfaces in aerated waters the principal reduction reaction is

$$\tfrac{1}{2}O_2 + H_2O + 2e^- \rightarrow 2OH^- \qquad (I.1$$

In cases where potential is more negative than the reversible hydrogen electrode a second reaction

$$2H_2O + 2e^- \rightarrow H_2 + 2OH^- \qquad (I.2$$

also occurs. In either case the result is an increase in pH for the electrolyte adjacent to the metal surface due to the production of hydroxyl ions. Alternately, an increase in $[OH^-]$ is equivalent to a corresponding reduction in $[H^+]$. This situation is represented schematically in Figure I.1, where the pH immediate to the metal-electrolyte interface is determined

by the rate of hydroxyl ion production and by removal due to diffusion or convection or both. Temperature, relative electrolyte velocity and electrolyte composition should influence this pH profile.

There is both analytical and experimental evidence that such a pH increase exists as a consequence of a cathodic current. For example, Engell et al (1965) projected pH at the surface of cathodically protected steel in sea water to be 10.9. Similarly, Wolfson and et al (1981) calculated values ranging from 10.75 to 11.25 based upon parameters of their research. Experimental verification has been provided by Kobayashi (1972) who applied a cathodic current of 0.938 mA/cm^2 to steel in an unstirred 3% NaCl solution of bulk pH 8 and measured pH 0.1 mm. from the surface to be 11.5.

In sea water pH is controlled by the carbon dioxide system, as expressed by the following reactions:

$$CO_2 + H_2O \rightarrow H_2CO_3 \qquad \text{(I.3}$$

$$H_2CO_3 \rightarrow H^+ + HCO_3^- \qquad \text{(I.4}$$

$$HCO_3^- \rightarrow H^+ + CO_3^-. \qquad \text{(I.5}$$

If OH^- is added to the system as a consequence, for example, of one of the above cathodic processes (see Equations I.1 and I.2), then the reactions

$$OH^- + HCO_3^- \rightarrow H_2O + CO_3^{-2} \quad \text{and} \qquad \text{(I.6}$$

$$CO_3^{-2} + Ca^{+2} \rightarrow CaCO_3(ppt) \qquad \text{(I.7}$$

are expected. The equilibria represented by Equations I.3-I.7 further indicate that as OH^- is introduced (Equation I.1 or I.2 or both) and reacts (Equation I.6) then Equations I.4 and I.5 are displaced to the right, resulting in proton production. This opposes any rise in pH and accounts for the buffering capacity of

sea water. Irrespective of this, however, Equations I.3-I.7 are responsible for calcareous deposits which form on cathodic surfaces in sea water.

It should not be inferred from Equation I.7 nor from the terminology "calcareous deposits" that the surface films in question here are comprised solely of calcium carbonate. Thus, the data in Table I.1 report the composition of calcareous deposits as reported by Humble (1948) and Hudson (1940) and reveal a significant magnesium ion content, particularly at higher current densities. The data suggest that this species is present primarily as $Mg(OH)_2$ but with some $MgCO_3$. These results may be rationalized in terms of established solubility limits and the major ion content of sea water.

Magnesium compounds, $Mg(OH)_2$ in particular, could also contribute to the protective character of calcareous deposits; but whereas calcium carbonate is thermodynamically stable in surface sea water (it is supersaturated) in the ambient pH range, magnesium hydroxide is unsaturated and, hence, not stable. Only when the pH of sea water exceeds approximately 9.5 should $Mg(OH)_2$ precipitate (Smith, 1981).

On the other hand, calcium carbonate occurs in the oceans in two crystalline forms, calcite and aragonite. Due at least in part to the fact that calcite and magnesium carbonate have similar crystal structures, these compounds form solid solutions the Ca/Mg ratio of which depends upon the ratio of these same ions in sea water. Theoretical calculations (Barner, 1975 suggest that calcite in equilibrium with sea water should contain between 2 and 7 mole percent $MgCO_3$. This has been confirmed experimentally by Auger spectroscopy which revealed the surface layers of calcite crystals in sea water to contains 4 ± 2 mole percent $MgCO_3$ (Morse, 1979). This low magnesium calcite is the most stable solid calcium carbonate phase in sea water, and its solubility is approximately 22 percent less than for pure calcite in sea water (Morse, et al, 1980).

Although low magnesium calcite is the most stable carbonate phase in sea water, its precipitation (Pytkowicz, 1973) and crystal growth (Pytkowicz, 1965) are strongly inhibited by dissolved magnesium. Consequently, aragonite is the phase which actually precipitates when sea water is made basic by addition of sodium carbonate (Pytkowicz, 1965). Pytkowicz (1973) has shown that although magnesium slows the nucleation of aragonite, it does not prevent it as is the case with calcite. However, once aragonite nuclei form, magnesium does not affect further growth. It has been demonstrated that oceanic levels of phosphate inhibit both nucleation (Pytkowicz, 1973) and crystal growth (Berner, 1978) of aragonite. In addition, various organic compounds inhibit aragonite precipitation in sea water (Pytkowicz, 1973; Berner, 1978; Chave, et al., 1970).

The behavior of $CaCO_3$ in sea water has been extensively studied because carbonate sediments are widespread in the oceans. Magnesium hydroxide is so soluble that it does not occur in marine sediments; consequently its solubility, kinetics and composition have not been broadly investigated. The most accurate solubility data for $Mg(OH)_2$ were measured in carbonate free synthetic sea water (Pytkowicz, et al, 1968; Gates, 1969). Solubilities in natural sea water containing carbonate have been found to be greater (Wattenberg, et al, 1938; Pytkowicz, et al, 1966), apparently due to coprecipitation of carbonate and hydroxide phases. Platform (1965) studied the precipitation of $Mg(OH)_2$ for carbonate free synthetic sea water and found that twelve-fold supersaturation is required for precipitation of this phase.

Only limited solubility measurement information is available regarding $MgCO_3$ and $SrCO_3$ (Wattenberg, et al, 1938). As these measurements were performed in natural sea water (containing calcium) and since $CaCO_3$ is much less soluble than either $MgCO_3$ or $SrCO_3$ the data may have been affected by coprecipitation of several different carbonates and, therefore, may not be representative of pure $MgCO_3$ or $SrCO_3$.

The degree of saturation of carbonate and hydroxide phases in the oceans depends on physical properties such as temperature, pressure and salinity, which control the solubility product of the solid phase, and on oceanic pH which is primarily controlled by the concentration of dissolved inorganic carbon, as was discussed above in conjunction with Equations I.3-I.5. This parameter (degree of saturation of a solid phase) may be represented by the ratio of the ion product (the product of the actual, in situ concentrations) to the solubility product of the solid phase. Thus, for aragonite the degree of saturation is

$$\Omega_{aragonite} = \frac{(Ca^{+2})_{sw}(CO_3^{-2}{}_{sw}}{K_{sp(aragonite)}}, \qquad (I.8$$

where $(Ca^{+2})_{sw}$ and $(CO^{-2})_{sw}$ are the measured calcium and carbonate concentrations in sea water and K_{sp} (aragonite) is the solubility product for aragonite at the temperature, pressure, and salinity of the sea water sample. A degree of saturation less than unity means sea water is undersaturated with the solid phase and a value greater than unity indicates supersaturation. Notice that the ion product, $Ca^{+2}{}_{sw}$ $(CO^{-2})_{sw}$, is the same for both calcite and aragonite. The degree of saturation for these two calcium carbonate phases differs only in the solubility product for the two solids. For the case of calcite Ω is always greater than for aragonite, because the solubility product of the former is less than that of the latter. Table I.2 lists selected values for the solubility product of calcite, aragonite, magnesium hydroxide, magnesium carbonate, and strontium carbonate in sea water as a function of temperature and pressure at 35 o/oo salinity. Data at other salinities may be found in the original papers. In Figure I.2 the degree of saturation for aragonite and calcite at a location in the North Atlantic and North Pacific Ocean is plotted. Thus, both aragonite and calcite are undersaturated at depth, as higher pressure and lower pH increase

their solubilities. More extensive calculations for the entire oceans (Ingle, 1975) show that calcite and aragonite are supersaturated everywhere in the surface oceans.

While a pressure increase alone results in a decrease in pH, the trend for sea water to become less basic with increasing depth is further compounded by the influence of additional factors upon inorganic carbon concentration. These include air-sea exchange, photosynthesis and solution and precipitation of calcium carbonate (Dexter, et al, 1980). For example, in surface sea water photosynthesis tends to consume CO_2 during the production of organic matter according to the generalized reaction

$$CO_2 + H_2O \rightarrow CH_2O + O_2. \qquad \text{(I.9}$$

This contributes to a lowering of $[CO_2]$ and to a corresponding pH increase to about 8.1. From the standpoint of thermodynamics this should result in precipitation of $CaCO_3$, but as discussed previously this is blocked by magnesium ions. As organisms die and sink they tend to be broken down by bacteria which utilize the organic compounds for respiration by the reverse reaction in Equation I.9. In conjunction with Equations I.3-I.5, this tends to lower pH and result in the dissolution of calcium carbonate. Thus,

$$CaCO_3 + H_2CO_3 \rightarrow Ca^{+2} + 2HCO_3^- \qquad \text{(I.10}$$

I.C. Fatigue and Calcareous Deposits.

Fatigue of steel in sea water has been judged to be a failure mode that may be critical to the integrity and reliability of numerous types of marine structural systems, including ships and offshore structures. Corrosion technology has evolved over the past several decades to the point that such structures are typically outfitted with a cathodic protection system. Hence, any study of fatigue, as applicable to structural

marine systems, should necessarily address the influence of cathodic polarization, with potentials of interest ranging from the freely corroding value to overprotection.

Hudgins, et al (1971) were apparently the first to consider that calcareous deposits might have a beneficial effect upon fatigue of steel in synthetic sea water, although no directly applicable experimental data was obtained to substantiate this. Using compact tension specimens fatigued to sea water, Scott (1978) observed for load control tests with positive R, that the maximum crack opening per cycle remained relatively invariant with time, whereas the minimum value progressively increased. He attributed this to calcareous deposit formation within the crack and influence of this matter upon crack closure. The fact that lowering of fatigue crack growth rate typically accompanied this was explained in terms of a reduced effective stress intensity range. Similarly, Royer (1978) has observed either a reduction or arrestment of crack propagation in compact tension specimens in sea water in response to potentiostatic control at an increasingly negative potential.

Hooper et al (1978) and Hartt, et al (1980) considered that calcareous deposits which formed within cracks of notched 1018 specimens fatigued in natural sea water were responsible for "endurance limit enhancement," where for a range of cathodic potentials the fatigue limit was approximately two times greater in sea water than in air. This behavior also was attributed to formation of calcareous deposits within cracks and to a corresponding reduction in stress intensity range.

It may be reasoned, based upon the above information, that corrosion fatigue cracking of structural steel in sea water or synthetic sea water under conditions of cathodic protection should not be a problem. However, reduction or elimination of fatigue crack propagation has not been observed universally. More commonly, fatigue crack growth rate is unchanged or slightly reduced for modest amounts of cathodic polarization ($\phi \approx$ -0.80v., SCE) but is enhanced progressively with further decrease in potential (Scott, et al, 1977). This latter trend has also

been observed in NaCl solutions (Vosikovsky, 1976). Apparently, a calcareous deposit which influences fatigue crack growth rate occurs only under certain conditions; and what these conditions are has not yet been defined.

Formation of calcareous deposits within fatigue cracks of steel cathodically polarized in sea water indicates that the occluded cell (crack) electrolyte pH increases relative to that of the bulk. It is generally recognized that chemistry of the electrolyte within local cells can become modified relative to the bulk solution. This results because both convective and diffusional interchange between the two (bulk and occluded cell electrolytes) are restricted due to geometric factors. Corrosion rate within crevices, pits, intergranular paths, filiforms, tuberculations, exfoliations and cracks have been rationalized in terms of localized pH modification (Brown, 1970). For the case of exposure in a near-neutral chloride solution under freely corroding or anodically polarized conditions pH of the occluded cell electrolyte for most metals becomes acidic. Local pH has been shown to increase progressively, however, with increasing cathodic current density and at sufficiently high values to exceed that of the bulk solution (Pourbaix, 1970; Peterson, et al, 1973). The potential dependence of static stress crack growth rate has been interpreted in terms of these local chemistry changes (Brown, 1970).

With regard to corrosion fatigue, it may be argued that the alternate opening and closing of the crack faces may result in a pumping action which should preclude crack electrolyte modification. On the other hand, if one considers the static tension case as simply one extreme of the frequency spectrum, then it may be reasoned that modification should occur for corrosion fatigue also, provided frequency is not excessive. Whether or not the electrolyte within a corrosion fatigue crack becomes distinct in comparison to the bulk is important, since development of calcareous deposits and crack propagation rate should depend upon solution chemistry in this region.

Several observations in the literature, in addition to those reported earlier for the specific case of cathodically polarized steel in sea water, support the projection that electrolyte chemistry modification can occur within corrosion fatigue cracks. For example, Barsom (1971) measured pH of such electrolyte to be about three for a 12Ni-5Co-3Mo steel cycled at 0.1 Hz in a near-neutral 3% NaCl - distilled water solution. Similarly, Meyn (1971) reported a pH or less than three for the crack electrolyte of Ti-8Al-1Mo-1V specimens fatigued at both 0.5 and 30 Hz.

In addition the observation (Hartt, et al, 1980) that under certain conditions of fatigue of steel in sea water calcareous deposits formed more profusely within the crack than on the bulk surface suggests that pH within the crack can become more alkaline than for the bulk electrolyte adjacent to the freely exposed surface. An example of this is presented in Figure I.3. Apparently, an important factor is the extent of crack electrolyte-bulk electrolyte mixing on each cycle as the former is sequentially ejected and ingested. Situations where this interchange is minimal are expected to promote a shift in pH for the crack electrolyte and thereby contribute to local calcareous deposit formation.

An initial analysis of the mixing of these electrolytes which takes place on each cycle has been performed by considering that only convective interchange is important and that this occurs in proportion to momentum of the ejected-ingested electrolyte (Hartt, et al, 1978). Thus, it was found that

$$J = (\rho a^3 \beta \omega^2/4) \{\cos^2\omega t/\sin\omega t + \alpha_0/\beta)\}dt, \qquad (I.11$$

where

J = net electrolyte momentum,

ρ = solution density,

a = crack length,

β = half angular range of crack opening,

ω = cyclic frequency,

α_0 = mean crack opening angle and

t = time.

On this basis the extent of mixing was projected to increase with the cube of crack length, with decreasing mean stress and with decreasing frequency. Other factors which were deemed important but whose role is not indicated by Equation I.11 include temperature, stress wave form, specimen geometry and test method.

How formation of a crack growth inhibiting calcareous deposit is influenced by mixing, cathodic current density, crack geometry and by mechanical fatigue variables is presently not known; however, this point could be important to the control and mitigation of this mode of failure as it may occur in marine structures.

I.D. Critical Assessment of Calcareous Deposits.

Table I.3 is intended to diagram the task of rationalizing the nature of calcareous deposits. Thus, the ultimate goal is to understand the properties of deposits (film thickness, porosity, etc.) and to rationalize these in terms of deposit structure and chemistry, as dictated by the nucleation and growth kinetics of their formation. These, in turn, are a consequence of the influential variables, which are listed in terms of five categories -

1. potential/current/time
2. temperature and pressure
3. sea water chemistry
4. relative motion or water velocity
5. substrate surface condition

The subsequent discussion considers these topics individually and reviews past investigations which have been performed within each category.

I.D.1. Potential/Current/Time. Polarization of an electrode in aerated water to a specified cathodic potential is invariably accompanied by oxygen concentration polarization, such that current density decreases with exposure time. In sea water or other aqueous electrolytes containing an adequate concentration

of certain inorganic ions (Ca^{++}, Mg^{++}, HCO^{-} etc., as discussed above) deposition of calcareous matter may accompany this polarization. This, in turn, compounds the extent of oxygen concentration polarization. Figure I.4 presents a typical current density decay plot for three carbon steel specimens polarized to -0.78, -0.93 and -1.03v. SCE, respectively, as reported by Wolfson et al (1981). Note that the current density after 100 hours is in some instances an order of magnitude less than the initial value. This reduction is attributed, at least in part, to build-up of calcareous deposits on the metal surface.

Limited information regarding the effectiveness of calcareous deposits in restricting oxygen access to a steel surface has been provided by Rodrigo (1966), as reported in Figure I.5. Here, the minimum current density for cathodic protection is indicated for both a 3% NaCl solution and natural sea water as a function of dissolved oxygen concentration. The interdependence between these two parameters conforms to a straight line in both cases; however, for the former electrolyte (3% NaCl) the slope is approximately 2.5 times greater than for the latter. This data further suggests that under conditions of air saturation, approximately 7 mg/l 0_2 (temperature of the experiment is assumed to be ambient), approximately 50% less current was required to polarize the steel in sea water than in 3% NaCl. While this data was obtained under short term, laboratory conditions and may not necessarily reflect longer duration, field exposures, still the economic implications are significant, since this current density reduction in the presence of calcareous deposits implies that half as many anodes would be required compared to an exposure that does not involve calcareous deposits.

It is generally recognized that for a given set of experiment conditions (constant temperature, electrolyte velocity, etc. and allowing for time dependent concentration polarization effects) that a singular relationship exists between potential and current. However, in the case of calcareous deposits extended exposure times may be required to achieve

steady state; and so it is appropriate that both potential and current be treated as independent variables. This is particularly true in view of the fact that a deposit formed under one set of conditions may have different properties and, hence, promote a different current density decay response than one formed under an alternative circumstance. Note, for instance, the data in Figure 4 where the initial ordering of current densities was in proportion to the magnitude of cathodic polarization, as should be anticipated. Also, the current density decay for the initial ten hours of exposure was approximately the same for all three potentials. Subsequently, however, the decay rate for the -1.03v. specimen increased, leading to current densities which after thirty hours were less than for -0.93v. This same behavior was apparent as well for nominal velocities of 30 and 107 cm/sec. Presumably, some property of the calcareous deposit formed at the most negative potential was unique in comparison to the two other potentials, and this upset what might otherwise be a common potential-current density relationship for the three specimens. No explanation has been developed for this behavior, although it is probably due to greater specific resistivity of the -1.03v. deposit as a consequence of some aspect of its chemistry or structure or both.

LaQue (1975) considered that calcareous deposits were responsible for enhanced polarization with time of steel coupled to a magnesium anode. Figure I.6 illustrates this, where potential has been plotted versus distance from the center of the steel plate (location of anode) for four exposure times. The behavior exemplified in this figure is largely responsible for the extensive "throwing power" of cathodic protection systems in sea water, where after a period of time potential is more uniform and cathodic than might be anticipated for other electrolytes, fresh water for example.

The experiments of Humble (1948) are illustrative with regard to how deposit chemistry and properties depend upon the magnitude of cathodic current. He exposed steel panels galvanically coupled to magnesium anodes for one year at Kure

Beach, N. C., under constant current conditions. Table I.1 reported the results of deposit chemical analysis and indicated that the major compounds comprising these films are $CaCO_3$, $MgCO_3$ and $Mg(OH)_2$. This data also indicates that the concentration of certain ions (Na^+, Si^{+4} and Cl^- was relatively independent of current density in the range investigated, whereas for others (Fe^{+2}, CO^{-2}, Mg^{+2}, Sr^{+2}, and OH^-) a trend was apparent. The decrease in iron ion concentration with increasing current density probably reflects reduced corrosion rate of the steel as a function of an increasingly cathodic potential. In the case of the other ions, however, the variations may reflect important trends which are a consequence of electrolyte chemistry modification, increased pH in particular, adjacent to the metal surface due to the cathodic current. Humble attached particular significance to the Ca/Mg ratio of the deposit and how this varied with current density. The data from Table I.1 pertaining to this ratio are plotted in Figure I.7. The trend of decreasing Ca/Mg ratio with increasing current density is probably related to the fact that the calcium ion is supersaturated at ambient surface sea water pH, but precipitation of $Mg(OH)_2$ requires that pH be greater than 9.5. Thus, increasing concentration of the latter compound should be facilitated at higher current densities, as discussed in the preceding section.

While the strontium ion concentrations listed by Humble (1948) approximate the amount of this species typically present in sea water, Strasburg (1981) has reported that calcareous deposits removed from the sonar cavity of various Navy ships operating between the U.S. west coast and Africa contained several weight percent of this ion. The reason for the relatively large distinction in strontium concentration between these two analyses is not clear; however, Humble has pointed out that the solubility products and ionic concentrations of sea water are such that with increasing pH $CaCO_3$ should precipitate first followed sequentially by $SrCO_3$, $MgCO_3$ and $Mg(OH)_2$. Hence, deposits of high Sr concentration, relative to sea water, are not unanticipated.

While no effort has been undertaken to investigate the structure of calcareous deposits, Hilbertz (1976) has performed x-ray analysis on acretions formed for structural purposes. These involved current densities much greater than are typically employed for cathodic protection. This revealed the structure to be that of aragonite, which is consistent with earlier comments regarding the inhibiting effect of magnesium in sea water upon calcite formation (Morse, et al, 1980; Chave, et al, 1970).

Humble (1948) noted that deposits formed at lower current densities were more "permanent" than ones at higher current densities, and he attributed th is to the lower solubility of Ca^{+2} as opposed to Mg^{+2}. This has been illustrated by an experiment reported by Cox (1950) which involved alternative immersion of specimens polarized by a prescribed constant cathodic current density. The results are reported in Figure I.8, where it is seen that no rusting was apparent when cathodic current density was in the range 0.07 - 0.3 mA/cm^2 (70-300 mA/ft^2). Thus, the surface film formed under these conditions provided protection even during the portion of the experiment when the specimen was out of water. The relative amounts of $CaCO_3$ and $Mg(OH)_2$ as reported by Humble (1948), are plotted for reference. An explanation for this behavior has been offered where calcareous deposits were considered to be particularly cementitious when $CaCO_3$ and $Mg(OH)_2$ are present in approximately equal amounts (Cox, 1950). On the other hand, the reduced protection afforded by deposits at current densities greater than 0.3 mA/cm^2 has been attributed to inherently poor coating properties of $Mg(OH)_2$. This may be due to dissolution of $Mg(OH)_2$ under conditions of zero current, as discussed earlier. Such dissolution could be particularly important with regard to periods when the current output of a cathodic protection system is interrupted. Alternately, coating detachment due to hydrogen evolution at the metal-electrolyte interface could contribute. The lack of protection for current densities below 0.07 mA/cm^2 may be related to insufficient time for adequate deposit coverage.

A second experiment (Humble, 1948) which relates the protective character of calcareous deposits under freely corroding conditions is reported by Figure I.9. This involved two sets of specimens, one which was freely corroding in sea water for ten months and the second which was polarized by a cathodic current of 0.19 mA/cm^2 (175 mA/ft^2) for one day followed by ten months of free corrosion exposure. Even at the end of this period corrosion rate for the latter specimen set, presumably determined by weight loss data over the entire ten months, was approximately one-half of that for the former set. Hence, it would appear that calcareous deposits formed at this current density can be protective during prolonged subsequent periods of free corrosion. On the other hand it may be reasoned that corrosion cells could be set up on a freely corroding metal where the surface is partially covered by calcareous deposits, and caution should be exercised with regard to reaching broad conclusions based upon these limited experiments.

I.D.2. Temperature and Pressure. The fact that scaling occurs more rapidly at higher temperatures is well established. In all probability increased precipitation kinetics, as limited by some thermally activated step, is the rate controlling factor.

Limited data addressing the effect of temperature on calcareous deposits for steel exposed in sea water taken from the Port of Barcelona and cathodically polarized at constant cathodic current has been provided by Guillen et al (1966) Figures I.10 and I.11 confer two representations of their data as plots of weight gain (attributed to calcareous deposits) as a function of either temperature or cathodic current density under static exposure. The general trend apparent here is that the weight of calcareous deposit precipitated at 0, 20 and 40°C increased modestly with increasing temperature but that 30-40% more deposit formed at 60° than at 40°C. Consistent with this it is generally recognized by the cathodic protection industry that calcareous deposits form more readily upon metal surfaces in warm ocean waters than in cold, although other factors (water movement and water chemistry, for example) also may be influential.

In the preceding section pressure was mentioned as one factor which influences the degree of saturation for various inorganic compounds comprising calcareous deposits. Also, degree of saturation calculations as a function of water depth were reported (see Table I.2 and Figure I.2); and these data infer that a greater pH shift in the vicinity of the metal-electrolyte interface (higher cathodic current) may be necessary to form a given amount of calcareous deposit at depth than near the surface. It should not be construed, however, that this is a consequence of pressure per se but, instead, of an influence of pressure upon inorganic carbon concentration as represented by the equilibria in Equations I.3-I.5. Irrespective of this, Figure I.2 suggests that the properties of calcareous deposits as a function of depth may be expected to vary from one location to the next in the oceans. For example, the fact that $CaCO_3$ becomes undersaturated at shallower water depth in the Pacific as compared to the Atlantic Ocean could contribute to inherent chemistry differences between deposits formed at depths between 300 and 2500 m in these two locations.

I.D.3. Sea Water Chemistry. The structure and properties of calcareous deposits may be related to the chemistry of the sea water from which they precipitate. One example of this is apparent from earlier discussions where the fact that magnesium ions inhibit calcite formation was discussed, thereby contributing to supersaturation of sea water with $CaCO_3$ and to occurrence of solid $CaCO_3$ as aragonite.

The influence of electrolyte concentration upon calcareous deposits was investigated by Klas (1958) who cathodically polarized steel specimens in synthetic sea water of 1:16, 1:4 and 1:1 dilutions. The rate of current decay for the first several hundred hours exposure was more rapid in the full strength solution than in the diluted ones, where decay rate was approximately the same for the two experimental conditions. The Ca/Mg ratio for these deposits was found to decrease with increasing polarization, which is consistent with the results of Humble (1948). However, the value for this parameter was greater

in the diluted synthetic sea waters than in the full strength for steel polarized to -0.780v.(SCE) and less for polarization to -0.980v. or -1.080v. Other than this there was no apparent trend for current density variation as a function of electrolyte concentration. In some instances an apparent steady state current density was subsequently observed, while in other cases the decay continued for the duration of the experiment (1200 hours). These experiments are in qualitative agreement with those of Wolfson et al (1981) in that the long-term current density did not necessarily correlate with the magnitude of polarization.

Klas also measured electrical resistivity of the calcareous deposits which formed on his specimens as a function of exposure duration. Figure I.12 illustrates typical results in comparison to the corresponding current density-time behavior and reveals an inverse correlation between the two. While this result suggests that resistivity is the film property of significance, it is not clear how this interfaces with data (Wolfson et al, 1981) indicating that thickness of calcareous deposits increased linearly with time even during a period when cathodic current density to maintain a constant potential was invariant.

A particularly interesting facet of sea water chemistry which influences $CaCO_3$ precipitation pertains to the concentration of organic carbon. Thus, Chave et al (1970) increased pH of sea water samples obtained from various locations near Hawaii by addition of Na_2CO_3 and observed the subsequent pH decay which was due to $CaCO_3$ precipitation. Several samples from sea water aquaria were also employed because these contained relatively high organic carbon concentrations. Figure I.13 reports a typical pH decay curve and illustrates that the onset of $CaCO_3$ precipitation may be characterized by a break point. Figure I.14 plots this latter parameter as a function of organic carbon concentration of the sea water, and this reveals a pronounced inhibiting influence of the carbon. Chave et al attributed this behavior to absorption of the

organic carbon upon $CaCO_3$ nuclei. In open sea water organic carbon concentrations have been reported to be in the range of 0.4-3 mg/l (Riley, et al, 1971). Values may be greater in coastal locations. In view of this it appears that organic carbon concentration may be an influential factor with regard to the formation rate of calcareous deposits, and so experiments addressing these surface films should take this parameter into account.

I.D.4 Velocity. Increasing relative motion between a metal and electrolyte typically results in enhanced reactant availability and more rapid dissipation of products. This is a consequence of reduced thickness of the diffusion barrier adjacent to the metal surface. On this basis it may be reasoned that the magnitude of current density to maintain a prescribed cathodic potential on a film free surface should increase with increasing electrolyte velocity provided the cathodic reaction is under concentration polarization control, as is likely to be the case for steel in aerated sea water. Thus, Figure I.15 schematically depicts the pH profiles which are envisioned to result at a metal surface (film free) for a prescribed cathodic potential and at several different velocities. In conjunction with the preceding discussion, it may be rationalized that such variations could have a profound influence upon the chemistry, structure and properties of calcareous deposits. Experimental data which may indicate this have been reported by Guillen et al (1966), as represented in Figure I.16. Here the Ca/Mg ratio of calcareous deposits is reported for both aerated and static conditions and for four different temperatures. The data indicate that at all but the lowest temperature (0°C) Ca/Mg ratio was increased by aeration. The data of Humble (1948) have been included in Figure I.16 and are in general agreement with that of Gullen and Feliu despite the fact that experiments by the former author were for one year and the latter only 48 hours. Guillen and Feliu considered that the primary role of aeration was to produce electrolyte movement and thereby reduce thickness of the stagnant surface layer, and this apparently resulted in a film of

higher calcium content. On the basis of previous comments then the deposits formed under the aerated condition should be more protective than the static case. This may be offset by the finding that film thickness decreases with increasing velocity (Wolfson, et al, 1981), as illustrated by Figure I.17.

I.D.5. Metal Surface Condition. Investigations regarding this topic have been limited primarily to the influence of prior rusting upon corrosion of current density trends and upon subsequent cathodic protection. Thus, in the experiments of Klas (1958) which were discussed above, one set of tests was performed in full strength synthetic sea water employing specimens covered with rust, as well as specimens which were largely rust free. Figure I.18 reports these results as a plot of current density as a function of exposure time for three potentials. Distinctions between the two sets of data include 1) that the variation in apparent steady state current density for rusted specimens was small in comparison to specimens with little rust, and 2) that prior rusting resulted in a higher current density than for specimens with little rust at some potentials and at others the current density for rusted specimens was lower.

Experiments investigating this same topic have also been performed by Humble (1948) according to the same generalized experimental techniques outlined earlier. Thus, Figure I.19 reports weight loss versus current density data for sand-blasted steel specimens exposed to sea water for three and twelve month periods. Note that under the freely corroding circumstance approximately forty percent of the weight loss occurred during the initial three months, presumably as a consequence of increased oxygen availability prior to corrosion product development. With increasing cathodic current density, the percentage of weight loss which occurred in the first three months became greater and was approximately ninety percent for 0.011 mA/cm^2 (10 mA/ft^2). The latter reflects enhanced oxygen concentration polarization due to calcareous deposits.

Figure I.20 reports the results of an experiment (Humble, 1948) similar to that in Figure 1.19 but involving an initial three months free corrosion in all cases. The data indicate that a cathodic current in the range 0-0.011 mA/cm^2 for three months after this free corrosion resulted in only modest additional weight loss and with little current density dependence of corrosion. During a subsequent nine months exposure cathodic protection at the higher current densities (0.0008 and 0.011 mA/cm^2) was effective in reducing corrosion to a very low value. By comparison of Figures I.19 and I.20 it is apparent that application of a cathodic current density in the approximate range 0.005 - 0.011 mA/cm^2 to previously corroded specimens resulted in more rapid polarization than in the case of as sand-blasted plate. Presumably, this is a consequence of a protective surface film comprised of both rust and calcareous deposit. Detailed information regarding how initial surface condition, including the presence of corrosion products, influences formation and properties of calcareous deposits has not been developed, however.

I.E. Mathematical Modeling.

The present design approaches for cathodic protection systems usually involve rules of thumb developed from experience with similar structures and environments. Such rules can be misleading if applied to new conditions. Mathematical modeling of current and potential distributions on cathodically protected structures has been tried using analytical methods (Wagner, 1951; Waber et al, 1955; Kenard et al, 1970; McCaffety, 1977) finite difference methods (Doig et al, 1979; Strommen et al, 1981) boundary element methods (Fu et al, 1982; Danson et al, 1983) and finite methods (Brauer, 1979; Forrest et al, 1980; Munn, 1982 and 1983). The models that have been described in the open literature are quite limited in sophistication and value. It is clear that propriety programs are in use, especially by oil companies concerned with protecting offshore structures, but we can only guess about the nature of these.

A significant aspect of cathodic protection that has been neglected in published models is the formation of deposits on the cathodic surface. Generation of hydroxide ions at such surface leads, in sea water, to the deposition of an adherent solid precipitate composed largely of calcium carbonate and magnesium hydroxide, as described previously. This coating lowers the current density needed to achieve protection. Furthermore, since precipitation occurs most rapidly where current density is greatest, the deposits tend to even out or spread the current, leading to more efficient protection. Any realistic model of cathodic protection in sea water must include these phenomena.

Analytical solutions for current distribution during cathodic protection are only possible for a few situations in which a closed form solution of the LaPlace equation can be found. This can be accomplished for very simple geometries with uniform material properties and simple boundary conditions. For these reasons analytical solutions are mainly of academic interest.

Numerical methods making use of computers seem to be the only practical approach to modeling cathodic protection. In theory, the finite difference method should be able to deal with this problem quite well. In practice, however, the finite difference approach has not been used extensively and has been restricted to relatively simple models. Doig et al (1979) modeled the current distribution in the electrolyte above a galvanic couple to two dimensions. Strommen et al (1981), on the other hand, attempted a more ambitious model of an actual offshore structure using a finite difference technique. Even in this case, however, the boundary conditions were quite simplified.

The very flexible boundary element and finite element methods appear to be better suited to this kind of problem. The boundary element approach is still rather new but may turn out to be very powerful for modeling cathodic protection systems, since such modeling involves a linear governing equation, non-liner boundary conditions, complicated geometry and infinite domains.

Under these conditions the boundary element method tends to require less effort for data input and less computer time than the finite element method. Fu et al (1982) demonstrated the application of boundary element techniques to cathodic protection by modeling a 3-dimensional case using simple elements. Danson et al (1983) have used more sophisticated elements to model protection of North Sea structures. This model predicted "switch-on" current distribution, but the authors point out that it could be modified to predict changes over time. They suggest gathering data and using a curve fitting approach to predict the effects of scale accumulation on the structure.

The use of the finite element method to model cathodic protection systems has been described by several authors but Munn (1983) has used the most up-to-date approach. He employed the sophisticated MARC program, which includes a heat-transfer option that can be used to model current flow. Current input at boundaries can be made an arbitrary function of potential. He can, therefore, model only the electrolyte, relegating complex polarization behavior to his boundary-value functions. Thus, Munn (1982) has described application of his model to a simple laboratory galvanic couple and also to an actual Navy test platform (Munn, 1983) with useful results. This author does not address the problem of changes in cathodic behavior over time due to formation of calcareous deposits, but this program may well be a suitable tool for modeling such behavior.

I.F. BIBLIOGRAPHY (Section I)

R. A. Berner, Geochim. Cosmochim. Acta, Vol. 39, p. 489 (1975).

R. A. Berner, Am. J. Sci., Vol. 278, p. 816 (1978).

J. R. Brauer, "Analysis of Electric Currents in Cathodic Protection Systems," MSC/NASTRAN Users' Conference, March. 1979.

K. E. Chave and E. Suess, Limnol. Oceanogr., Vol. 15, p. 633 (1970).

K. G. Compton, "Cathodic Protection of Structures in Sea Water," Paper no. 13 presented at CORROSION 75, April 14-18, 1975, Toronto.

G. C. Cox, quoted by F. L. LaQue, Corrosion J., Vol. 6, p. 161 (1950).

D. J. Danson, and M. A. Warne, "Current Density/Voltage Calculations Using Boundary Element Techniques." Paper no. 211 presented at Corrosion/83, April 18-22, 1983, Anaheim.

S. E. Dexter and C. Culberson, Materials Performance, Vol. 19, p. 16 (1980).

P. Doig and P. E. J. Flewitt, J. Electrochemcial Society, Vol. 126, p. 2057 (1979).

G. L. Doremus and J. G. Davis, Materials Protection, Vol. 6(1), p. 30 (1967).

H. Engell and P.Forchhammer, Cor. Sci, Vol. 5, p. 479 (1965).

A. W. Forrest, J. W. Fu and R. T. Bicicchi, "Validation of Finite Element Technique for Modeling Cathodic Protection Systems." Paper no. 150 presented at CORROSION 80, March 3-7, 1980, Chicago.

J. W. Fu and J. S. K. Chow, "Cathodic Protection Designs Using an Integral Equation Method," Paper no. 163 presented at CORROSION 82, March 22-26, 1982, Houston.

R. F. Gates, "Magnesium Sulfate Ion Association in Sea Water," M. S. Thesis, Oregon State University, Corvallis, 1969, 39 pages.

M. A. Guillen and S. Feliu, Revista de Metallurgia, Vol. 2, p. 519 (1966).

W. H. Hilbertz, "Electrodeposition of Minerals in Solution and Its Enhancement by Biological Growth for Structural Applications," Sea Grant Report No. 04-6-158-4111, U. of Texas, 1976.

J. C. Hudson, The Corrosion of Iron and Steel, Van Nostrand Co., Inc., New York, 1940, pp. 158 and 175.

R. A. Humble, Corrosion Journal, Vol. 4, p. 358 (1948).

S. E. Ingle, Mar. Chem., Vol. 3, p. 301 (1975).

E. Kenard, J. T. Waber, J. Electrochemical Soc., Vol. 117, p. 880 (1970).

H. Klas, Archiv fur das Eisenhuttenwesen, Vol. 29, p. 321 (1958).

T. Koboyashi, Proc. Fifth Intl. Congress on Metallic Corrosion, p. 629 (1972).

F. L. LaQue, Corrosion Journal, Vol. 6, p. 161 (1950).

F. L. LaQue, Marine Corrosion: Causes and Prevention, J. Wiley and Sons, New York, 1975, p. 107.

E. McCafferty, "Mathematical Analysis of Circular Corrosion Cells Having Unequal Polarization Parameters," Naval Research Laboratory Report No. 8107, August, 1977.

J. W. Morse, Science, Vol. 205, p. 904 (1979).

J. W. Morse, A. Mucci and F. J. Millero, Geochim. Cosmochim. Acta, Vol. 44, p. 85 (1980).

R. S. Munn, Materials Performance Vol. 21 (8) p. 29 (1982).

R. S. Munn, "Corrosion Analysis and Cathodic Protection System Design for a Navy Measurements Platform Barge Using the Finite Element Method." Paper no. 212, presented at CORROSION 83, April 18-22, 1983, Anaheim.

R. F. Platford, J. Fish. Res. Bd. Canada, Vol. 22, p. 113 (1965).

R. M. Pytkowicz, J. Geology, Vol. 73, p. 196 (1965).

R. M. Pytkowicz, I. W. Duedall and D. N. Connors, Science, Vol. 152, p. 640 (1966).

R. M. Pytowicz, and R. Gates, Science, Vol. 161, p. 690 (1968).

R. M. Pytkowicz, Am. J. Sci., Vol. 273, p. 515 (1973).

J. P. Riley and R. Chester, Introduction to Marine Chemistry, Academic Press, London, 1971.

M. A. G. Rodrigo, Afinidad, Vol. 23, p. 217 (1966).

S. W. Smith, Analysis of the Cathodic Behavior of Aluminum in Natural Sea Water by Surface Chemistry, SCD Thesis, MIT-WHOI Joint Program (1981).

W. A. Strassberg, Naval Ship Engineering Center, Wash., D. C. private communication, 1981.

R. Strommen, and A. Rodland, (1981) Materials Performance, Vol. 20, p. 15.

J. T. Waber, (1956) J. Electrochemical Society, Vol. 103, No. 10, p. 567.

C. J. Wagner, (1951) J. Electrochemical Society, Vol. 108, No. 6, p. 116.

H. Wattenberg and E. Timmerman, Kieler Meeresforschungen, Vol. 2, p. 81 (1938).

S. L. Wolfson and W. H. Hartt, Cor. J., Vol. 37, p. 70 (1981).

FIGURE CAPTIONS (Section I)

Figure I. 1: Schematic illustration of the pH profile in the electrolyte adjacent to a cathodically polarized metal surface.

Figure I. 2: Degree of saturation as a function of depth calcite and aragonite.

Figure I. 3: Photograph of 1018 steel specimen subsequent to fatigue in sea water. The crack, which initiated at the notch root and propagated across approximately one-third the specimen, is evidenced by the white calcareous material on the specimen face.

Figure I. 4: Decrease in current density for steel specimens cathodically polarized in sea water as a function of exposure time.

Figure I. 5: Current density to maintain a prescribed cathodic potential for steel polarized in NaCl and sea water as a function of oxygen concentration.

Figure I. 6: Potential of a steel plate exposed to sea water as a function of distance outward from a magnesium anode and for four different exposure times.

Figure I. 7: Plot of Ca/Mg ratio of calcareous deposits as a fucntion of current density.

Figure I. 8: Plot of percent of rusted surface for alternately immersed, cathodically protected steel and also of deposit chemistry as a function of current density.

Figure I.9: Plot of corrosion rate for steel in sea water. While (a) freely corroding and (b) cathodically polarized followed by free corrosion.

Figure I.10: Weight gain (attributed to calcareous deposits) as a function of temperature and for various current densities.

Figure I.11: Weight gain (attributed to calcareous deposits) as a function of current density for various temperatures.

Figure I.12: Plot of current density and film resistance for steel cathodically polarized in synthetic sea water.

Figure I.13: Example of pH decay of sea water sample with Na_2CO_3 addition. Note the occurrence of a "break point" which was attributed to $CaCO_3$ precipitation.

Figure I.14: Plot of time-to-break from pH decay plot (see Figure I.13) as a function of organic carbon concentration in sea water.

Figure I:15: Schematic representation of pH profiles near the surface of a film free cathodically polarized metal for the three water velocities.

Figure I.16: Ca/Mg ratio of calcareous deposits for both static and aerated cases as a function of current density and temperature.

Figure I.17: Plot of calcareous deposit film thickness as a function of nominal sea water velocity.

Figure I.18: Comparison of current density decay as a function of time for heavily and lightly rusted steel specimens polarized to various cathodic potentials in synthetic sea water.

Figure I.19: Weight loss versus cathodic current density for sand blasted steel specimens exposed for three months and for one year in sea water.

Figure I.20: Weight loss versus current density for steel specimens exposed to different periods of free corrosion and cathodic polarization.

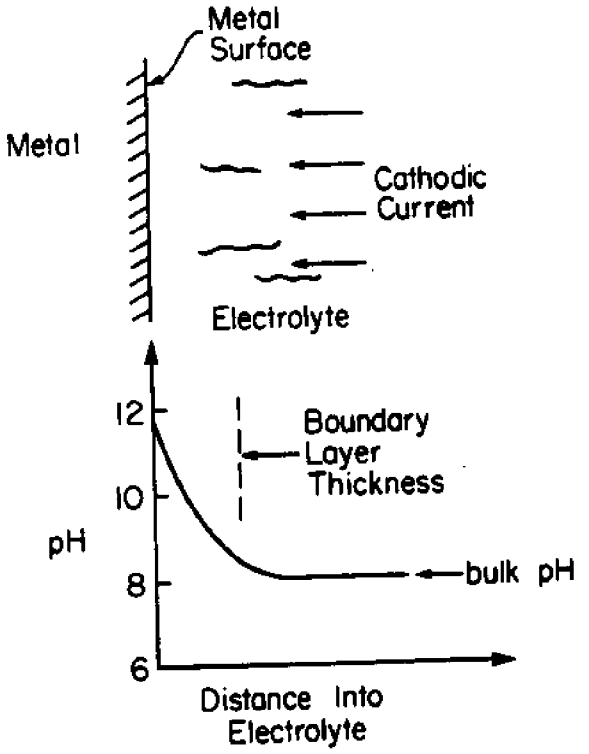

Figure I.1

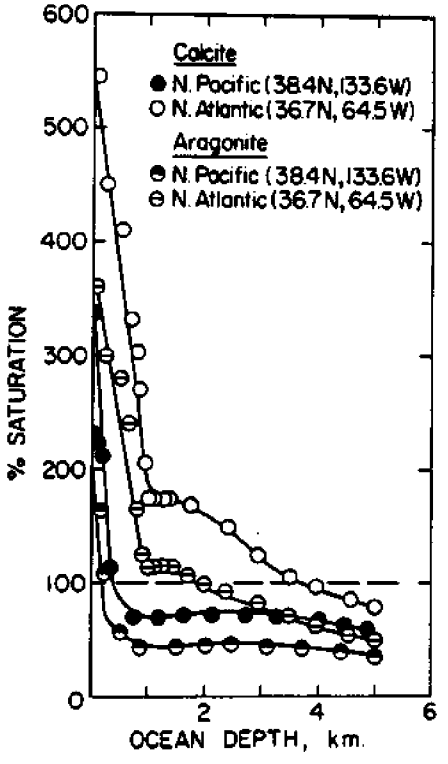

Figure I.2

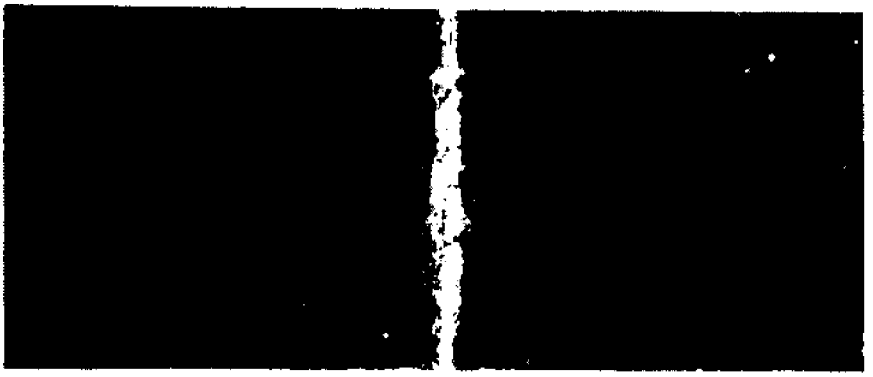

Figure I.3 "Top View"

Figure I.3 "Side View"

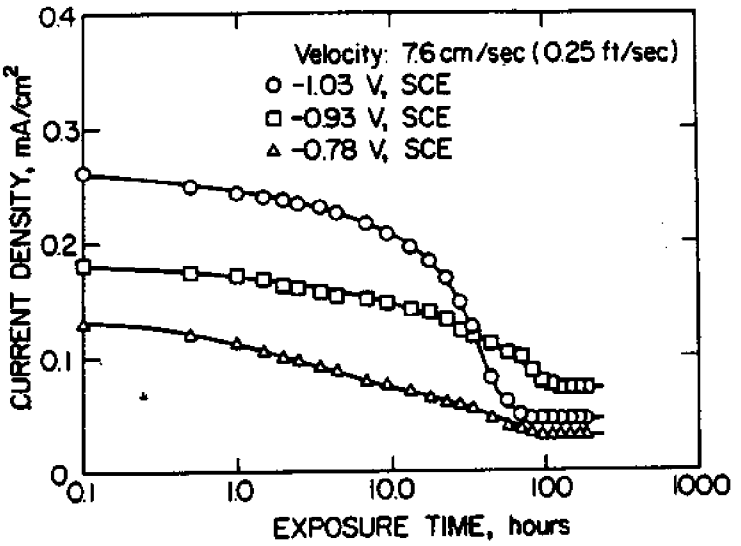

Figure I.4

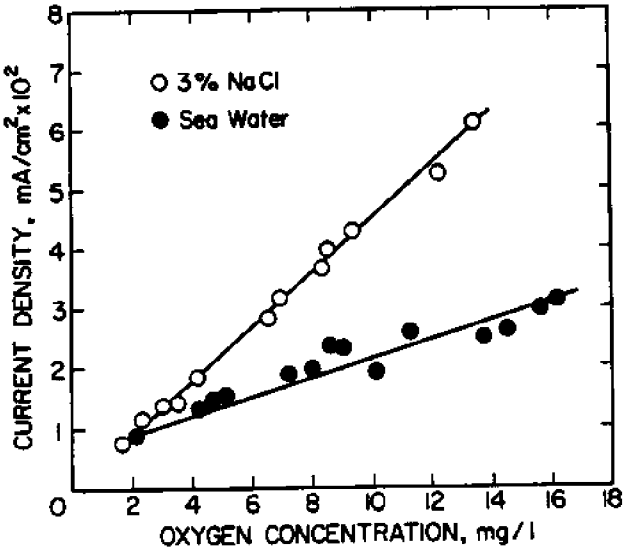

Figure I.5

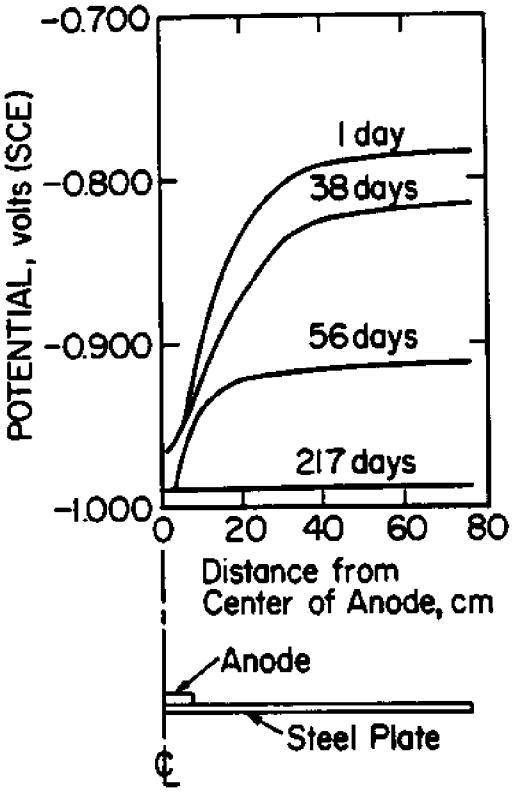

Figure I.6

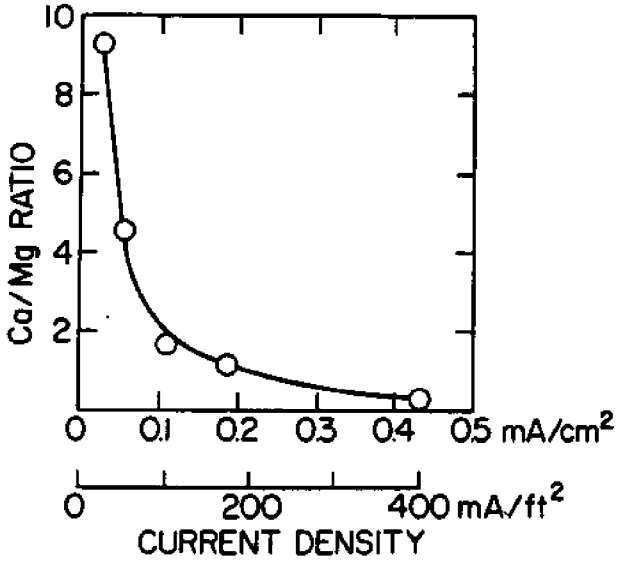

Figure I.7

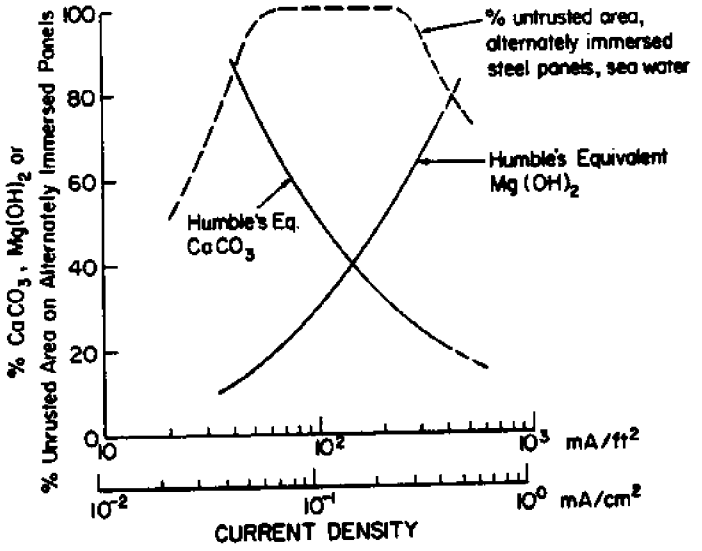

Figure I.8

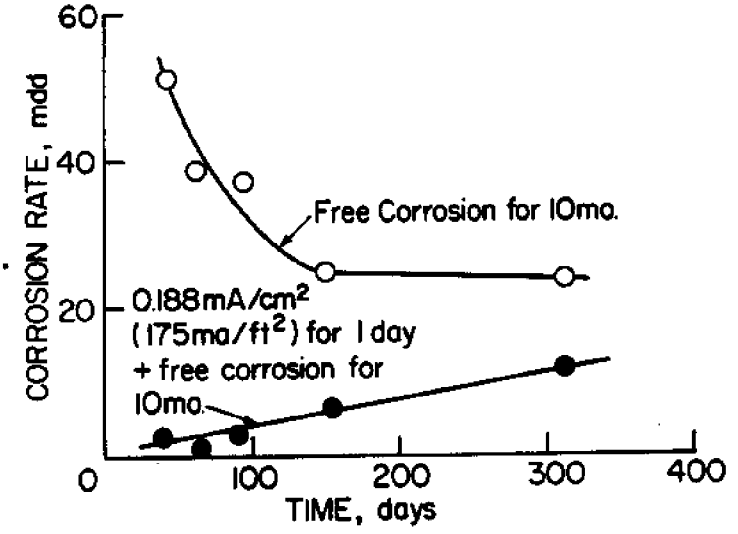

Figure I.9

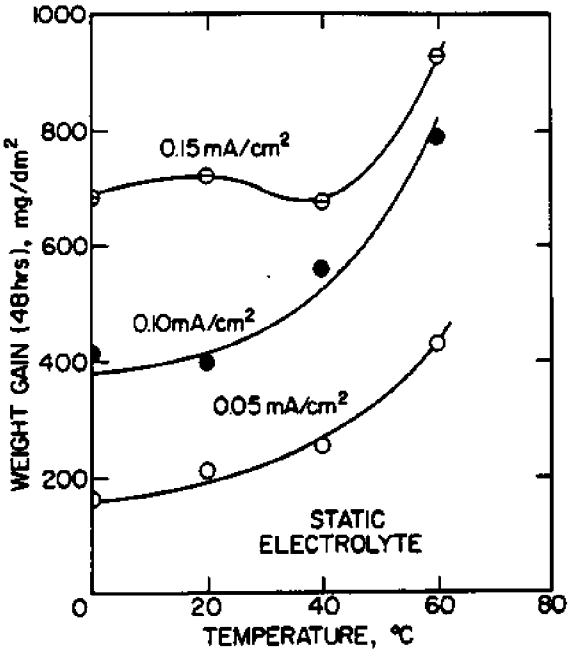

Figure I.10

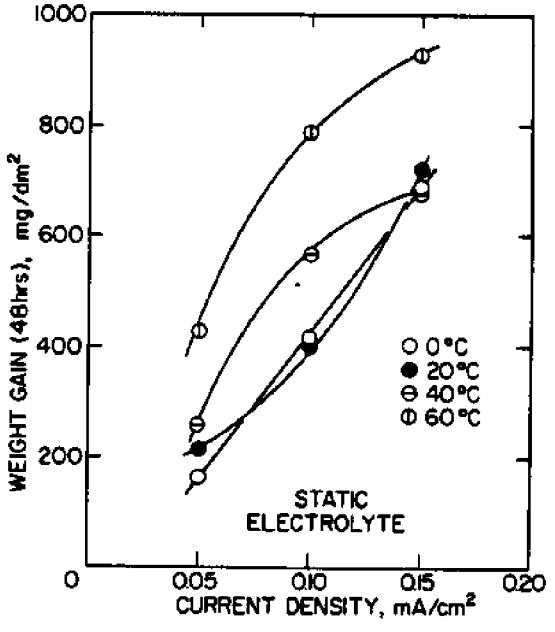

Figure I.11

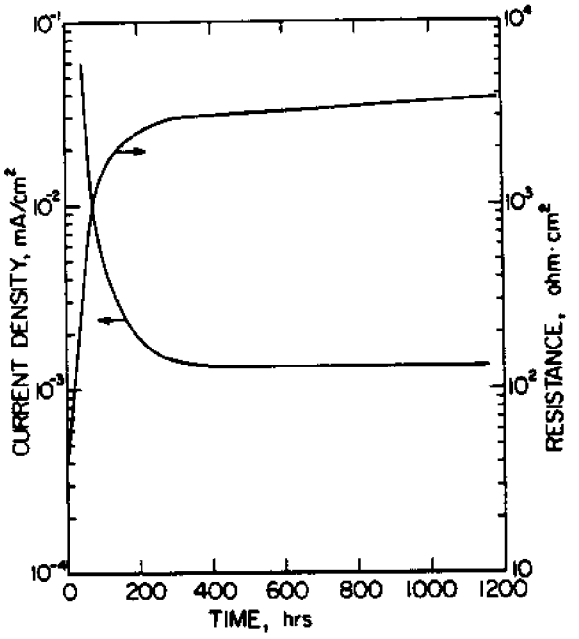

Figure I.12

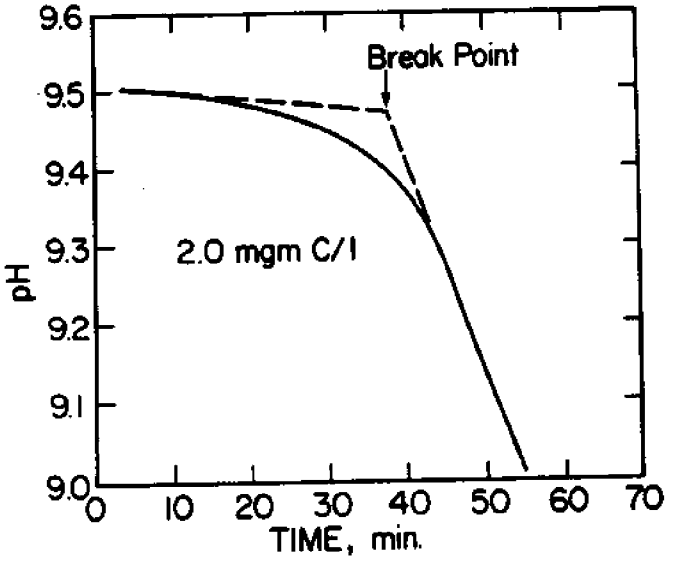

Figure I.13

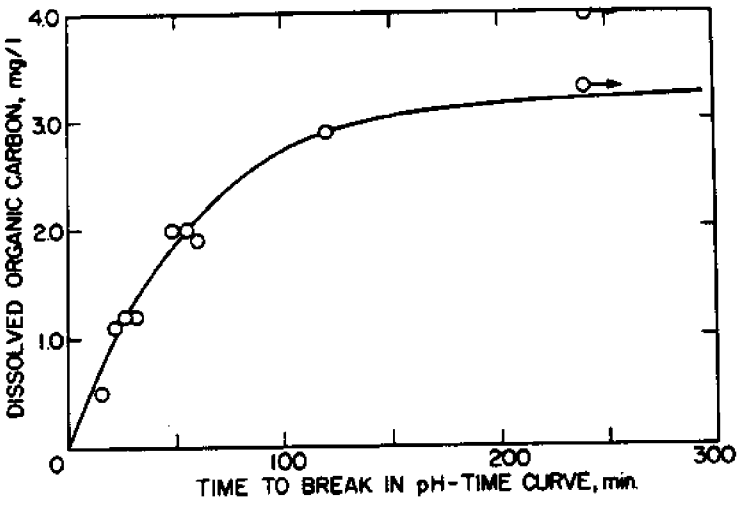

Figure I.14

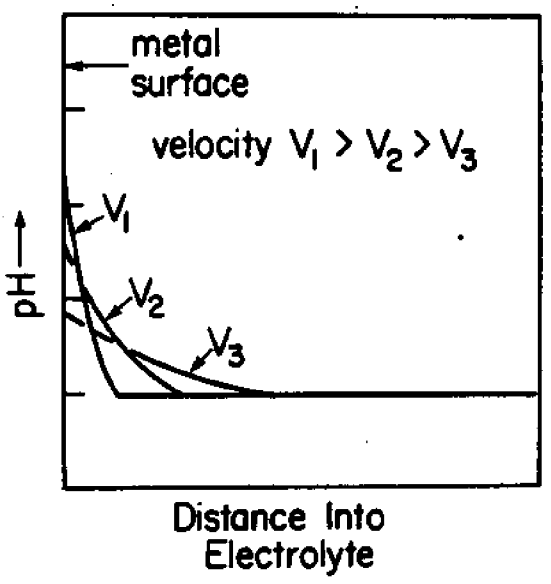

Figure I.15

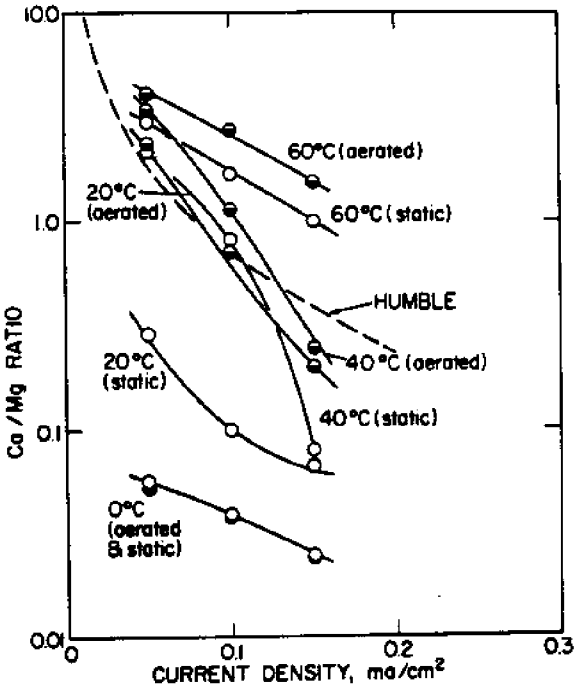

Figure I.16

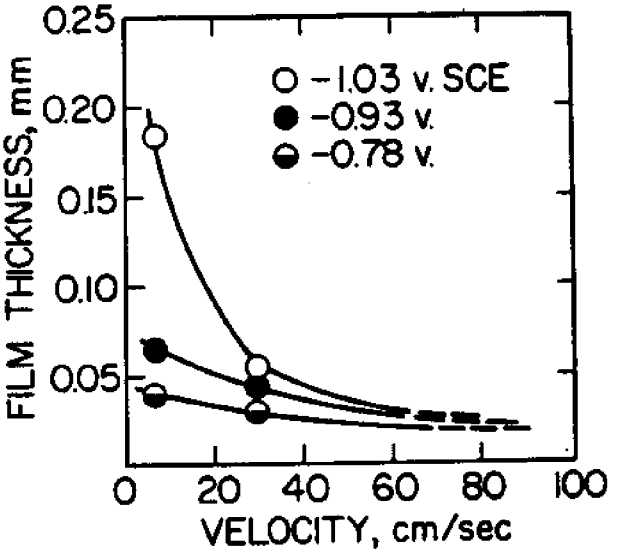

Figure I.17

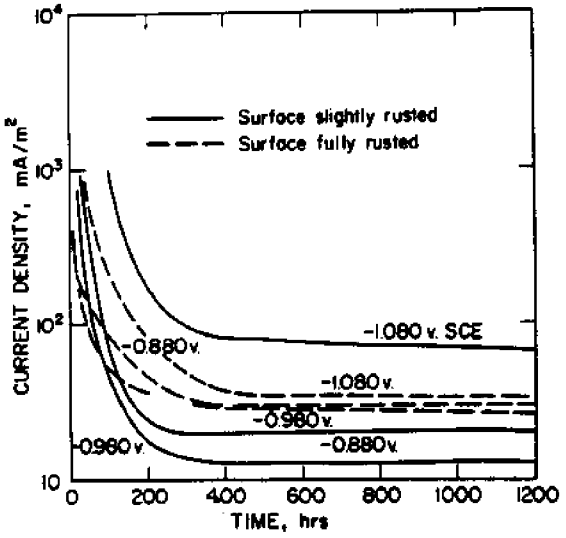

Figure I.18

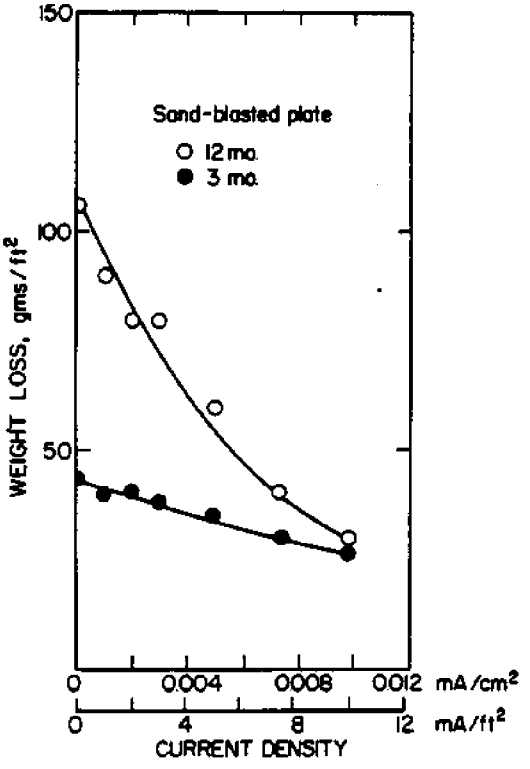

Figure I.19

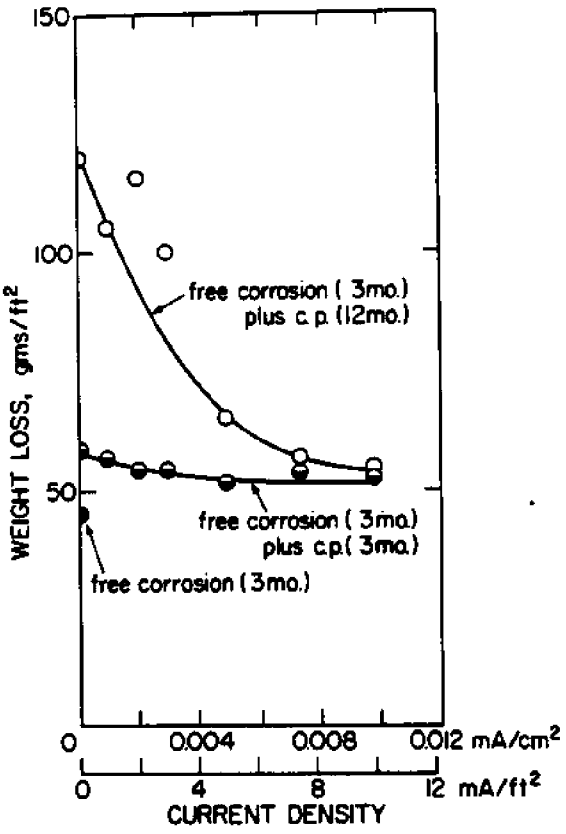
150
100
50
0
WEIGHT LOSS, gms/ft²
free corrosion (3mo.)
plus c.p. (12mo.)
free corrosion (3mo.)
plus c.p.(3mo.)
free corrosion (3mo.)
0.004
0.008
0.012 mA/cm²
0
4
8
12 mA/ft²
CURRENT DENSITY

Figure I.20

II. EXPERIMENTAL PROCEDURE

Standardization of test equipment and experimental procedures are difficult problems whenever different investigators and laboratories are involved. Several different experimental approaches have been employed in the present investigation, each of which has its own set of advantages and disadvantages. Wherever possible investigators have sought to coordinate their particular experimental approach with that of others.

II.A. Material.

Experiments by all investigators employed either iron or low carbon steel (nominally 1018) that was obtained from various sources. While some experimental results have indicated a variation of calcareous deposit formation kinetics from specimen to specimen, it is thought that differences in alloying element composition within normal ranges was not of major importance. As a general rule, substrate variability was not included as a major factor of consideration in the experiments.

II.B. Rotating Ring Disc Electrode (RRDE) Experiments.

Electrochemical measurements were made using a rotating ring disc electrode (RRDE), the design of which was based on that of Sohner et al. (1969) with several modifications. The electrode consists of two sections--the upper or spindle section is designed to fit a Pine Instruments ASR-2 rotator unit modified to include four electronic contacts. The present design utilizes two carbon-silver brushes, one for the ring and one for the disc electrical circuit. These connectors provide a low noise circuit acceptable for the current levels encountered in these studies.

The tip section of the RRDE is of a size to fit in the vacuum chamber of SEM and Auger surface analysis equipment. The exposed electrodes consist of an iron disc (4.45 mm diameter supplied by Climax Molybdenum) and platinum trisected rings of

4.8 mm I.D. and 6.0 mm O.D. brazed to the brass conductor electrodes. The tip is connected to the spindle by a threaded central rod with an "O" ring seal. The potentiostat/galvanostat used for this study is a PAR (Princeton Applied Research Model 173). The ring circuit of the RRDE was not used in the experiments described here but will be used in future studies for determination of soluble corrosion products of iron and for estimation of pH changes at the disc surface.

The electrochemical cell is of two wall pyrex glass construction such that temperature regulated fluid may be circulated between the walls of the cell. The volume of the cell is about 1000 ml. This volume is considered a minimum for proper circulation and dilution of reaction products such that they will not be reacted at the disc or ring. The electrochemical cell incorporates an upper Teflon lid which contains ports for the RRDE, auxiliary electrodes, and gas input/outputs.

In this work the cell was open to air. Three solutions were used throughout the experiments. These were synthetic sea water based on ASTM D1141 and natural sea water from either St. Augustine beach or from Crescent Beach, Florida. Platinum gauze was used as an anode and Ag/AgCl as a reference electrode.

Surface microscopy was carried out in a scanning electron microscope (SEM) JEOL JSM35C. In a few instances a Zeiss ICM405 metallurgical microscope was used for surface examination.

X-ray intensities of particles were evaluated using an Acton Laboratories Microprobe Model MS64. Elemental analysis was carried out using atomic absorption Heath 703 equipment.

For surface and depth of profile spectra estimation, Auger electron spectroscopy equipment was used. It consists of a custom ultra-high vacuum system, and a PEI (Physical Electronic Instruments) film analyzer. The auger spectra were taken using a 3 KeV electron gun beam, and, in argon ion bombardment, a 2 KeV beam was used.

The following sequence for surface preparation was adopted: specimens were abraded with silicon carbide (SiC) paper down to

600 grit and rinsed with distilled water between each grade. After the final abrasion the specimens were ultrasonically cleaned and rinsed in ethyl alcohol, air dried and transferred to the cell for cathodic polarization.

For a series of experiments, after abrasion with 600 grit paper, the specimens were polished with diamond polishing compound (6 μm), followed by ultrasonic cleaning in alcohol.

II.C. Rotating Cylinder Electrode Experiments.

Design of this experimental system is as shown in Figure II.C.1. The rotating cylinder electrode test technique was employed for some experiments because of the relatively large surface area involved and the fact that hydrodynamics for this electrode are well established (Gabe, 1974). The corrosion cell consisted of a 12.7 mm diameter by 25.4 mm long steel working electrode connected at each end to 12.7 mm diameter Teflon rods. The top of the cell contained ports for a platinum counter electrode, which was also cylindrical and symmetric about the working electrode, a salt bridge, a combination pH electrode, an oxygen electrode and a gas dispersion tube. The cell also had an outer water jacket for temperature control. Potential between the steel and a reference calomel electrode was maintained constant either by a PAR Model 174A Polargraphic Analyzer (U of Delaware system) or by a locally fabricated potentiostat (FAU experiments). The cell had a two liter capacity with the electrolyte being either 1) NaCl-distilled water, 2) various synthetic sea waters, 3) sea water, closed cell (U. of Delaware), 4) one-through natural sea water (FAU) or 5) recirculated natural sea water (FAU)*. In experiments where oxygen concentration and pH were measured on Orion Model 97-08-00 oxygen electrode and Corning Model 476050 combination -pH electrode standardized on the National Bureau of Standards pH scale were employed.

---

* U. of Delaware experiments employed sea water that was obtained approximately 40 miles offshore, passed through 0.2 μm membrane filter and stored aerated in carboys. FAU experiments used sea water pumped via an all plastic piping system directly to the Center for Marine Materials Laboratory (Hartt, 1981).

II.2.D. Velocity Experiments.

To aid in characterizing the dependence of calcareous deposit formation kinetics upon water flow an experimental apparatus was employed which permitted accurate measurement of flow rate and with known hydrodynamic properties based on established boundary layer theory. This system was a submersible water tunnel which included the following features:

1. Flows ranging from 0.3 to 2 m/sec.
2. A 0.9 m long plexiglas housed test section to accommodate the flat plate.
3. Accessible test section.

In essence, this approach to the experimental problem allowed a flat plate to be subjected to a uniform flow field. A schematic illustration of the water tunnel is shown in Figure II.D.1. The tunnel was immersed in a test tank containing natural sea water. The system was powered by a 24 volt d.c. submersible electric motor located downstream from the test section. Velocity within the test section was altered by changing the input voltage to the motor. Thus, sea water from the test tank was drawn through the intake section at a known rate, across the test plate and exhausted at the rear of the tunnel.

A composite plexiglass and steel plate was fabricated for the experiments. The plate consists of 40 individual steel segments, each electrically isolated from one another. Segments 1 through 20 each had an area of 12.9 cm^2, while segments 21 through 40 had an area of 25.8 cm^2. Prior to each experiment the test plate was abraded with 200 grit aluminum oxide paper, degreased with alcohol and placed in the tunnel. The plate was then cathodically protected with a Wenking Potentiostat.

The forty steel segments were wired in parallel through a mechanical switch system of the potentiostat. The current was read as a voltage drop across a one ohm resistor in the switch system. A Keithley Model 610-C Electrometer was used for this measurement. The potential was measured versus a saturated calomel electrode (SCE). Each test was designed to last 7 days.

II.E. Simulated Fatigue Experiments.

The experimental plan was based upon two types of simulated fatigue crack specimens, one of which is illustrated in Figure II.E.1. The second type was of one-quarter scale in the width and thickness dimensions. Thus, two mating, machine ground faces simulated a fatigue crack and thereby permitted more detailed study of calcareous deposit formation in this region than would be possible in the case of an actual fatigue crack. Specimen Type A was comprised of three parts, whereas Type B was a modification of this involving four components. The specimen design permitted 0.76 mm OD, 0.25 mm ID Tygon tubes to be inserted through the specimen and sealed flush with the lower crack faces. Figure II.E.2 presents a more detailed view of Part 2 for the smaller type specimen. For the 2.54 cm. thick specimen ten potential probe holes were employed. Hence, the potential profile within the simulated crack could be measured.

The specimens were machined from either 6.4 mm or 25.4 mm thick cold finished 1018 steel plate. The simulated crack faces were finished by surface grinding in order to render these as flat as possible. All surfaces were acetone degreased and, except for the crack faces and the front face 25 mm above and below the crack, were coated with aerosol Quelspray.

Figure II.E.3. illustrates the specimen in prospective to the electrolyte bath and other instrumentation. The bath was of an all plexiglass construction with nylon fittings and was such that electrolyte entered near the base and flowed upward past the specimen at a prescribed rate. The saturated calomel electrode employed for potential control was located in the overflow compartment of the bath, while the Pt coated Nb counter electrode was mounted on the bath wall immediately opposite the uncoated specimen face. Potentiostatic control was affected using either a Wenking Model 68 FRO.5 potentiostat or a locally fabricated instrument based upon the circuitry proposed by Baboian (1979). Potential and current were monitored and recorded by three

alternative techniques which were 1) an Orion Model 701 pH/mv meter, 2) a Gould Model 2400 four channel strip chart recorder and 3) an Esterline Angus Model PD 2064 data acquisition system.

The cyclic motion of the upper part of the specimen was developed by a modified Fatigue Dynamics Model VSP-150 Machine. Frequencies of 0.1, 0.5 and 1.0 Hz were employed, and the stroke of the fatigue machine was adjusted such that the maximum and minimum crack openings per cycle were 0.25 and 0.05 mm, respectively, as determined by viewing the front specimen face with a calibrated eyepiece microscope. The electrolyte was either recirculated 3.5% NaCl-distilled water or flowing (non-recirculated) natural sea water, as is available at the Center for Marine Materials Laboratory. Water flow rate was 100, 500 or 1000 ml/min. which for the present specimen and bath geometry corresponded to nominal velocities of 1.6, 8 and 16 mm/sec. The purpose of tests in the former electrolyte was to assess the influence of nominal water velocity, cyclic frequency and control potential upon potential profile within the simulated crack without concern for time dependence of this latter parameter due to precipitation of calcareous material. It was determined that these experiments could be performed by stepping through the variables of interest and allowing approximately thirty minutes in each case for steady state to be achieved. This procedure was not attempted in seawater because it was thought that the deposit developed under one set of conditions may be unique and not apply to others. Most sea water tests were either one or two weeks in duration.

Subsequent to testing, calcareous deposits on the crack and boldly exposed faces of specimens exposed in sea water were examined by scanning electron microscopy and in some cases the chemistry of these was characterized by EDAX analysis.

BIBLIOGRAPHY (SECTION II)

R. Baboian, L. McBride, R. Langlais and G. Haynes, Materials Performance, Vol. 18(12), 1979, p. 40.

D. R. Gabe, J. Applied Electrochem., Vol. 4, (1974) p. 91.

W. H. Hartt, "Fatigue of Welded Structural Steel in Sea Water," paper no. 3962 presented at Offshore Technology Conf., May 4-7, 1981. Published in conference proceedings.

R. H. Sohner, B. Miller and R. E. Visco, Analytical Chem., Vol. 41, 1969, p. 19.

FIGURE CAPTIONS

Figure II.C.1: Schematic representation of rotating cylinder experimental system.

Figure II.D.1: Schematic representation of water tunnel.

Figure II.E.1: Schematic illustration of the specimen employed in the simulated crack study.

Figure II.E.2: Detail of Part 2 From Specimen Type B showing the location and geometry of holes for potential measurement within the simulated crack of the 6.4 mm thick specimens.

Figure II.E.3: Schematic representation of test system, including specimen and bath.

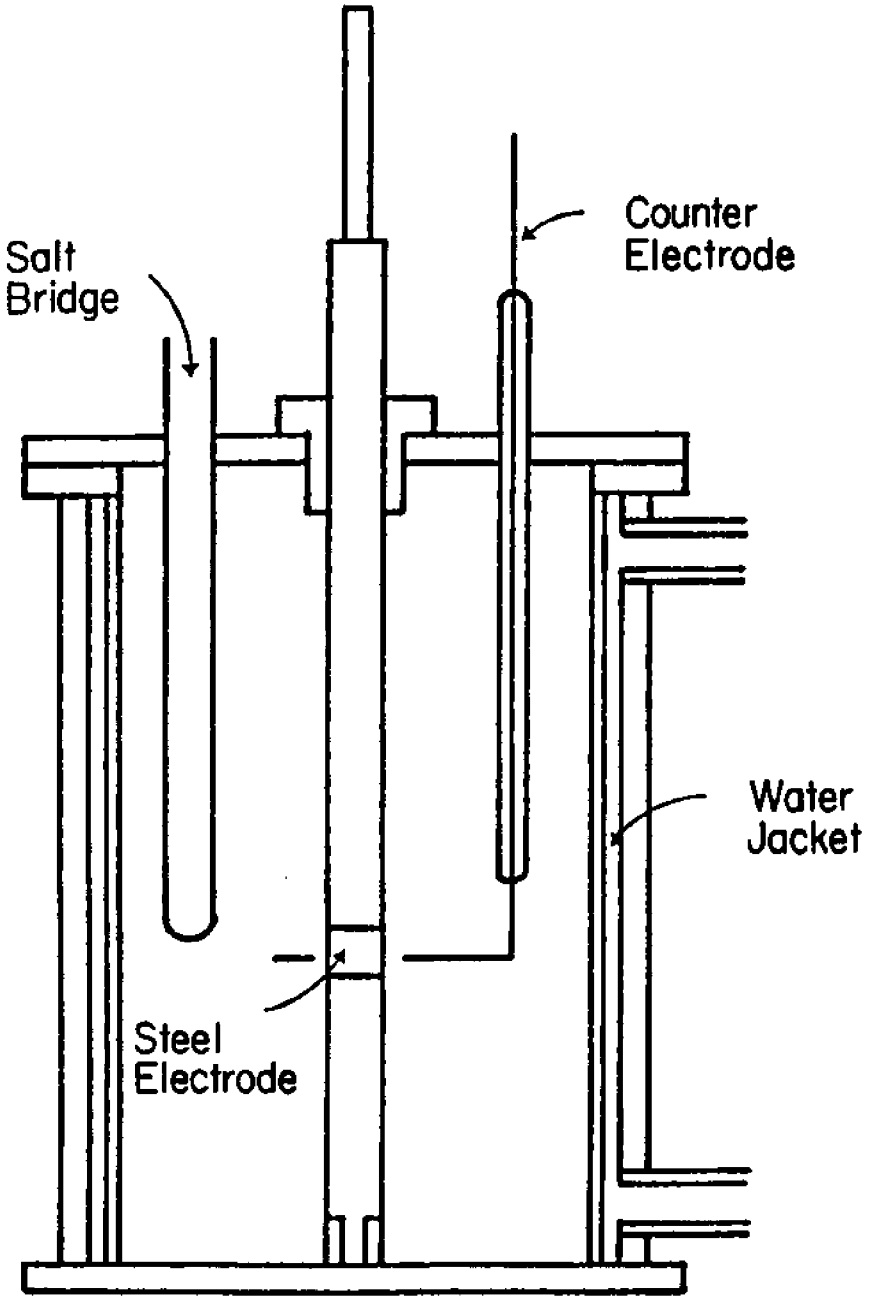
Salt
Bridge
Counter
Electrode
Water
Jacket
Steel
Electrode

Fig.II c.I

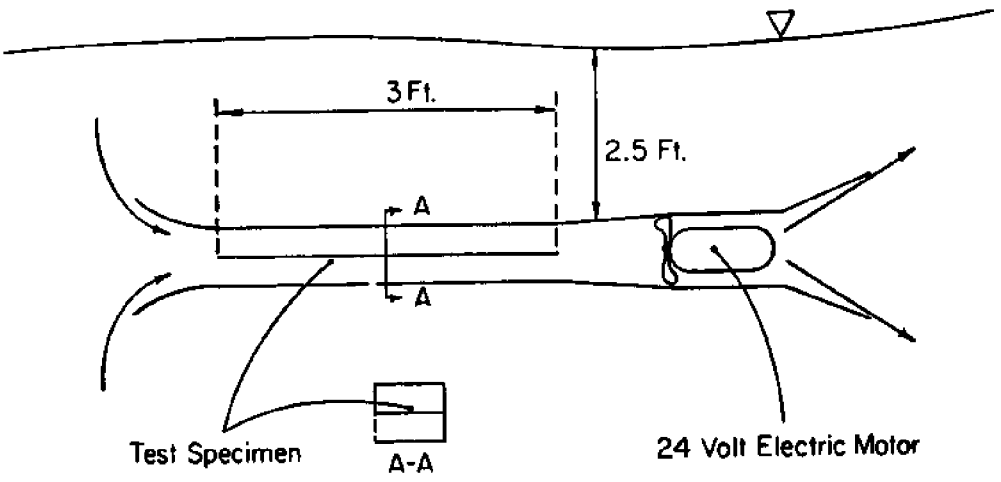

Fig.II D.I

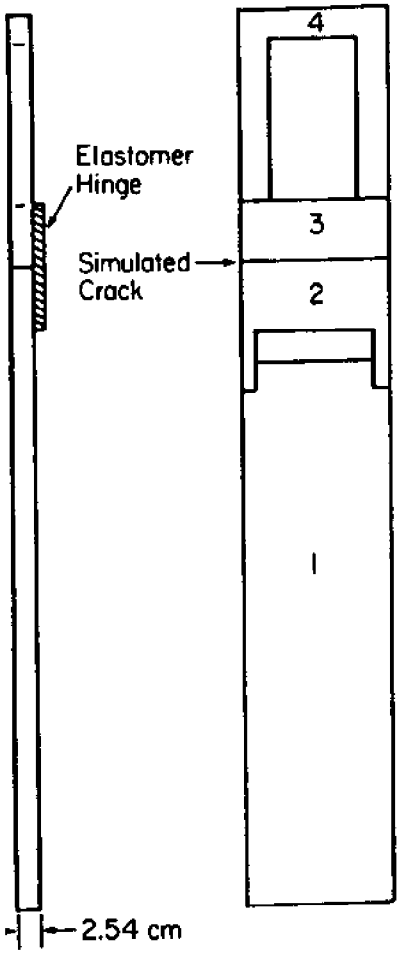

Fig.II E.I

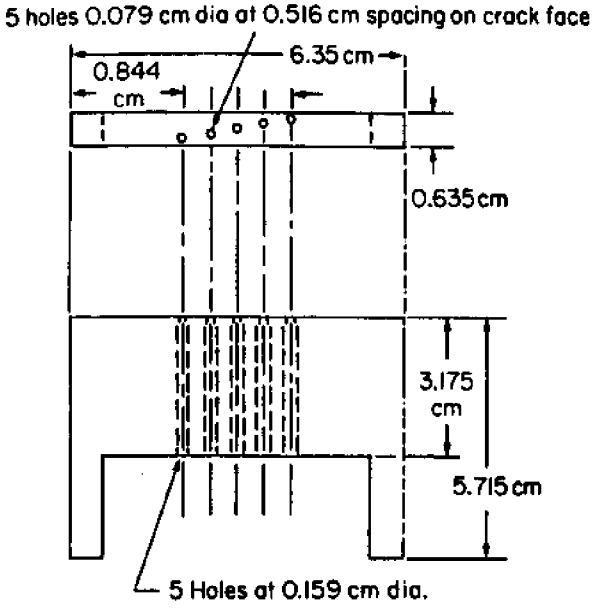

Fig.II E. 2

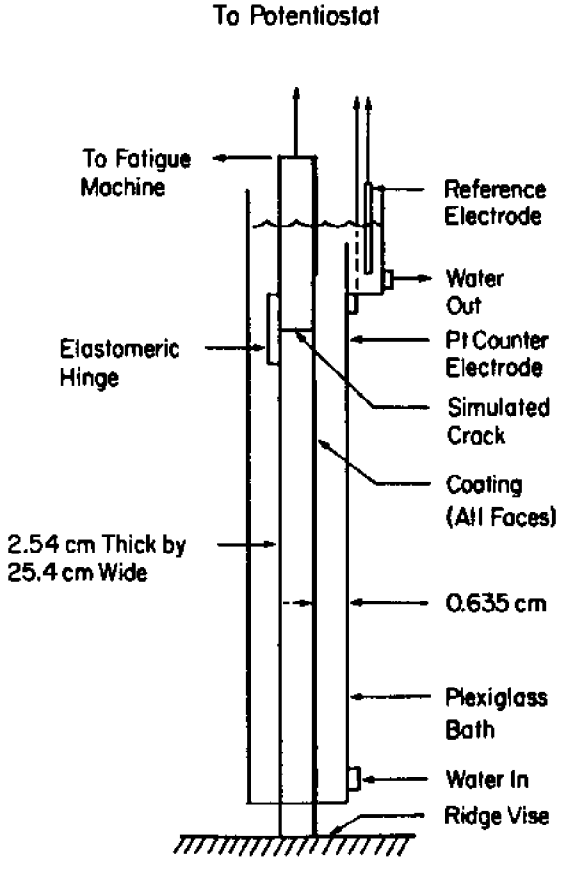

Fig.II E. 3

III. RESULTS AND DISCUSSION

III.A. Seawater Chemistry

Calcium carbonate, $CaCO_3$, and magnesium hydroxide, $Mg(OH)_2$, are slightly soluble in seawater, and their solubilities can be represented by their solubility products,

$$K_{sp}(CaCO_3) = (Ca^{+2})(CO_3^{-2}) \qquad \text{(III.A.1)}$$

$$K_{sp}(Mg(OH)_2) = (Mg^{+2})(OH^{-})^2 \qquad \text{(III.A.2)}$$

where the parentheses represent molar concentrations. Calcium carbonate occurs in two crystal forms in seawater, as calcite or aragonite. Calcite has the least solubility and is the thermodynamically stable phase under oceanic temperatures and pressures, but aragonite is the phase which actually occurs in calcareous deposits formed during cathodic protection (Hilbertz, 1976). Solubility products for calcite, aragonite, and magnesium hydroxide are given in Table III.A.1.

Figure III.A.1 shows a typical $CaCO_3$ (aragonite) deposit observed on cathodically polarized surfaces during this research. On rare occasions, brucite, $MgOH_2$, is observed (Figure III.A.2). The chemistry of the deposits in Figures III.A.1 and III.A.2 was identified by EEDS analysis. The difference in morphology between the two phases is obvious from the figures. The consequences of aragonite versus brucite with regard to calcareous deposit properties are addressed in the following sections.

Any chemical, physical, or biological processes in seawater which affect the concentrations of the ions in the solubility

products (Equations III.A.1 and III.A.2) will affect the solubilities of $CaCO_3$ and $Mg(OH)_2$, and thus may affect the efficiency of the cathodic protection of steel in seawater. In addition to the ions in Equations III.A.1 and III.A.2, the concentration of dissolved oxygen is expected to be an important variable affecting cathodic protection of steel in seawater, since the diffusion of oxygen to the steel surface controls the production of hydroxide and carbonate ions at the interface. In the following sections we will discuss the effects of

1. calcium and magnesium;
2. dissolved oxygen; and
3. pH and carbonate ion

on the current density required for cathodic protection of steel in seawater. The experiments addressing these variables were performed with the rotating cylinder electrode (RCE) described in the section on experimental procedure. Unless otherwise noted, the rotating steel electrode was polarized to -0.90 volt versus a saturated calomel reference electrode.

III.A.1. Effects of Dissolved Calcium and Magnesium

Dissolved calcium and magnesium are major constituents of seawater, and their concentrations are directly proportional to the salinity (Table III.A.2).

Calcareous deposits formed during cathodic protection in seawater contain both calcium carbonate and magnesium hydroxide (Humble, 1948). In order to determine the relative efficiency of

$Mg(OH)_2$ and $CaCO_3$ as coatings, we performed the experiments shown in Figures III.A.3 and III.A.4. Figure III.A.3 shows the results of an experiment in which steel was cathodically protected in calcium free synthetic seawater (0.50 NaCl + 0.03 Na_2SC_4 + 0.0025 $NaHCO_3$ + 0.05 $MgCl_2$). In this solution magnesium hydroxide is the only solid phase which can form. Magnesium hydroxide is very soluble in seawater at normal oceanic pH, and the purpose of this experiment was to determine if a $Mg(OH)_2$ coating would actually form in seawater of pH = 8. The results in Figure III.A.3 show that a $Mg(OH)_2$ deposit does indeed form at pH = 8.2, but a comparison of Figure III.A.3 with the results of cathodic protection in natural seawater (Figures III.B.4 and III.B.6) shows that the current density across a $Mg(OH)_2$ deposit (Figure III.A.3) is at least twice that across a deposit containing $CaCO_3$ (Figures III.B.4 and III.B.6). Thus, magnesium hydroxide is not as effective a deposit as calcium carbonate for cathodic protection. Seawater does not become saturated with respect to $Mg(OH)_2$ until the pH is increased to 9.3 (Pytkowicz and Gates, 1968). The results in Figure III.A.3 show that the observed current density decreases as the solution pH increases. Careful inspection of this figure shows that the observed current density reached a constant value at pH = 8.2 and pH = 9.2, and that it did not continue to decrease with time at these two pH values. This suggests that the deposit had reached a steady state in which the deposit surface was dissolving as rapidly as new $Mg(OH)_2$ was being formed at the steel surface. It was not until the solution pH was increased to 9.6 (solution supersaturated with $Mg(OH)_2$) that the

current density decreased to values characteristic of natural seawater (Figures III.B.4 and III.B.6). Under these supersaturated conditions the current density (Figure III.A.3) did not reach a constant value but continued to decrease with time, suggesting that the $Mg(OH)_2$ deposit continued to grow and did not dissolve into the bulk seawater.

In Figure III.A.4 we show the results of an experiment designed to test the efficiency of pure $CaCO_3$ as a coating for cathodic protection. This experiment was conducted in three parts. The corrosion cell was initially filled with calcium and magnesium free synthetic seawater (0.42 NaCl + 0.028 Na_2SO_4 + 0.0024 $NaHCO_3$). This solution has the sodium, sulfate, and bicarbonate concentrations of normal seawater. This part of the experiment was designed to determine the current density in the absence of calcareous coatings (Culberson, 1983). In Figure III.A.4, the points between 1 and 24 hours were measured in the above calcium and magnesium free synthetic seawater. These points represent the current density in the absence of any coating.

After 24 hours, 0.01 M $CaCl_2$ was added to the corrosion cell. The current density began to decrease immediately, and within 12 hours it had decreased from 170 to 2 $\mu amp/cm^2$. Under these conditions (no dissolved magnesium) a very protective carbonate film was formed. The observed current densities in this part of the experiment are much lower than those obtained in natural seawater (Figures III.B.4 and III.B.6), suggesting that the presence of magnesium in natural seawater causes the formation of a less protective coating. It is well known that dissolved

magnesium in seawater inhibits the nucleation and precipitation of calcium carbonate (Pytkowicz, 1965), and the third part of this experiment was designed to show the effect of magnesium on the formation of the calcareous deposit.

After 80 hours, the steel electrode was removed from the cell and rinsed with dilute acid and distilled water to remove the carbonate deposit. Magnesium chloride (0.055 M) was added to the corrosion cell, the steel electrode replaced in the cell, and the experiment resumed. The synthetic seawater in the cell now had a major ion composition similar to natural seawater.

The inhibitory effects of magnesium on formation of the calcreous deposit are evident in Figure III.A.4. In the presence of magnesium, the current density drops slowly rather than abruptly, as in part 2 when only calcium was present, and the final current density after 72 hours of cathodic protection was 30 times higher than in the absence of magnesium.

III.A.2. Effect of Dissolved Oxygen

The effects of dissolved oxygen on current density during the cathodic protection of steel in seawater and in 0.5 M NaCl are shown in Figures III.A.5 and III.A.6. These experiments were performed in natural seawater or in buffered sodium chloride (0.50 M NaCl + 0.0027 M $NaHCO_3$) (Culberson, 1983). The concentration of oxygen was adjusted by bubbling varying amounts of nitrogen and oxygen gas through the test solution. The compressed nitrogen and oxygen each contained 340 ppm carbon dioxide, thus maintaining a

constant solution pH regardless of the O_2/N_2 ratio.

The measurements in NaCl (Figure III.A.5) show a linear relationship between the dissolved oxygen concentration and the current density required for cathodic protection. This result agrees with previous work (Windfeldt, 1961) and can be explained by Fick's first law of diffusion (Bockris and Reddy, 1970):

$$J(O_2) = D(O_2)x(\Delta O_2/\Delta x) \qquad \text{(III.A.3)}$$

where $J(O_2)$ = flux of oxygen to steel electrode;

$D(O_2)$ = diffusion coefficient of dissolved oxygen; and

$\Delta O_2/\Delta x$ = oxygen concentration gradient at interface.

If the concentration of oxygen is zero at the steel-water interface, then the diffusion of oxygen to the steel electrode and thus the current will be directly proportional to the concentration of oxygen in solution.

Figure III.A.6 shows the effect of dissolved oxygen on the current density required for cathodic protection in seawater. The current was allowed to reach a constant value at an oxygen concentration corresponding to air saturation; the oxygen concentration was then reduced to zero and the current monitored until it reached a constant value. The oxygen concentration was then increased in steps, allowing the current to stabilize after each increase.

Previous measurements (Windfeldt, 1961) with planar steel electrodes in a quiescent solution (potential -0.94 volts versus a saturated calomel electrode) show a linear relationship between current density and dissolved oxygen during cathodic protection of steel in 3% NaCl and in seawater. We also found a linear

relationship in NaCl. However, in seawater we found that although the current density increased with increasing oxygen concentration at low oxygen concentrations, it remained constant or decreased slightly at oxygen concentrations greater than air saturation (4.88 ml O_2/liter).

Uhlig (1971) shows that high concentrations of oxygen passivate steel surfaces, and that high pH lowers the concentration of oxygen required for passivation. This is consistent with the conditions of these seawater experiments; oxygen concentrations greater than air saturation and high pH at the steel-water interface. However, Uhlig (1971) states that passivity never occurs in seawater due to its high chloride concentration.

III.A.3. Effect of pH and Carbonate Ion

The effects of solution pH on current density during cathodic protection of steel in seawater are shown in Figure III.A.7. These data show that current density decreases as the solution pH increases, probably because the increased concentrations of carbonate and hydroxide ions in solution cause $CaCO_3$ and $Mg(OH)_2$ to be less soluble at the steel-water interface.

The experiments (Culberson, 1983) were performed in the same natural seawater used in the oxygen concentration experiments. Seawater pH was adjusted with compressed air containing varying amounts of carbon dioxide. The experiment was performed by allowing the current density to reach a steady state at a partial

pressure of carbon dioxide (343 ppm CO_2) corresponding to natural air. This partial pressure yielded a seawater pH = 8.2, the normal oceanic surface water pH. The seawater pH was then raised to 8.65 by bubbling with low CO_2 air, and the resulting steady state current density measured. The pH was then decreased in steps by increasing the CO_2 content of the compressed air. After each pH decrease, the current was monitored until a steady state value was reached.

The decrease in current density at high pH could be due to several factors since the concentrations of hydroxide, bicarbonate, carbonate, and total dissolved inorganic carbon all change as the pH changes. The results of the experiment are summarized in Table III.A.3. There is a negative linear correlation between current density and the carbonate ion concentration in the bulk seawater (Figure III.A.8). The correlation suggests that increased carbonate ion concentration in solution enhances the precipitation of $CaCO_3$ at the steel-water interface and thus reduces the current density.

There is a positive linear correlation between current density and bicarbonate ion concentration and between current density and the concentration of total dissolved inorganic carbon. However, because of the positive correlation, the lowest current densities occur at the lowest concentrations of these two parameters. Therefore, the concentrations of bicarbonate and total carbon do not seem to control the current density.

III.A.4. Hydrogen Evolution at the Steel Cathode

In the previous discussion it has been assumed that the only reaction at the steel cathode which supplies current is the reduction of oxygen,

$$0.5O_2 + H_2O + 2e^- = 2OH^-. \qquad \text{(III.A.4)}$$

However, hydrogen evolution also occurs at the cathode,

$$2H_2O + 2e^- = H_2 + 2OH^- \qquad \text{(III.A.5)}$$

as is evident from Figures III.A.5 and III.A.6 in which the measured current density does not go to zero at zero oxygen concentration.

Figure III.A.9 shows the results of an experiment in buffered sodium chloride (0.70 NaCl + 0.002 $NaHCO_3$) designed to determine the importance of hydrogen evolution in suppling current in air saturated solutions. In this experiment the current density was measured as a function of the potential applied to the steel electrode for applied potentials between -0.7 and -1.15 volts. If oxygen reduction was the only reaction supplying current, the current density should be independent of potential. This is approximately true for the points in Figure III.A.9 between -0.7 and -0.95 volts. However, the current rapidly increases at potentials less than -0.95 volts, apparently due to hydrogen evolution. Gas bubbles were observed on the steel electrode beginning at -1.0 volt.

The currents plotted in Figure III.A.9 represent the sum of the currents due to oxygen reduction and hydrogen evolution. The straight line plotted on Figure III.A.9 is an attempt to calculate

the current due to hydrogen evolution by assuming that the current density measured at -0.95 volts is entirely due to oxygen reduction, and then subtracting the current at -0.95 volts from the measured currents at each potential more negative than -0.95 volts. The potentials plotted on Figure III.A.9 also include a small correction for the IR drop in the solution. The IR drop correction is only significant at potentials more negative than -1.05 volts. Note that the slope of the hydrogen evolution line in Figure III.A.9 is 120 mv/decade which is the expected slope for hydrogen reduction (Andresen, Gartland, and Bardal, 1981).

Extrapolating the hydrogen reduction line in Figure III.A.9 to -0.90 volts, the cathodic potential used in this work, yields approximately 10 $\mu amp/cm^2$ as the current due to hydrogen reduction. This value is in approximate agreement with the data in Figures III.A.5 and III.A.6 at zero oxygen concentration.

III.A.5. Comparison of Electrolytes

This section presents the results of an investigation contrasting data obtained in a series of otherwise identical once-through and recirculating seawater experiments in which the current decay rates of cathodically protected steels were determined.

While recirculated natural seawater and even artificial seawater have been employed for testing and research pertaining to calcareous deposits in the marine environment, it is not clear that these electrolytes permit realistic simulation of normal

seawater exposure. Factors inherent to these environments that could cause modified material response from one situation to the next include differences in organic content and minor element and carbonate chemistry.

Seawater for all experiments was that available at Florida Atlantic University. Flow rate through the test cells was 1 liter per minute in all cases. Experiments invloving recirculating electrolyte employed 2 liters of solution in conjunction with a peristaltic pump.

Prepared specimens were placed in the seawater bath and a potential of -1.00VSCE was applied by a locally fabricated potentiostat. Potential and current were monitored and recorded for 48 to 50 hours using an Esterline Angus Model PD2064 Data Acqusition System. Each experiment was repeated at least three times to assure reproducible results.

When specimens cut from the same bar were used, reproducible current densities were obtained for experiments run in flow-through seawater. A typical set of results can be seen in Figure III.A.10. Note the current dropped from 180 $\mu amp/cm^2$ to 25 $\mu amp/cm^2$, an 86% drop.

Current densities observed for specimens placed in the recirculating seawater bath differed substantially from those observed for a once-through bath. Also, results were less reproducible and the steady state current value was much greater than that of the once through experiments. Typical results contrasting once-through and recirculating systems are shown in Figure III.A.11.

Figure III.A.12 illustrates typical results from a comparative run of once-through seawater and artificial seawater. As can be seen the artificial seawater resulted in a higher current density than the once-through system. Calcareous deposits were observed to form on the steel in the artificial seawater. There were, however, problems maintaining the stability of the artificial seawater when the specimen was under cathodic protection.

The observation that natural and artificial seawater yielded film formation rates that differed from once-through seawater can probably be traced to differences in the organic character of the water or depletion of constituent ions. While care was taken that the area of the specimen was small compared to the volume of the seawater, there would still have been a depletion of calcium and perhaps some minor elements during precipitation. However, in light of the work of Chave and Suess (1970), it is believed that the organic character of seawater is likely important to the development of the calcareous film. The organics are very surface active and can change the activity of ions at the surface. They may also affect the kinetics of the precipitation reactions. For these reasons organics are suspect as a cause of the differences observed.

III.B. Effect of Temperature on Calcareous Deposits

It is generally observed that current requirements for cathodic protection of steel in seawater increase at low temperatures. The increased current requirements are apparently due to the difficulty in forming calcareous deposits in seawater at low temperatures. One of the major goals of this project has been to explain the increased current requirements at low temperatures in seawater in terms of the chemical properties of seawater and of the calcareous deposits.

Temperature could affect the formation of calcareous deposits at the steel-seawater interface in several ways:

1. by changing the solubilites of $CaCO_3$, $Mg(OH)_2$, and dissolved oxygen in seawater;
2. by affecting the kinetics of precipitation of $CaCO_3$ and $Mg(OH)_2$; and
3. by affecting the rate of diffusion of oxygen and other substances at the steel-seawater interface.

To determine the relative importance of the above processes, experiments have been performed in natural seawater and in sodium chloride solution at 25°C and at 3°C.

III.B.1. Effect of Temperature in Absence of Calcareous Deposit

The experiments in air saturated sodium chloride (0.70 molar NaCl + 0.0025 molar $NaHCO_3$) were designed to determine the effect of temperature on current density in the absence of calcareous coatings. In these experiments the potential of the steel electrode was held constant at -0.9 volt versus a 3.5 molar

calomel electrode, and the current density required to maintain this potential was measured as a function of the rotation speed of the rotating steel electrode. The dissolved oxygen concentrations and the pH of these air saturated NaCl solutions at 25°C and 3°C are listed in Table III.B.1.

The results of two separate experiments are shown in Figures III.B.1 and III.B.2. The most obvious feature of the two figures is that the current density required to maintain a steel electrode potential of -0.9 volt is about 50% lower at 3°C than at 25°C. This is exactly opposite the behavior observed in natural seawater, in which the current requirements increase as the temperature decreases! In Figures III.B.1 and III.B.2, the ratio of the current densities at 25°C and 3°C is remarkably constant over the entire range of rotation speeds from 10 to 175 rpm (Table III.B.2).

In addition to the constant ratio between the current densities at 25°C and at 3°C, two additional features are evident in Figures III.B.1 and III.B.2. The first is that the current density is independent of rotation speed between 0 and 5 rpm. This observation is in agreement with theoretical calculations for rotating cylindrical electrodes (Billings and Ritchie, 1980) which show that the thickness of the diffusion layer is independent of rotation speed for speeds less than 10 rpm. The second feature of Figures III.B.1 and III.B.2 is that current density increases with rotation speed.

The features of Figures III.B.1 and III.B.2 can be explained by analyzing the diffusion of dissolved oxygen to the steel electrode in terms of Fick's first law of diffusion:

flux of species i = (diffusion coefficient of i)x (concentration gradient of i at interface) (III.B.1)

In terms of dissolved oxygen Fick's law becomes:

$$J(O_2) = D(O_2)x(\Delta O_2/\Delta x) \quad \text{(III.B.2)}$$

where $J(O_2)$ = flux of oxygen to steel electrode;

$D(O_2)$ = diffusion coefficient of dissolved oxygen; and

$\Delta O_2/\Delta x$ = oxygen concentration gradient at interface.

During cathodic protection, the concentration of dissolved oxygen is zero at the surface of the steel electrode, and Equation (III.B.2) can be written:

$$J(O_2) = D(O_2)x(O_2(sat))/\Delta x \quad \text{(III.B.3)}$$

where $O_2(sat)$ = the concentration of dissolved oxygen (mol/cm^3) in 0.70 molar NaCl at air saturation (Table III.B.1). The current density is proportional to the flux of oxygen to the steel surface:

$$i = 4xJ(O_2)xF \quad \text{(III.B.4)}$$

where 4 = the number of electrons produced per mole of oxygen reduced; and

F = Faraday's constant (96,487 coulombs/mol); and

i = current density.

Combining Equations (III.B.3) and (III.B.4) yields:

$$i = 4xFxD(O_2)x(O_2(sat))/\Delta x. \quad \text{(III.B.5)}$$

In the experiments shown in Figures III.B.1 and III.B.2, the only unknown in Equation (III.B.5) is the thickness, Δx, of the laminar layer across which molecular diffusion occurs. Calculated

values of Δx as a function of rotation speed at 25°C and 3°C are shown in Table III.B.3. The calculations in Table III.B.3 show that the thickness of the laminar layer increases with decreasing temperature, and is about 30% greater at 3°C than at 25°C.

It is clear from Equation (III.B.3) that the lower current densities (Figures III.B.1 and III.B.2) at 3°C relative to 25°C are due to the fact that the flux of dissolved oxygen to the steel electrode surface is lower at 3°C than at 25°C. This might seem suprising since the concentration of dissolved oxygen in solution at 3°C is much greater than that at 25°C (Table III.B.1). However, the diffusion coefficient of oxygen increases with temperature, and the thickness of the laminar layer decreases with temperature (Table III.B.1). Thus the term,

$$D(O_2)x(O_2(sat))/\Delta x \qquad \text{(III.B.6)}$$

in Equations (III.B.3) and (III.B.5) is considerably smaller at 3°C than at 25°C.

The data in Figures III.B.1 and III.B.2 allow us to calculate the approximate pH at the steel-seawater interface in the absence of a calcareous deposit. Consider an unbuffered sodium chloride solution. In this case, the only reaction taking place at the steel electrode is the reduction of oxygen and the subsequent diffusion of hydroxide ion away from the steel electrode into the bulk solution.

$$0.5O_2 + H_2O + 2e^- = 2OH^-. \qquad \text{(III.B.7)}$$

In this case the flux of hydroxide away from the steel surface is 4 times the molar flux of oxygen. Thus,

$$J(OH^-) = 4xJ(O_2) \qquad \text{(III.B.8)}$$

where $J(OH^-)$ = flux of hydroxide ion away from steel surface. The hydroxide flux can also be calculated from Fick's first law, Equation (III.B.1):

$$J(OH^-) = D(OH^-)x(\Delta OH/\Delta x) \qquad \text{(III.B.9)}$$

where $D(OH^-)$ = hydroxide ion diffusion coefficient; and

$\Delta OH/\Delta x$ = hydroxide ion concentration gradient at steel surface.

Combining Equations (III.B.9), (III.B.8), and (III.B.2) and rearranging, yields an Equation for the concentration of hydroxide ion at the steel surface.

$$(OH^-)_o = (OH^-)_b + 4xD(O_2)x(O_2(sat))/D(OH^-) \qquad \text{(III.B.10)}$$

Note that Equation (III.B.10) does not depend on the thickness of the laminar layer, Δx, and thus the hydroxide ion concentration at the steel surface, and consequently the surface pH, is independent of rotation speed.

The hydroxide ion concentration and the pH at the steel surface calculated from Equation (III.B.10) are the maximum possible values because seawater contains bicarbonate ion which will react with hydroxide ion produced at the steel surface, thus lowering the hydroxide ion concentration at the interface.

$$HCO_3^- + OH^- = CO_3^{-2} + H_2O \qquad \text{(III.B.11)}$$

The pH and hydroxide ion concentrations at the steel surface calculated from Equation (III.B.10) at 25°C and 3°C are listed in Table III.B.4. The calculations in Table III.B.4 show that the pH at the steel-solution interface in an unbuffered solution increases from 10.3 at 25°C to 11.3 at 3°C. However the hydroxide ion concentration remains relatively constant because the ionization constant of water decreases an order of magnitude

between 25°C and 3°C.

Seawater is buffered by dissolved inorganic carbon dioxide, and in seawater the flux of bicarbonate ion to the steel surface will decrease the hydroxide ion concentration at the interface. In any solution buffered by carbon dioxide the following Equation expresses the relationship between the flux of dissolved oxygen and the fluxes of hydroxide, carbonate, and bicarbonate ions:

$$4xJ(O_2) = J(OH^-) + 2xJ(CO_3^{-2}) + J(HCO_3^-) \qquad \text{(III.B.12)}$$

where $J(CO_3^{-2})$ = the flux of carbonate ion from the interface into the bulk solution; and

$J(HCO_3^-)$ = the flux of bicarbonate ion from the bulk solution to the steel surface.

In addition to Equation (III.B.12) which represents the charge balance at the electrode surface, an Equation can be written which represents the mass balance of carbon dioxide at the interface:

$$J(TCO_2) = 0 = J(CO_2) + J(HCO_3^-) + J(CO_3^{-2}) \qquad \text{(III.B.13)}$$

where $J(TCO_2)$ = total flux of inorganic carbon to the steel surface; and

$J(CO_2)$ = flux of molecular carbon dioxide, CO_2, to the interface.

The derivation of Equation (III.B.13) assumes that at steady state there is no net flux of inorganic carbon to or from the electrode surface. This is true in a solution such as 0.70 NaCl plus 0.0025 $NaHCO_3$ in which no precipitation of $CaCO_3$ or $Mg(OH)_2$ occurs. Although there is no net flux of inorganic carbon to the steel electrode, there may be fluxes of CO_2, HCO_3^-, or CO_3^{-2} to or from the interface. The constraint is that the sum of the CO_2, HCO_3^-, and CO_3^{-2} fluxes equals zero.

By combining Equations (III.B.12) and (III.B.13) and by

assuming that acid-base equilibrium is achieved in the bulk solution and at the steel-solution interface, it is possible to calculate the concentrations of hydroxide, carbonate, bicarbonate, and molecular carbon dioxide at the steel surface. The results of these calculations are shown in Table III.B.5 for a bulk solution pH = 8.0. Note that the calculated concentrations in Table III.B.5 are only approximate because the calculations ignored the effect of the electrical potential at the interface on ionic concentrations at the interface. Although the data in Table III.B.5 are only approximate, they illustrate several important points. The first is that the pH at the interface is reduced in solutions buffered with inorganic carbon. Comparing Tables III.B.4 and III.B.5 we see that the presence of 0.0025 $NaHCO_3$ in 0.70 NaCl reduces the interfacial pH by about 0.6 pH units at 25°C and at 3°C. The second important conclusion from the data in Table III.B.5 is that the carbonate ion concentration is more than an order of magnitude greater at the interface than in the bulk solution. This means that the solubility of calcium carbonate at the steel surface is at least an order of magnitude less than in the bulk solution.

III.B.2. Effect of Temperature on Calcareous Deposition in Seawater

The data in Figures III.B.1 and III.B.2 show that in the absence of calcareous deposits, the current required for cathodic protection decreases as the temperature decreases, and that the decrease is due to the effect of temperature on the diffusion coefficient of dissolved oxygen. In Figures III.B.3 through III.B.6 we show the effect of temperature on the current density required for the cathodic protection of steel in natural seawater. In seawater at 25°C, the measured current densities are approximately equal to those observed in sodium chloride at the beginning of the experiment, but the current density decreases with time due to the formation of calcareous deposits. After 6 days cathodic protection in natural seawater at 25°C, current densities are less than 20 $\mu amp/cm^2$ and continue to decrease with time. At 3°C in natural seawater (Figures III.B.3, III.B.4, III.B.5) the current density required for cathodic protection of steel in seawater is relatively constant at 50 to 60 $\mu amps/cm^2$ after the first few days. At 3°C the current density decreases slightly during the first several days of cathodic protection, which indicates a slight amount of deposit formation. After 1 week of cathodic protection, current requirements at 3°C are a factor of 3 higher than those at 25°C. The increased current requirements at 3°C must be due to inhibition of $CaCO_3$ and/or $Mg(OH)_2$ precipitation at low temperatures. The inhibition of deposit formation at 3°C could be due to several factors:

1. reduced rates of precipitation due to slower kinetics of precipitation at low temperatures;

2. reduced rates of precipitation due to slower diffusion of reactants to the steel surface; or

3. increased solubility of $CaCO_3$ or $Mg(OH)_2$ at low temperatures, either in the bulk solution or at the steel-seawater interface.

To determine if increased solubility of $CaCO_3$ or $Mg(OH)_2$ could cause the increased current densities observed at low temperatures in seawater, we calculated the degree of saturation of these two solids in the bulk seawater (Table III.B.6) and at the steel surface (Table III.B.7). The calculations in Table III.B.6 show that the seawater used in these experiments is always supersaturated with respect to $CaCO_3$, and once precipitated on the steel surface $CaCO_3$ should not dissolve into the bulk seawater. In contrast, $Mg(OH)_2$ is always greatly undersaturated in the bulk seawater and once formed will tend to dissolve into the bulk seawater. The data in Table III.B.7 show that the steel-seawater interface is initially greatly supersaturated with respect to $CaCO_3$. The percent saturation of $CaCO_3$ at the interface is approximately 10 times that in the bulk seawater. Interestingly, the interface is not highly supersaturated with respect to $Mg(OH)_2$. Considering the uncertainties in the solubility calculations at the interface, it is possible that the interface is actually undersaturated with respect to $Mg(OH)_2$.

The measurements of current density at 3°C (Figures III.B.3, III.B.4, III.B.5) all show a slight increase in current density with time after the first few days of cathodic protection. The increase in current density with time is accompanied by an

increase in the alkalinity of the seawater. Alkalinity, which is measured by titrating seawater with strong acid, is a measure of the equivalents of weak acid anions present in the seawater sample. In seawater the alkalinity is given by the following Equation,

$$\text{alkalinity} = (HCO_3^-) + 2(CO_3^{-2}) + (B(OH)_4^-) + (OH^-) \quad \text{(III.B.14)}$$

where the parentheses represent molar concentrations. We routinely measure alkalinity because deposition of $CaCO_3$ and $Mg(OH)_2$ on the steel electrode during cathodic protection results in a decrease in the alkalinity of the seawater in which the steel is immersed. The product of the alkalinity decrease times the volume of seawater in the corrosion cell is equal to the quantity of calcareous deposit which has formed.

However, the increase in alkalinity with time (Table III.B.8) observed in the 3°C seawater experiments cannot be explained by deposition of $CaCO_3$ or $Mg(OH)_2$. After investigating and eliminating several possible sources of contamination in our experiments, such as contamination of the laboratory air used to maintain constant pH and reaction of the seawater with the acyrlic walls of the corrosion cell, we found that the source of the alkalinity increase and of the current density increase was the formation of bromine, Br_2, at the platinum anode in the cell. The bromine formed at the anode

$$2Br^- = Br_2 + 2e^- \quad \text{(III.B.15)}$$

reacted with water to form hypobromite, OBr^-,

$$Br_2 + H_2O = H^+ + Br^- + HOBr \quad \text{(III.B.16)}$$

and the hypobromite then diffused to the steel cathode where it

was oxidized to bromide, Br^-,

$$OBr^- + H_2O + 2e^- = Br^- + 2OH^-. \qquad \text{(III.B.17)}$$

The formation of hypobromite, OBr^-, in Equation (III.B.16) removes hydrogen ions from the seawater and thus increases the alkalinity. The oxidation of hypobromite at the cathode causes the increase in current density observed in the 3°C experiments. During the experiments shown in Figures III.B.5 and III.B.6 we measured the hypobromite concentration in the seawater during the course of the experiments and the results are given in Table III.B.8.

The data in Table III.B.8 show that the concentration of hypobromite reached higher levels at 3°C than at 25°C. This may be due to the higher potential of the anode at 3°C (Table III.B.8) compared to 25°C, or it may be due to kinetic factors related to temperature effects on the rate of bromine production. We are currently studying methods to eliminate the formation of bromine in the corrosion cell. These include increasing the surface area of the anode to reduce the current density and thus potential at the anode, and the use of bromide free synthetic seawater.

BIBLIOGRAPHY (Section III A and B)

R. E. Andresen, P. O. Gartland, and E. Bardal: "Cathodically protected steel in sea water; polarization curves and cathodic reactions". SINTEF-report STF16 A81039, Trondheim 1981.

J. Billings and I. M. Ritchie, Electrochimica Acta, Vol. 25, p. 733 (1980).

J. O'M. Bockris and A. K. N. Reddy, "Modern Electrochemistry", Plenum, New York, 1973, p. 293.

C. H. Culberson, "Effect of seawater chemistry on the formation of calcareous deposits", paper no. 61 presented at CORROSION/83, April 18-22, 1983, Anaheim.

D. D. Dyrssen and I. Hansson, Marine Chemistry, Vol. 1, p. 137 (1973).

H. S. Harned and B. B. Owen, "The Physical Chemistry of Electrolytic Solutions", Reinhold, New York, 1958.

W. H. Hartt, C. H. Culberson, and S. W. Smith, "Calcareous deposits on metal surfaces in sea water - a critical review", paper no. 59 presented at CORROSION/83, April 18-22, 1983, Anaheim.

W. H. Hilbertz, "Electrodeposition of minerals in solution and its enhancement by biological growth for structural applications", Sea Grant Report No. 04-6-158-4111, Univ. of Texas, 1976.

R. A. Humble, Corrosion Journal, Vol. 4, p. 358 (1948).

D. R. Kester, "Dissolved Gases other than CO2", chapter 6, in: Chemical Oceanography, Vol. 1, 2nd edition, Academic Press, London, 1975.

A. Lerman, "Geochemical Processes Water and Sediment Environments", John Wiley & Sons, New York, 1979, p. 94.

Y.-H. Li and S. Gregory, Geochimica et Cosmochimica Acta, Vol. 38, p. 703 (1974).

F. J. Millero, Geochimica et Cosmochimica Acta, Vol. 43, p. 1651 (1979).

R. M. Pytkowicz, J. Geology, Vol. 73, p. 196 (1965).

R. M. Pytkowicz and R. F. Gates, Science, Vol. 161, p. 690 (1968).

T. R. S. Wilson, "Salinity and the Major Elements of Sea Water", chapter 6, in: Chemical Oceanography, Vol. 1, 2nd edition, Academic Press, London, 1975.

A. Windfeldt, Corrosion et Anticorrosion, Vol. 9, No. 1, p. 15 (1961).

H. H. Uhlig, "Corrosion and Corrosion Control", John Wiley & Sons, New York, p. 95 (1971).

FIGURE CAPTIONS (Section III A and B)

Figure III.A.1. Photograph of a typical calcareous deposit consisting of aragonite.

Figure III.A.2. Photograph of a calcareous deposit consisting of brucite, $Mg(OH)_2$.

Figure III.A.3. The effect of magnesium on cathodic protection of steel in synthetic seawater. Solution composition 0.50 NaCl + 0.03 Na_2SO_4 + 0.0025 $NaHCO_3$ + 0.05 $MgCl_2$; temperature = 25°C; potential = -0.90 Volt; rotation speed = 50 rpm; air saturation.

Figure III.A.4. The effect of calcium and magnesium on cathodic protection of steel in synthetic seawater of 35°/$_{oo}$ salinity. Temperature = 25°C; potential = -0.90 volt; rotation speed = 58 rpm; dissolved oxygen = 4.7 ml O_2/liter (air saturation).

Figure III.A.5. Effect of oxygen on current density during cathodic protection of steel in sodium chloride (0.50 NaCl + 0.0027 $NaHCO_3$). Temperature = 25°C; pH = 8.3; potential = -0.90 volt; rotation speed = 88 rpm.

Figure III.A.6. Effect of oxygen on current density during cathodic protection of steel in seawater of 29.7°/$_{oo}$ salinity. Temperature = 25°C; pH = 8.2; potentials = -0.80, -0.90, -0.992 volt; rotation speed = 105 rpm.

Figure III.A.7. Effect of seawater pH on current density during cathodic protection of steel in seawater of 29.7°/$_{oo}$ salinity. Temperature = 25°C; oxygen = 4.9 ml O_2/liter; potential = -0.90 volt; rotation speed = 89 rpm.

Figure III.A.8. Correlation of current density and seawater carbonate ion concentration. Data from Table III.A.3. Same conditions as Figure III.A.7.

Figure III.A.9. Effect of hydrogen evolution on potential versus current relationship in sodium chloride. Solution composition 0.70 NaCl + 0.0025 $NaHCO_3$; air saturation; temperature = 25°C; rotation speed = 50 rpm.

Figure III.B.1. Effect of rotation speed on current density during cathodic protection of steel at 25°C and 3°C. Solution composition 0.70 NaCl + 0.0025 $NaHCO_3$; potential = -0.90 volt; air saturation; experiment NOAA-5.

Figure III.B.2. Effect of rotation speed on current density during cathodic protection of steel at 25°C and 3°C. Solution composition 0.70 NaCl + 0.0025 $NaHCO_3$; potential = -0.90 volt; air saturation; experiment NOAA-6.

Figure III.B.3. Time variation of current density during cathodic protection of steel in seawater of 30°/$_{oo}$ salinity. Temperatures = 3°C and 25°C; potential = -0.90 volt; rotation speed = 50 rpm; air saturation; experiment NOAA-4.

Figure III.B.4. Time variation of current density during cathodic protection of steel in seawater of 30°/$_{oo}$ salinity. Temperatures = 3°C and 25°C; potential = -0.90 volt; rotation speed = 50 rpm; air saturation; experiment NOAA-9.

Figure III.B.5. Time variation of current density during cathodic protection of steel in seawater of 30°/$_{oo}$ salinity. Temperature = 3°C; potential = -0.90 volt; rotation speed = 50 rpm; air saturation; experiment NOAA-12.

Figure III.B.6. Time variation of current density during cathodic protection of steel in seawater of 30°/$_{oo}$ salinity. Temperature = 25°C; potential = -0.90 volt; rotation speed = 50 rpm; air saturation; experiment NOAA-13.

Table III.A.1. Solubility products of calcite, aragonite, and magnesium hydroxide in seawater of 35°/₀₀ salinity as a function of temperature and pressure (Hartt, Culberson, and Smith, 1983).

	***** 25°C *****		****** 2°C ******	
Solid phase	1 atm	400 atm	1 atm	400 atm
Calcite	4.6×10^{-7}	8.1×10^{-7}	4.8×10^{-7}	10.1×10^{-7}
Aragonite	6.7×10^{-7}	--	--	--
$Mg(OH)_2$	4.5×10^{-10}	--	2.8×10^{-10}	--

Table III.A.2. Chemical composition of 35°/₀₀ salinity seawater. The constituents listed include those whose concentrations exceed 1 part per million (Wilson, 1975).

Constituent	***** Concentration ******* (mol/liter)	(gram/liter)
Na^+	0.479	11.02
Mg^{+2}	0.0543	1.320
Ca^{+2}	0.01052	0.422
K^+	0.01044	0.408
Sr^{+2}	0.000092	0.0081
Cl^-	0.559	19.80
SO_4^{-2}	0.0289	2.775
HCO_3^-	0.00234	0.143
Br^-	0.000862	0.0689
F^-	0.000070	0.00133
$B(OH)_3$	0.000426	0.00460

Table III.A.3. Effect of pH on current density requirements for cathodic protection in seawater. Salinity = 29.73°/$_{oo}$, temperature = 25°C. Dissociation constants of carbonic acid were taken from Millero (1979).

pH	TCO_2	HCO_3^-	CO_3^{-2}	pCO_2	$a_{on} \times 10^6$
	**** micromolar ****			(ppm)	
8.16	1788	1618	158	402	1.4
8.65	1502	1151	348	93	4.5
8.41	1655	1405	245	196	2.6
8.24	1749	1557	183	322	1.7
7.47	2022	1914	38	2332	0.3
8.15	1792	1625	155	413	1.4

Table III.B.1. Chemical concentrations and diffusion coefficients in air saturated sodium chloride at 25°C and 3°C. Solution composition is 0.70 molar NaCl plus 0.0025 molar $NaHCO_3$. Oxygen solubilities from Kester (1975), oxygen diffusion coefficients from Lerman (1979), hydroxide diffusion coefficients from Li and Gregory (1974).

Temperature	Dissolved oxygen (μmol/liter)	pH	Diffusion Coefficient (cm^2/sec)	
			Oxygen	Hydroxide
25°C	211	8.39	2.1×10^{-5}	5.3×10^{-5}
3°C	333	8.23	1.1×10^{-5}	2.8×10^{-5}

Table III.B.2. The average value of the ratio of current densities at 25°C and 3°C in 0.70 molar NaCl plus 0.0025 molar $NaHCO_3$ (air saturated) calculated from the data in Figures III.B.1 and III.B.2 at rotation greater than 5 rpm.

Experiment	Ratio of current densities
Figure III.B.1	1.42 ± 0.05
Figure III.B.2	1.53 ± 0.03

Table III.B.3. Thickness of the laminar layer, Δx, calculated from Equation (III.B.5) and the data given in Figure III.B.2.

Rotation speed (rpm)	Laminar layer thickness (microns)	
	25°C	3°C
0	398	551
10	381	473
50	147	185
100	97	123
175	68	88

Table III.B.4. The pH and hydroxide ion concentration at the steel surface during cathodic protection in an unbuffered solution of bulk pH = 8.0 from Equation (III.B.10).

Temperature	pH	Hydroxide ion concentration
25°C	10.28	3.4×10^{-4} mol/liter
3°C	11.30	5.2×10^{-4} mol/liter

Table III.B.5. The pH, hydroxide, and inorganic carbon concentrations at the steel surface during cathodic protection in a buffered sodium chloride solution (0.70 NaCl plus 0.0025 $NaHCO_3$) of bulk pH = 8.0. TCO_2 is the total concentration of dissolved inorganic carbon. Ionization constants of carbonic acid from Dyrssen and Hansson (1973), of water from Harned and Owen (1958).

	Concentration (μmolar)									
	**** Bulk solution *****					******* Interface ********				
Chemical species	CO_2	HCO_3^-	CO_3^{-2}	OH^-	pH	CO_2	HCO_3^-	CO_3^{-2}	OH^-	pH
25°C	21	2079	60	1.8	8.0	0	1019	1412	85	9.7
3°C	31	2129	36	0.3	8.0	0	319	2314	110	10.6

Table III.B.6. Saturation state of seawater with respect to $CaCO_3$ and $Mg(OH)_2$ at 25°C and 3°C. Seawater pH = 8.2, alkalinity = 2100 μeq/l, 31°/₀₀ salinity. Ionization constants of carbonic acid, boric acid, and water from Millero (1979).

Temperature	***** Percent Saturation ******		
	Calcite	Aragonite	$Mg(OH)_2$
25°C	423	282	0.5
3°C	231	154	0.01

Table III.B.7. Saturation state of the steel-seawater interface with respect to $CaCO_3$ and $Mg(OH)_2$ at 25°C and 3°C. These calculations are only valid for time zero in which there is no calcareous deposit on the steel surface.

Temperature	***** Percent Saturation ****		
	Calcite	Aragonite	$Mg(OH)_2$
25°C	2900	1900	140
3°C	4200	2800	410

Table III.B.8. Production of hypobromite and alkalinity changes in natural seawater during the cathodic protection of steel (-0.9 volt versus SCE).

Elapsed time (hours)	Alkalinity (μeq/l)	HOBr (μmol/l)	Anode potential (volts vs. SCE)
**********	3°C	**********	
0	2096	0	+1.52
119	2307	--	
171	2392	256	
265	2510	305	
**********	25°C	**********	
3	2103	0	+1.38
45	2035	61	
117	2004	68	

Figure III.A.1

Figure III.A.2

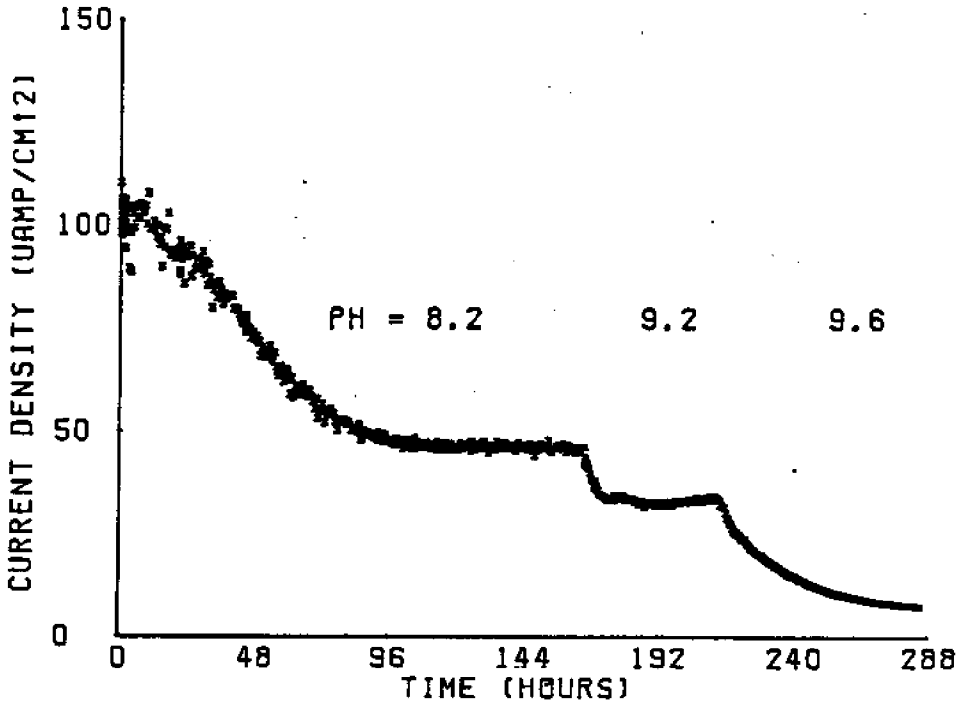

Figure III.A.3

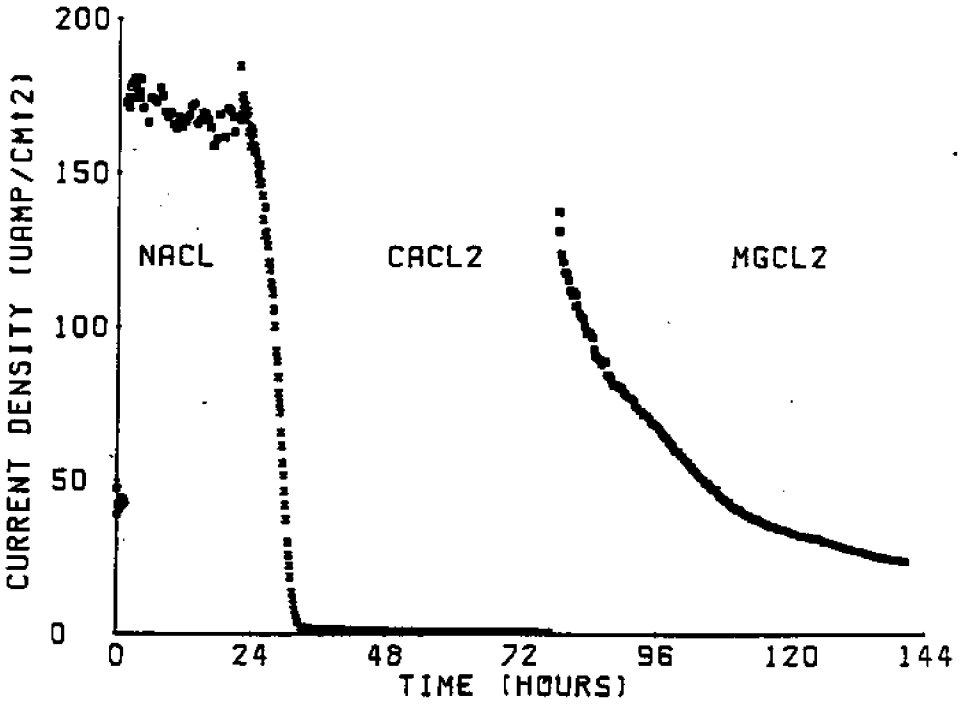

Figure III.A.4

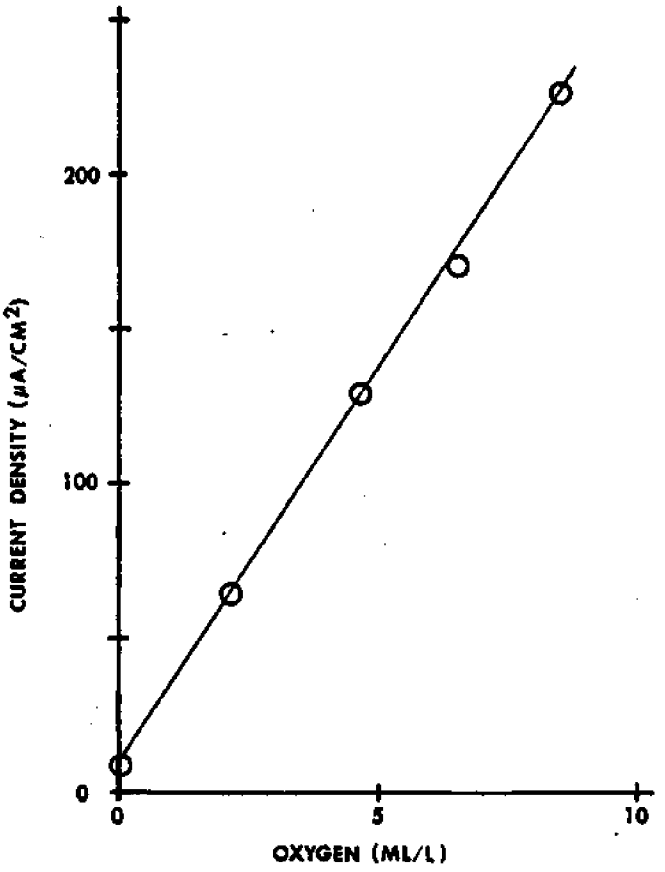

Figure III.A.5

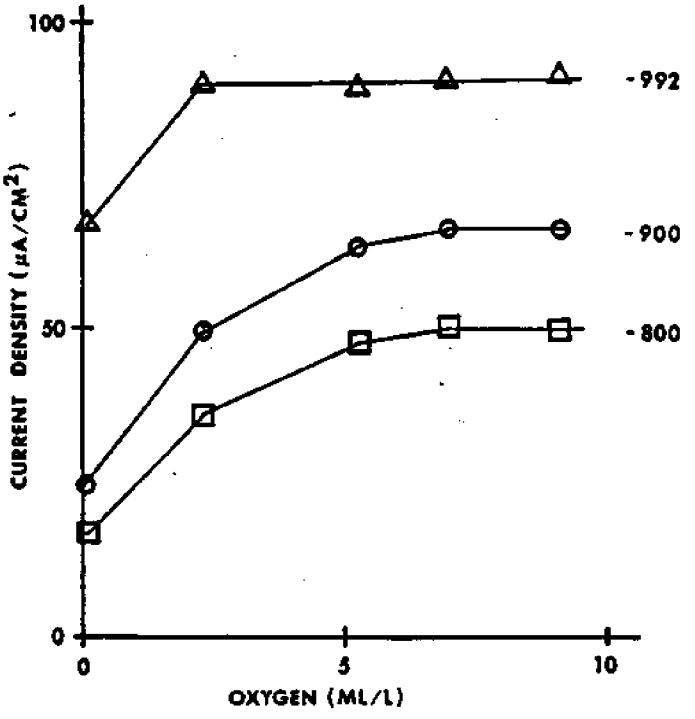

Figure III.A.6

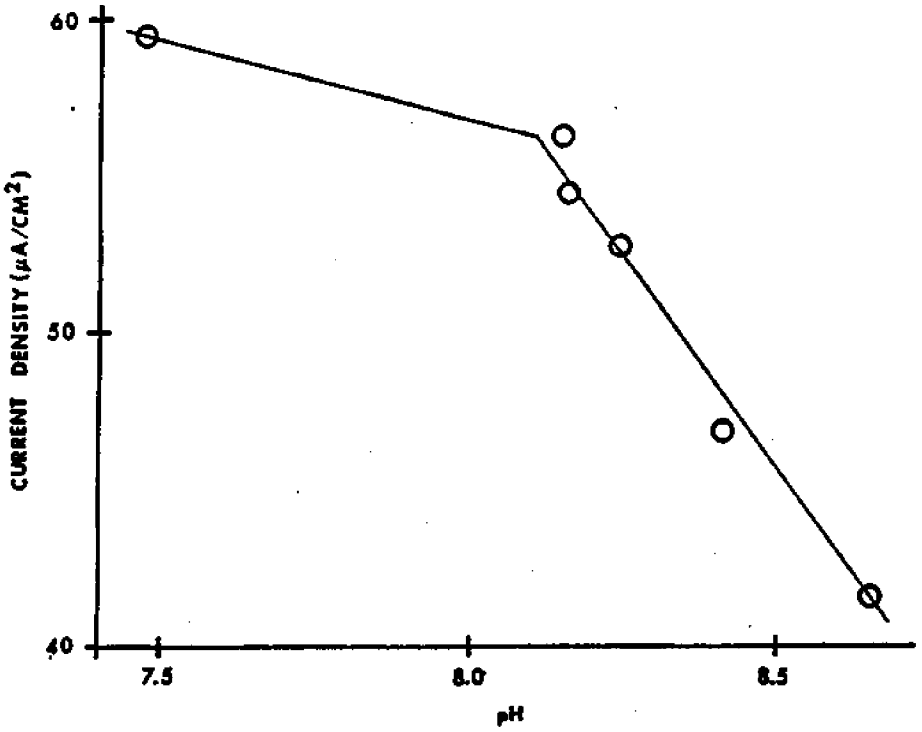

Figure III.A.7

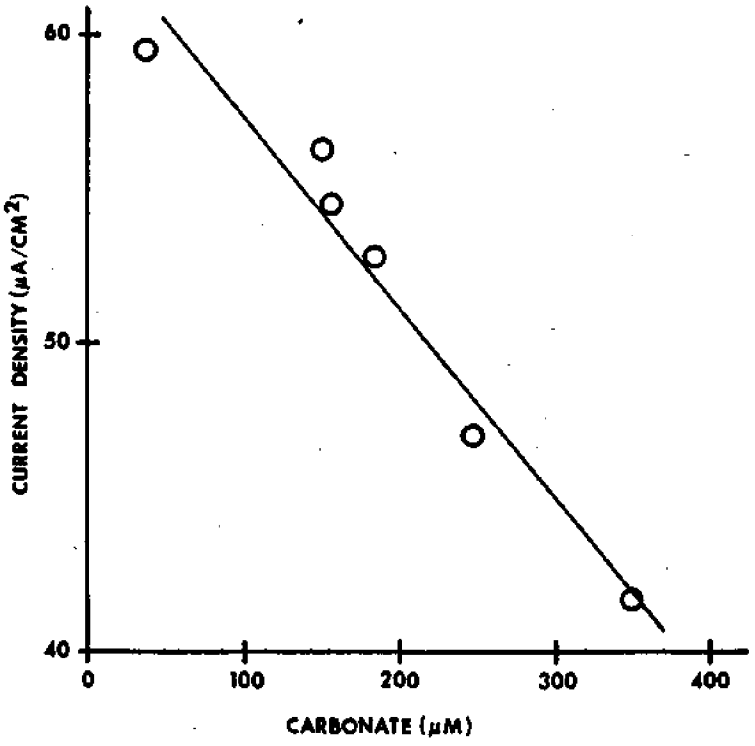

Figure III.A.8

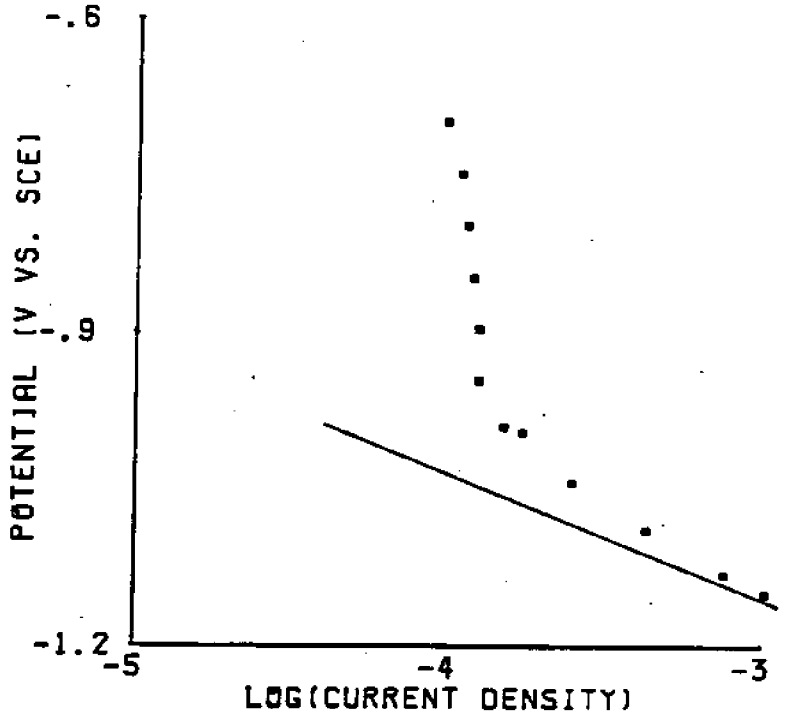

Figure III.A.9

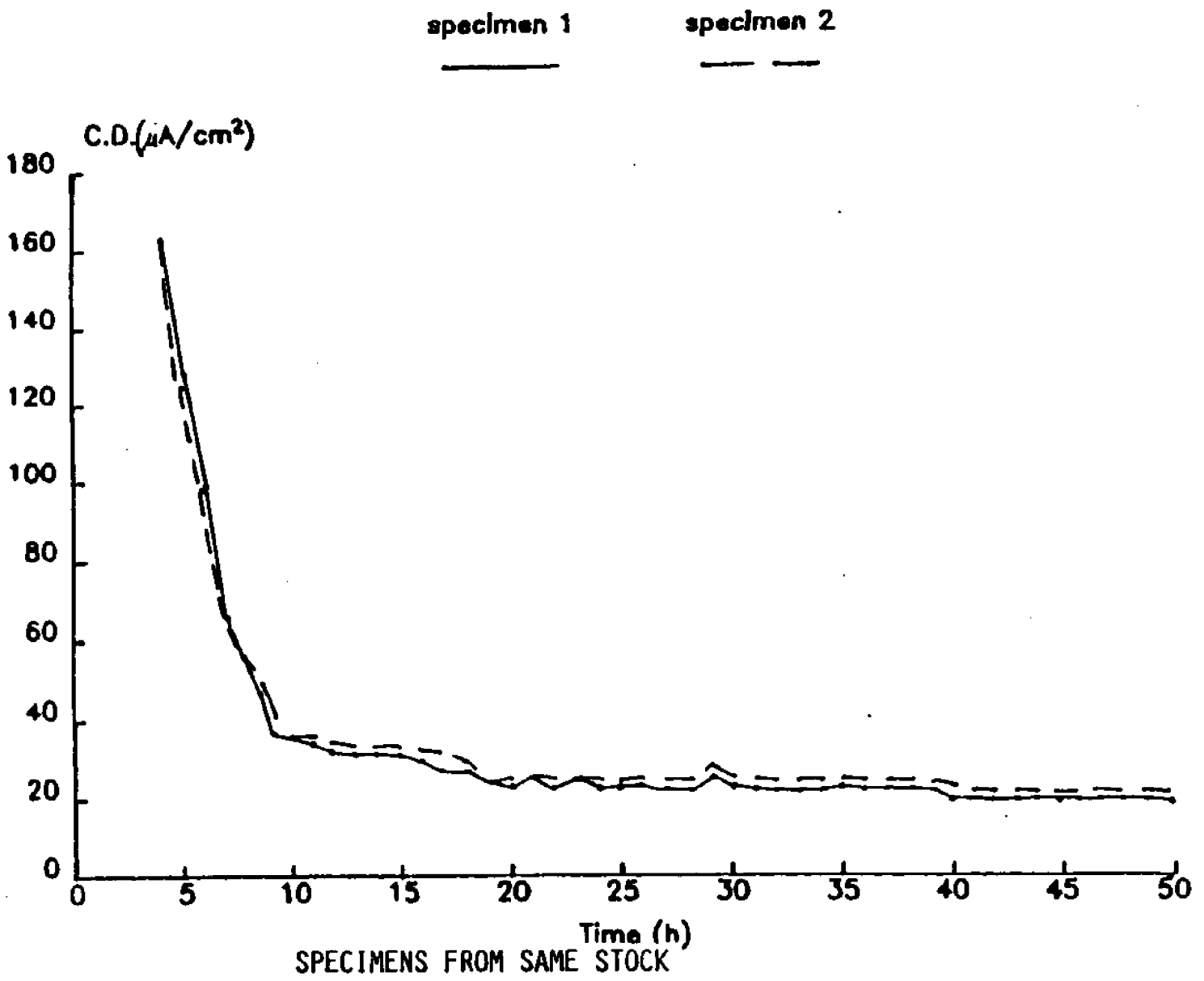
specimen 1
specimen 2
C.D.(μA/cm²)
180
160
140
120
100
80
60
40
20
0
0
5
10
15
20
25
30
35
40
45
50
Time (h)
SPECIMENS FROM SAME STOCK

FIG. III.A.10

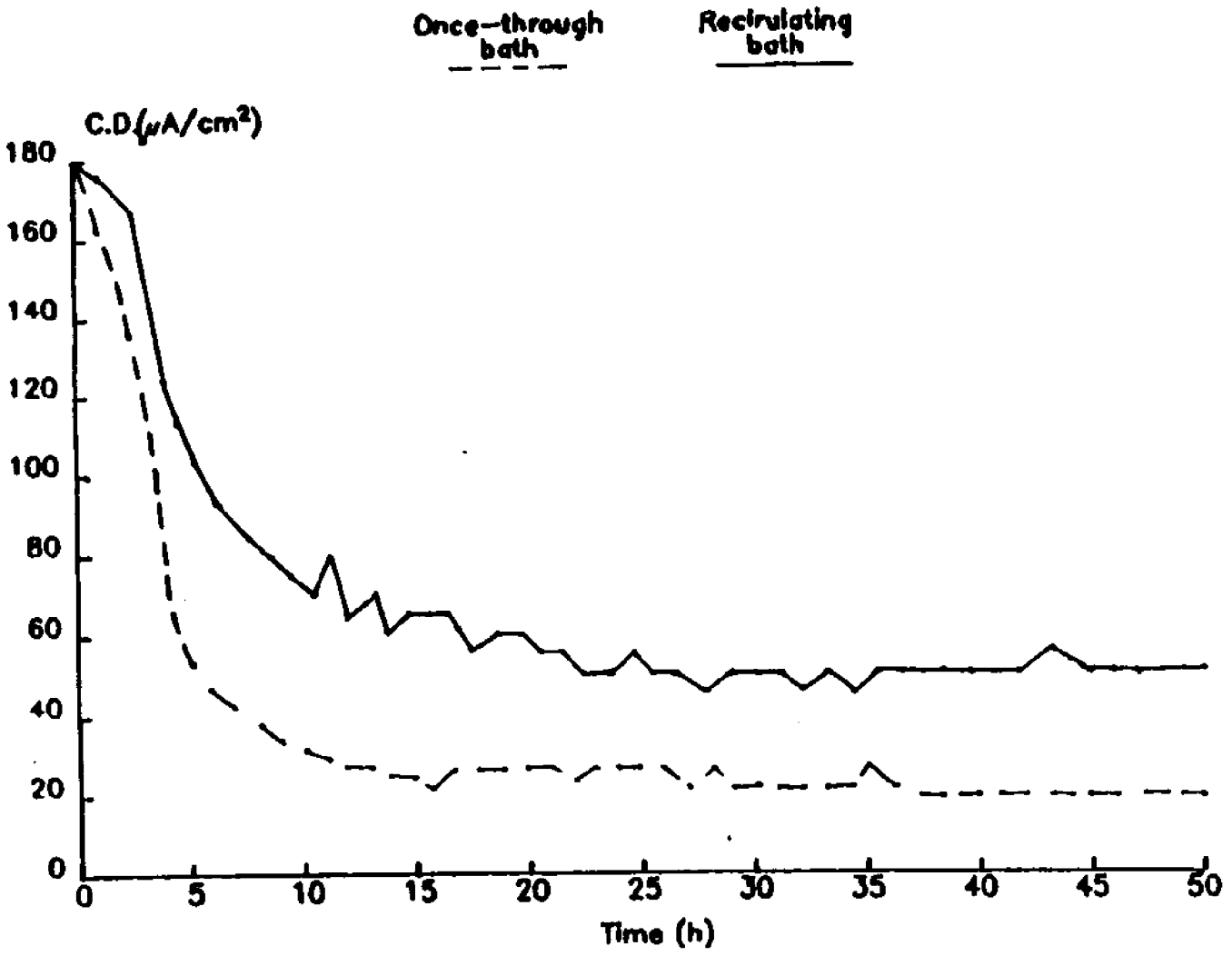

RECIRCULATING AND ONCE-THROUGH BATHS

FIG.III.A.11

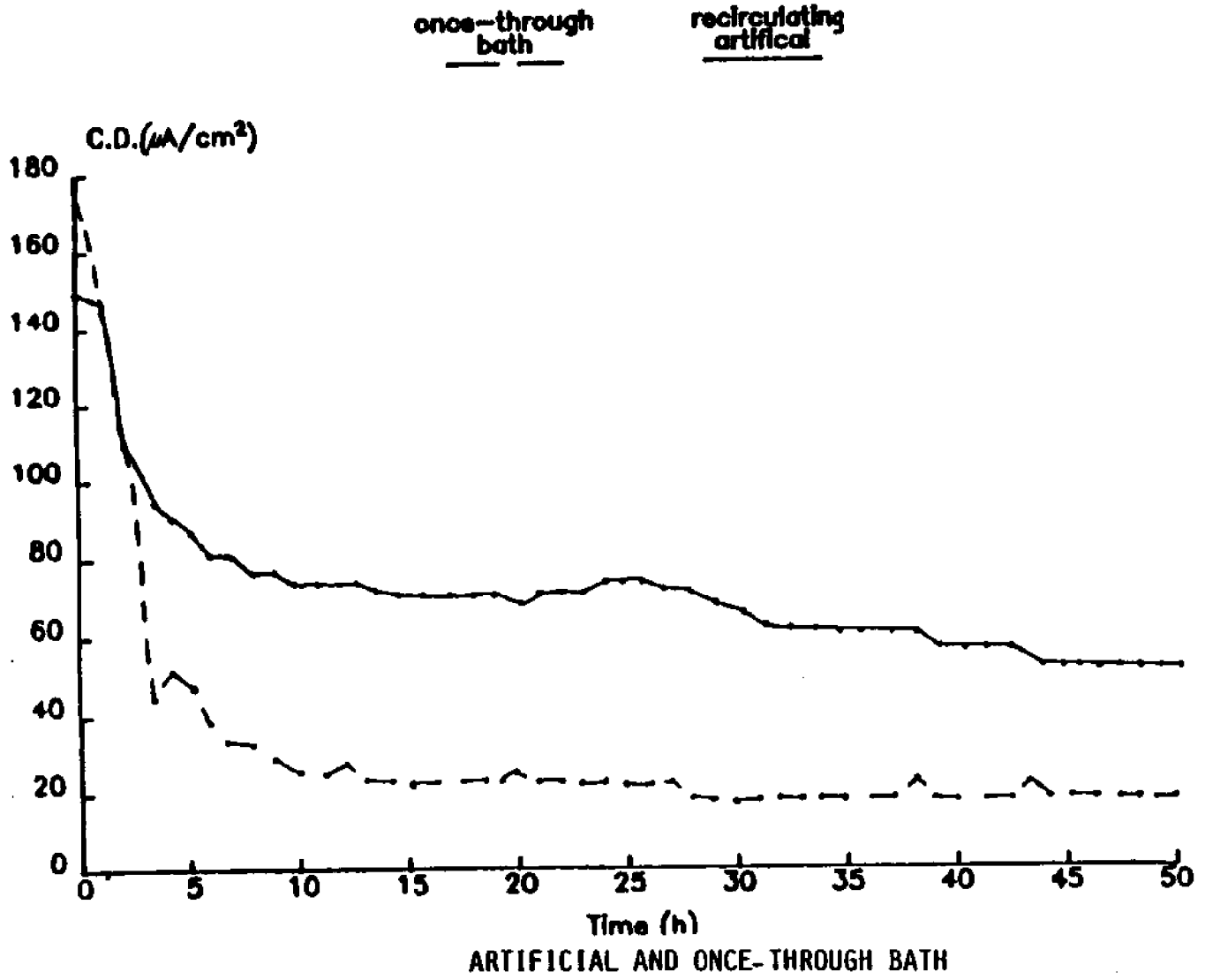

ARTIFICIAL AND ONCE-THROUGH BATH

FIG.III.A.12

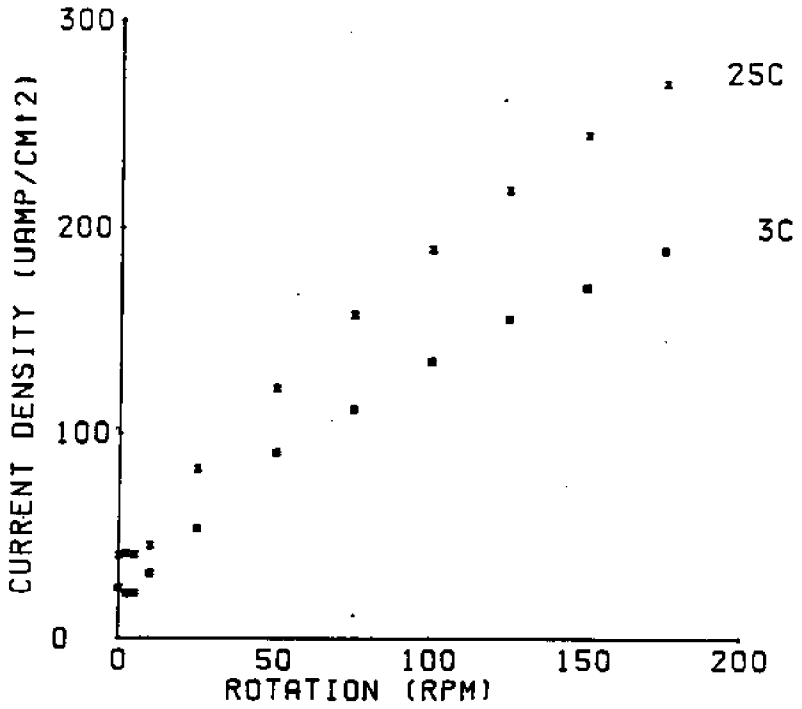

Figure III.B.1

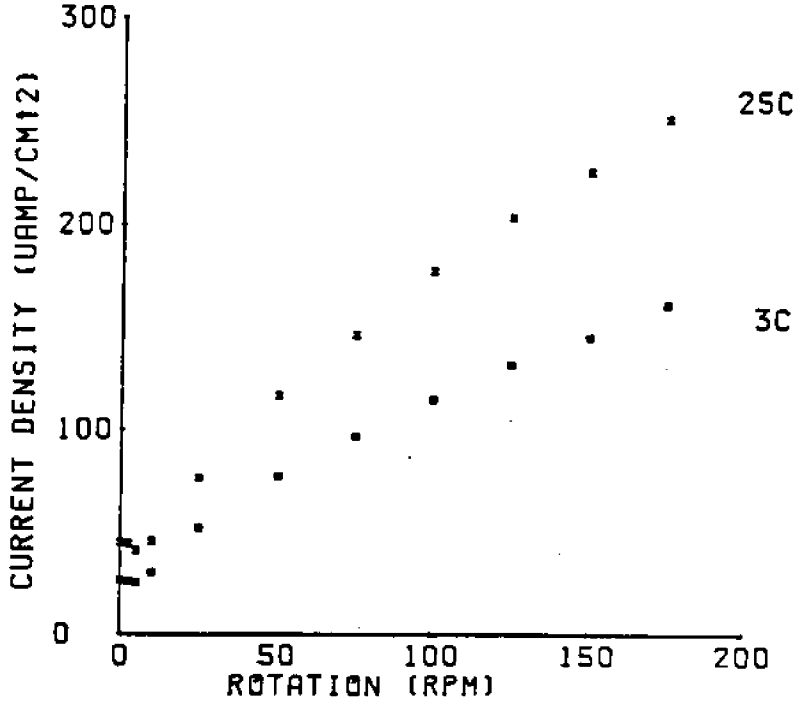

Figure III.B.2

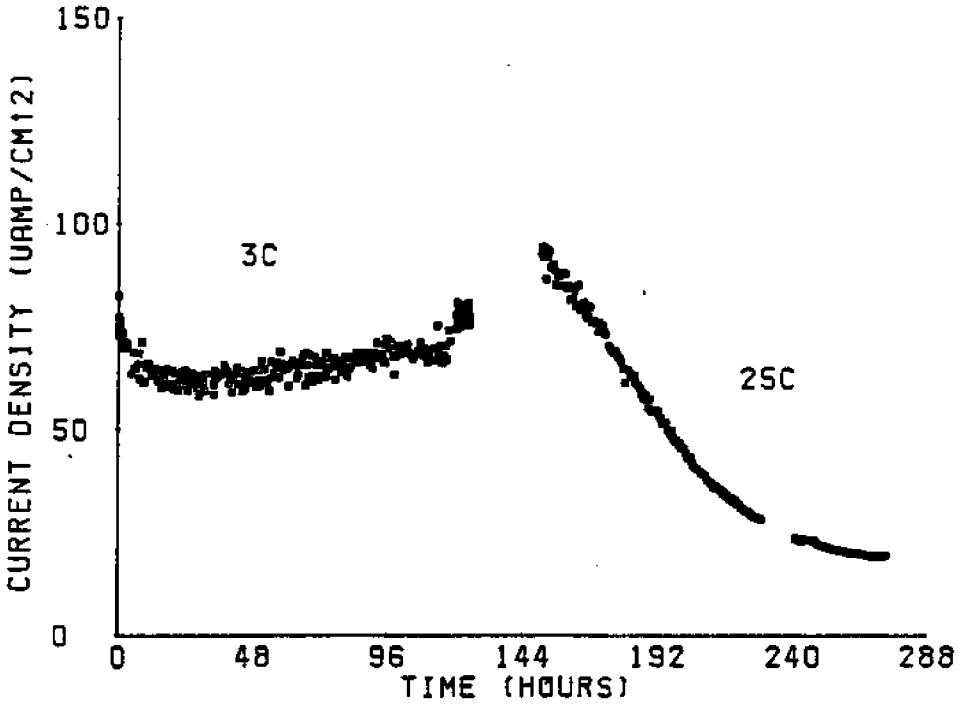

Figure III.B.3

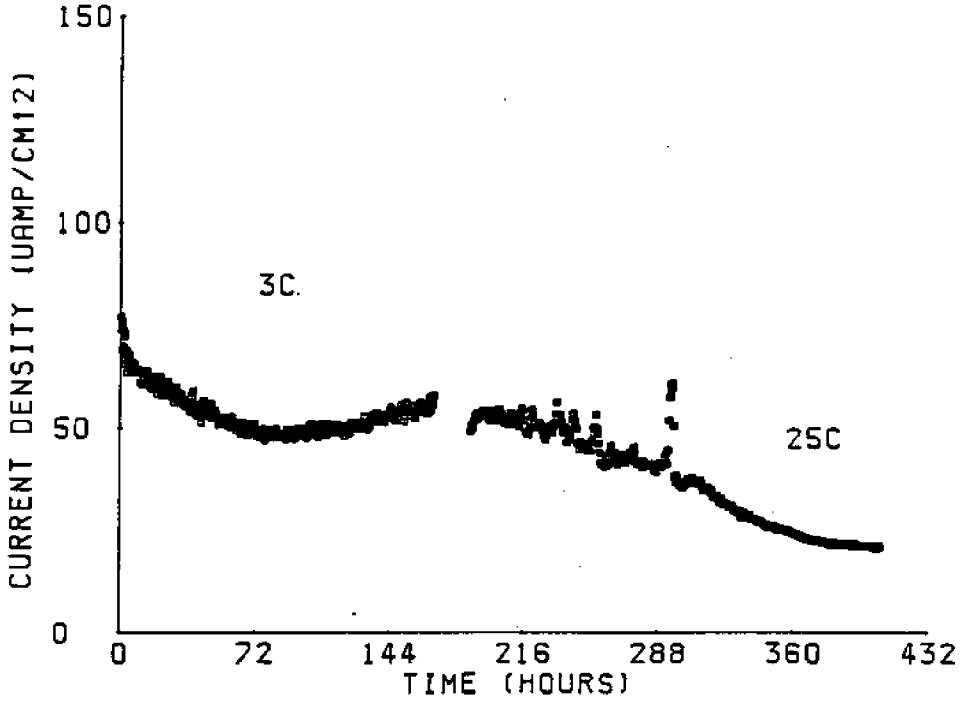

Figure III.B.4

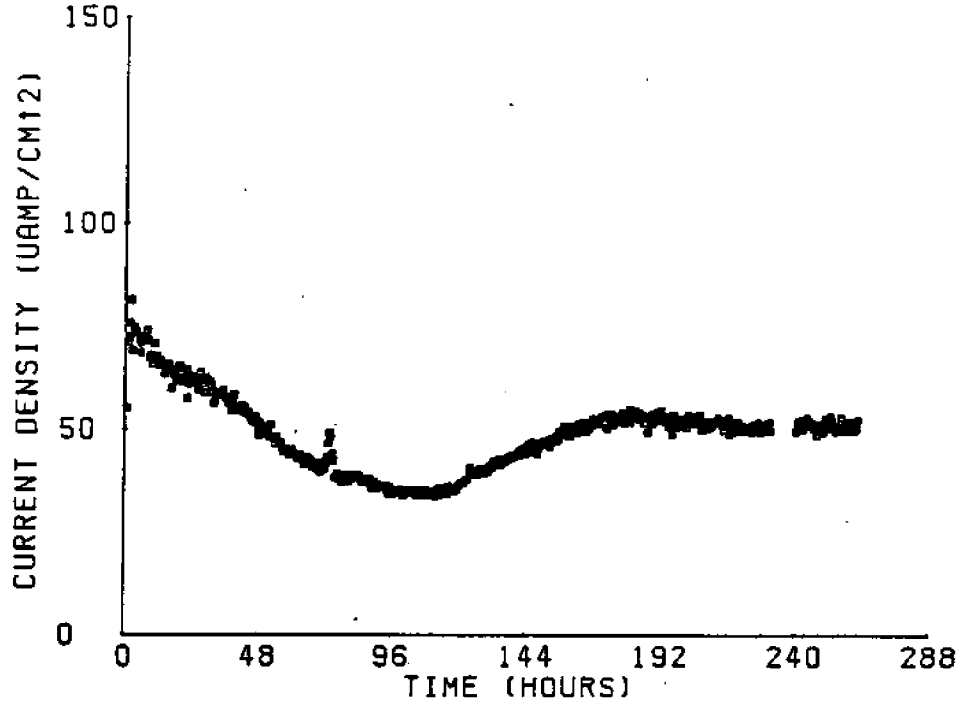

Figure III.B.5

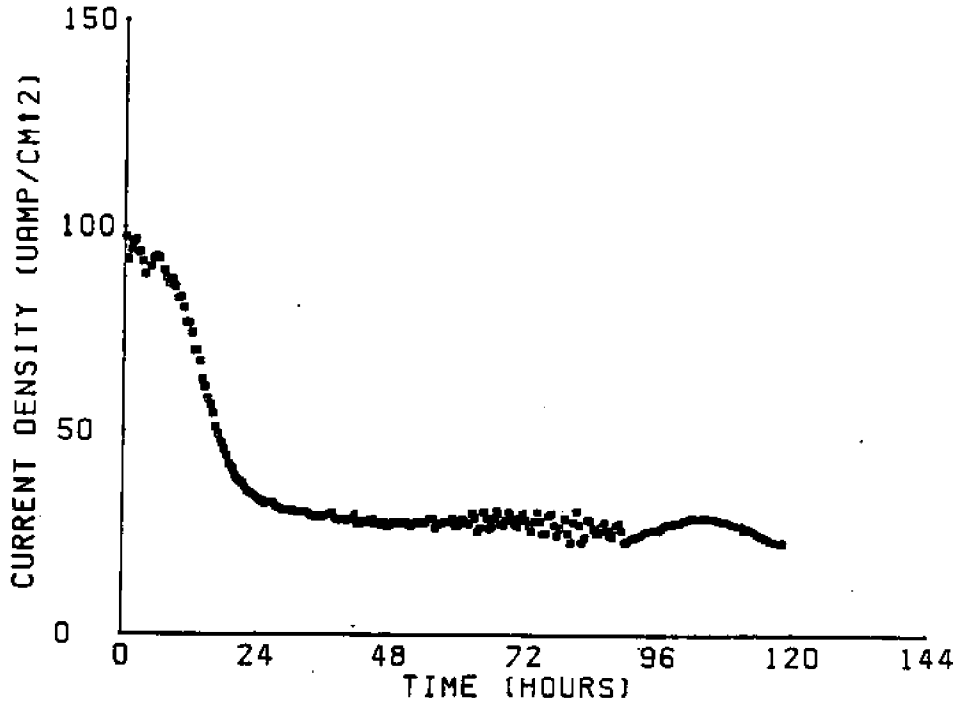

Figure III.B.6

III.C Hydrodynamics

III.C.1 Rotating Disk Experiments

A series of experiments were run to investigate the effect of velocity on deposit morphology and protectivity using the rotating electrode assembly described previously. The specimen was fabricated from iron supplied by Climax Molybdenum. Rotational speeds of 0, 250, 500, 1000, and 2500 rpm were used.

In the curve for polarization under stationary conditions (Figure III.C.1), three distinct regions can be seen. In the region denoted A-B, metal dissolution and oxygen reduction occur simultaneously; in regions B-C, cathodic reduction of oxygen and complimentary film deposition takes place; and in region C-D, hydrogen evolution occurs. This figure is analogous to Figure III.A.13. The higher current in the latter case is probably due to the slower rotation speed. When compared to Figure III.A.1 the limiting current densities are equal. With increased rotation speed the plateau region for oxygen reduction became less pronounced. Current was no longer mass transport limited, but approached Tafel conditions of charge transfer control.

For all cyclic step galvanodynamic sweep curves presented in Figure III.C.2, hysteresis loops can be seen. For stationary conditions and at 250 rpm, broader hysteresis loops were obtained than for the specimens rotated to 500, 1000, and 2500 rpm. The magnitude of the hysteresis loop is associated with the electrical resistance of the calcareous deposit produced at the more negative potentials.

The morphology of the deposits as affected by relative solution velocity can be seen from SEM micrographs taken directly from electrodes which were cathodically polarized in natural seawater at various rotational speeds, dried in a nitrogen stream, dipped in deionized water and dried again in the nitrogen stream.

There is distinct difference in appearance between specimens polarized under stationary conditions and at 250 rpm rotation speed (Figures III.C.3 and III.C.4) and those polarized at 1000

and 2500 rpm (Figures III.C.5 and III.C.6). Whereas the stationary and the 250 rpm group form a dense film of sub-micrometer (0.1 to 0.5 um) globules, the 1000 and 2500 rpm group form larger globules of approximately 1um. This could imply that at the higher current densities required by the higher rotation speeds a more porous film is formed. There are no distinct differences within the 0 or 250 rpm and the 1000 or 2500 rpm groups.

Several instrumental methods were used in attempts to characterize deposit composition as a function of velocity and impressed current density. Unfortunately, the only unambiguous conclusion which could be drawn from a comparison of measurements obtained from various techniques was that the results were ambiguous. For instance, from the comparison between SEM-EDAX spectra of extraction replicas for deposits formed under stationary conditions in natural seawater (Figure III.C.7) and deposits formed at 250 rpm (Figure III.C.8) several features dominate:

1. In addition to calcium, magnesium, and sodium being present, aluminum, silicon, sulfur, chloride, and phosphorus are also present.

2. Deposits under flowing conditions contain considerably less calcium than under stagnant conditions. Relative concentrations of other elements are also effected, but not in any predictable manner with increased solution velocity (Figure III.C.9, 1000rpm). Of course, the rough nature of the replica surfaces prevented any meaningful analysis of compositional variations. X-ray images which correspond to these spectra do show, however, that the elements are rather well dispersed throughout the area from which the spectra were obtained.

Electron microprobe elemental analyses (EPMA) and count distribution of surface deposit compositions show the ratio decreases with increasing velocity.

An attempt to resolve differences in the EDAX and EPMA analyses by dissolving deposits was attempted. The deposits were predipped in distilled water to remove excess NaCl and then dissolved in 6 ml of 0.5 mm HCl solution. The results again confirm the difficulty in relating deposit compositions to seawater velocity. The one meaningful feature of this experiment was that for deposits grown for extended periods of time calcium content was dramatically increased under stagnant conditions.

Auger electron spectroscopy (AES) was used to obtain depth profiles of the composition of the films. Figure III.C.10 shows a typical AES spectrum, and Figures III.C.11 and III.C.12 present the depth profile at two rotational speeds. Note that the spectra must be treated cautiously since adsorbed monolayers may influence the results due to the shallow sample depth of AES. In all the spectra the oxygen and iron intensities were extremely high, implying that a major component of the deposit was iron hydroxide or oxide (oxychloride). Since the spectrum does not show the elements P, K, Al, Si, and S it would appear that these elements are concentrated near the metal deposit interface.

Magnesium and calcium did show a definite pattern with depth in the film and with solution velocity. The compiled depth profiles for these elements are given in Figure III.C.13. Of some interest is the fact that the Mg/Ca peak height ratio goes through a minimum at a distance from the surface which is more or less dependent upon relative seawater velocity (for example, Figure III.C.14 at 250 rpm). A plot of sputtering depth where this Ca/Mg ratio maximum occurs versus square root of rotation velocity is given in Figure III.C.15 and indicates that deposit compositions are controlled by transport of both calcium and magnesium ions to the surface of the growing deposit and that concentrations of these ions change with exposure time.

There is no question but that increased seawater velocity necessitates increased impressed current density in order to maintain a prescribed degree of cathodic protection in terms of some established protection potential. However, the consequences of any elevated current density requirements with respect to

modification of environmental chemistry at the metal/seawater interface is not completely clear. Furthermore, if one assumes precipitation of insoluble material from a supersaturated solution to be controlled by nucleation and growth processes, then it must be recognized that conditions are not necessarily the same during growth as they were during initiation.

The parabolic dependence of the initial impressed current density on relative seawater velocity as determined from the plateau regions (B-C) in Figure III.C.1 indicates that solution mass transport controls cathode reaction kinetics (Figure III.C.15). Also shown in Figure III.C.15 is a plot of impressed cathodic current density versus square root of electrode rotation velocity after one hour of cathodic protection. Although mass transport control is clearly evident, the difference in slope reflects a difference in control between nucleation and growth processes of calcareous deposit formation. It is likely that oxygen diffusion through the electrolyte controls impressed current density requirements during early stages, while transport of some other species, presumably one which is incorporated into the deposit, controls the oxygen flux and hence the current requirements during later stages of deposit development.

Assuming this to be the case, then with increasing relative solution velocity, cathodic current density will be proportional to interfacial oxygen concentration as long as available surface area for the electrochemical process is unchanged (i.e. no deposit forms). Interfacial hydroxide ion concentration is proportional to both oxygen concentration and relative velocity. This is in contrast to Wolfson and Hartt (1981) who have suggested that metal surface hydroxide ion concentration should be inversely proportional to solution velocity.

It is therefore reasonable to conclude that increased interfacial pH results in nucleation of deposits which contain a higher ratio of magnesium to calcium. Results of Humble (1948) and the AES results of this work tend to support this conclusion. Although deposit composition will be controlled by the ease with

which individual compounds can precipitate from supersaturated solution, it is interesting to note that magnesium hydroxide, when precipitated, lowers hydroxide concentration by 2 equivalents per mole of magnesium ion. Intuitively then, it could be deduced that those species which make up the bulk of the deposit will be those which tend to resist further increases in surface pH.

Of much greater importance, however, is the effect of impressed current density on deposit morphology. There is an increasingly nodular appearance for deposits grown under conditions of higher relative solution velocity and impressed current density. The nodules resemble crystal "blooms" in that they probably result from a precipitation process which is not uniformly distributed across the surface of the electrode which is receiving the impressed cathodic current. Since solution supersaturation results from changes caused by the electrochemical reduction process, it can only be assumed that impressed current density is also not uniform across the surface, but concentrated at areas of low deposit electrical resistance. Whatever the origin of these sites, localized high cathodic current density results in rapid hydroxide production and increased precipitation of magnesium hydroxide. Since there is a definite relationship between current density, solution velocity, composition and nodule size, it must be concluded that, for whatever reason, areas with low electrical resistance to current flow correspond to areas of high magnesium hydroxide concentration. As seen in Figure III.C.2 least hysteresis and, hence, lowest surface resistance occurred with highest impressed currents and rotational velocities.

III.C.2 Flat Plate Experiments

In another set of experiments a segmented steel plate as described elsewhere was used to study the effect of water velocity on current distribution (Figure II.D.1). Two velocities have been examined, 64cm/sec and 125cm/sec. In addition two potentials were used.

Results from these studies are presented in Figures III.C.16, 17, and 18. In each case the current density at the leading edge of the plate is higher than that on the remainder. This suggests that velocity is not the key variable controlling hydrodynamic effects. For example, the current density appears to be a stronger function of fluid shear than velocity. As time progresses in the test the current profile flattens out and overall current density drops. This is due to the formation of calcareous deposit.

Comparing specimens run at the same potential but different velocities (Figures III.C.16 and III.C.17) it can be seen that while the initial current requirements are considerably higher in the 125 cm/sec than the 64 cm/sec, however after 75 hours the values converge. This suggests that fluid flow is less important after the deposit has formed.

Figure III.C.19 shows a comparison of total cathodic current for 64 cm/sec at -900 mV and -1000 mV. After approximately 50 hours the film formed at -900 mV is less protective than that formed at -1000 mV. This agrees with the results of Wolfson (1978).

In order to gain a quantitative understanding of hydrodynamic effects on the formation of calcareous deposits it is necessary to look at diffusion of ions to and from the surface during flow. In the simple case where there is no significant flow or surface deposits, mass transfer from the solution to the surface would be controlled by Fick's First Law:

$$i_\ell = DmF\ dC/dX \qquad \text{(III.C.1)}$$

where dC/dX is concentration gradient, D is diffusivity, m is valence, i_ℓ is the limiting current, and F is Faraday's constant. Rewriting:

$$i_\ell = DmF\ Cb/\delta d \qquad \text{(III.C.2)}$$

where Cb is the bulk concentration and d is the diffusional boundary layer thickness. For the condition of laminar flow with no surface deposit the above equation is still valid so long as the correct d is used. The diffusional boundary layer is related to the hydrodynamic boundary layer h for laminar flow by the Schmidt Number ($Sc = \gamma/d$) via the following equation (Gartland 1980):

$$\delta h/\delta d = \alpha\ Sc^{a} \qquad \text{(III.C.3)}$$

where α is equal to 1 and a equals 1/3. Thus the following:

$$\delta d = \delta h/Sc^{1/3} \qquad \text{(III.C.4)}$$

Substituting (III.C.4) into (III.C.2),

$$i_{\ell} = DmF\ Cb\ Sc^{1/3}\ /\delta h \qquad \text{(III.C.5)}$$

Now for laminar flow over a flat plate δh is give by:

$$\delta h = 5X/\ Re^{1/2} \qquad \text{(III.C.6)}$$

By substituting (III.C.6) into (III.C.5) one obtains

$$i_{\ell} = DmF\ Cb\ Sc^{1/3}\ Re^{1/2}\ /5X \qquad \text{(III.C.7)}$$

Noting the following relation (Wolfson 1978):

$$i_{\ell} = KmF\ Cb \qquad \text{(III.C.8)}$$

where K is the mass transfer coefficient, and by combining (III.C.7)and (III.C.8) a dimensionless expression can be obtained as below:

$$\text{Sherwood Number} = KX/D = 0.323\ Sc^{1/3}\ Re^{1/2}\ . \qquad \text{(III.C.9)}$$

Notice that for a given set of physical conditions the Schmidt Number is a constant and therefore the current is related to the square root of the Reynold's Number. However, a quick glance at the experimental data obtained for a flat plate (Figures III.C. 16, 17, and 18) will show that the results are not a function of the square root of Reynold's Number, but are in fact a much weaker function.

An examination of the plate used in the experiment would reveal it to be somewhat less than ideally smooth. For this

reason this likely resulted in the flow being tripped to turbulence at or very near the beginning of the plate and therefore the flow over the plate was turbulent. A quantitative analysis of a turbulent flow is more complicated than a laminar flow. In general a statistical approach must be used. However, in this case only diffusion through the boundary layer is of interest. If one makes the assumption that eddy diffusion dominates in the turbulent region of the boundary layer then this layer will most likely be well mixed on the time scale of molecular diffusion through the laminar sublayer. For this reason only diffusion through the laminar sublayer need be considered.

The theory relating molecular diffusion through a laminar sublayer has not been completely formulated. However, investigators have developed a dimensionless expression based on convective transfer of heat and momentum across a flat plate in turbulent flow (Knudsen and Katz 1958). This expression can be extended into the area of mass transfer.

For a flat plate in turbulent flow the dimensionless expression analogous to that for heat transfer on a flat plate can be written as:

$$\text{Sherwood Number} = KX/D = \frac{(f/2)\ Re\ Sc}{1 + (U/V)\ (Sc - 1)} \qquad \text{(III.C.10)}$$

where f is local function factor and (U/V) is the ratio of velocity in the laminar sublayer to that in the turbulent core. The value of f in turbulent flow as defined by Robertson and Crowe 1980 is:

$$f = 0.058/Re^{1/5} \qquad \text{(III.C.11)}$$

The term (U/V) is given by (Eckert an Gross 1963):

$$(U/V) = \frac{1.305}{Sc^{1/6}\ Re^{1/10}} \qquad \text{(III.C.12)}$$

Substituting Equations III.C.11 and III.C.12 into III.C.10 yields the dimensionless expression:

$$\text{Sherwood Number} = KX/D = \frac{0.0292\ Re^{4/5} SC}{1 + 1.305\ Sc^{-1/6} Re^{-1/10} (Sc-1)} \quad \text{(III.C.13)}$$

Solving for the mass transfer coefficient for turbulent flow in Equation III.C.13 and substituting into III.C.8 yields:

$$i = \frac{0.0292\ DmF\ Cb\ Sc\ Re^{4/5}}{x(1+1.305\ Sc^{-1/6}\ Re^{-1/10}\ (Sc-1)} \quad \text{(III.C.14)}$$

Note that in Equation (III.C.14) the current is a function of less than 0.8 power of Reynold's Number. This gives a much better qualitative match to the previously discussed experimental data (Figures III.C.16, 17, and 18) than Equation (III.C.7) which is for laminar flow.

The last issue addressed under the topic of flow effects is the role of the calcareous deposit. Returning to Fick's First Law (Equation (III.C.1)):

$$i_{\ell} = DmF\ dC/Dx \quad \text{(III.C.1)}$$

The diffusion process in the presence of a deposit can be treated in two parts, diffusion through the deposit and diffusion through the boundary layer. In the boundary layer diffusion is governed by the following:

$$i_{\ell} = DmF\ (Cb - Ct)/\delta d \quad \text{(III.C.15)}$$

where Ct is the concentration at the film's surface. Diffusion through the calcareous deposit is given by:

$$i_{\ell} = kD\ell mF\ (Ct - Cs)/t \quad \text{(III.C.16)}$$

where k is the porosity of the deposit, t is the thickness of the deposit, and Cs is the concentration at the surface (for oxygen this is zero). Noting that both of these must be equal at the interface and by algebra:

$$Cb = \frac{i_l(k\delta d + t)}{kDmF} \qquad \text{(III.C.17)}$$

Solving for i:

$$i_l = \frac{kDmF\ Cb}{k\delta d + t} \qquad \text{(III.C.18)}$$

Note that as the thickness of the deposit increases the effect of the boundary layer decreases. Velocity should have little effect after a certain film thickness determined by the ratio of the product of boundary layer thickness and porosity to deposit thickness. This is in fact what is observed in Figures III.C.16 and 17.

III.D. Substrate

To answer the question of how reproducible polarization results are with respect to different mild steel substrates the following experiment was undertaken. The tests were performed in a rotating cylinder apparatus, which has been previously described, operated under stationary conditions. Seawater for all experiments was that available at FAU. Flow rate through the test cells was 1 liter per minute in all cases. The test duration was at approximately 48 hours. Each experiment was done in triplicate to assure reproducible results.

Initial control experiments involved specimens cut from different mild steel rods. Figure III.D.1 shows typical current decay curves for this set of experiments. As the calcareous deposit formed on the steel surface the current decayed. These curves show poor correlation with each other, especially during the first 15 to 30 hours when the deposit is initially forming. Note that variations on the order of seventeen percent occurred when different rods were employed. Once the current densities had stabilized the correlation was better. When specimens cut from the same bar were used, reproducible current densities were obtained. A typical set of results can be seen in Figure III.A.10.

The fact that mild steel specimens machined from different bars gave significantly different polarization results during the initial period of film formation was unexpected. This was apparently due to differences in the kinetic activity of the steel surfaces. What caused these differences in unknown at the present time, however, an energy dispersive X-ray analysis with an ORTEC EEDS II Quantitative Unit revealed no chemical differences in the steels. This technique could not determine the carbon content of the steel, but it is difficult to rationalize how small variations in the carbon present could significantly effect the results. Additional experiments are required to better rationalize this observation. The present experiments indicate, however, a need for obtaining specimens from the same material stock.

III.E. Pressure Effects

In an initial phase of this three year effort high pressure experiments were performed under the direction of Dr. Robert H. Heidersback (Formerly with University of Rhode Island but presently at Cal Poly State University). Two publications and a doctoral dissertation resulted from this. The present section is intended as an overview of these experiments.

The tests were performed employing a zinc-iron corrosion cell that was exposed to Sargasso Sea surface water pressurized via a laboratory pressure vessel to from 1.0×10^5 to 6.5×10^6 pascals. Pressure-wise this corresponded to water depth extremes of 0 and 645 m. Temperatures of both 6 and 22°C were employed. Exposure duration was for as long as 789 hours. Scanning electron microscopy and energy dispersive x-ray spectra analysis were performed on the iron surfaces subsequent to exposure and these revealed that the deposits were magnesium rich with relatively little calcium. This was the case for both the ambient and high pressure experiments. For the case of the ambient pressure test this contrasts with results reported above, where deposits were primarily comprised of $CaCO_3$. This may have been due to the fact that the sea water electrolyte was of finite volume and non replenished. Also, no effort was made in these experiments to duplicate any property of deep ocean water other than pressure and temperature (oxygen concentration, pH and organics, for example). These experiments, coupled with the results in Section III.A - D, strongly infer that subtle aspects of exposure may have a major effect upon calcareous deposits structure and properties and that deep ocean simulation experiments would take all of these factors into account.

The low temperature and sea water chemistry results may, however, be used to project cathodic protection requirements under deep ocean exposure conditions. Thus, low temperature, pH and oxygen concentration, as are likely to occur with increasing depth, have a negative influence upon calcareous deposit formation. In addition, increasing pressure should result in

enhanced calcium carbonate and magnesium hydroxide solubility. Hence, it is anticipated that higher current densities are necessary for cathodic protection under this condition.

BIBLIOGRAPHY (Section III.C)

Eckert E.R.G., INTRODUCTION TO HEAT AND MASS TRANSFER, McGraw-Hill, N.Y., 1963.

Gartland, P.O., "Effects of Flow on the Cathodic Protection of a Steel Cylinder in Seawater", SINTEF Report No. STF16 F80007, Trondheim, Norway, 1980.

Humble, R.A., "Cathodic Protection of Steel in Seawater with Magnesium Anodes", CORROSION, V. 4, p. 358, 1948.

Knudsen, J.G. and Katz, D.L., FLUID DYNAMICS AND HEAT TRANSFER, McGraw-Hill, N.Y., 1958.

Robertson, J.A. and Crowe, C.T., ENGINEERING FLUID MECHANICS, 2nd Ed., Houghton Mifflin Co., Boston, MA., pp. 320-340, 1980.

Wolfson, S.C., EFFECT OF CATHODIC POLARIZATION AND SEA WATER VELOCITY UPON CALCAREOUS DEPOSIT FORMATION ON MILD STEEL, M.S.O.E. Thesis, Florida Atlantic University, December 1978.

Wolfson, S.C. and Hartt, W.H., "An Investigation of Calcareous Deposits Upon Cathodic Steel Surfaces in Seawater", CORROSION, V. 37, p. 70, 1981.

FIGURE CAPTIONS (Section III.C-D)

Fig.III.C.1	Current Density vs. Potential for Different Rotation Speeds
Fig.III.C.2	Current Density vs. Potential Plots Demonstrating Hysteresis Loops
Fig.III.C.3	Surface Morphology at 0 RPM
Fig.III.C.4	Surface Morphology at 250 RPM
Fig.III.C.5	Surface Morphology at 1000 RPM
Fig.III.C.6	Surface Morphology at 2500 RPM
Fig.III.C.7	SEM-EDAX Spectra of Extraction Replica for Deposit Formed at 0 RPM
Fig.III.C.8	SEM-EDAX Spectra of Extraction Replica for Deposit Formed at 250 RPM
Fig.III.C.9	SEM-EDAX Spectra of Extraction Replica for Deposit Formed at 1000 RPM
Fig.III.C.10	Typical Auger Spectrum for Deposit
Fig.III.C.11	Auger Depth Profile for 0 RPM
Fig.III.C.12	Auger Depth Profile for 250 RPM
Fig.III.C.13	Depth Profiles for Ca and Mg vs. Velocity
Fig.III.C.14	Ca/Mg Auger Peak Height as a Function of Depth for 250 RPM
Fig.III.C.15	Depth of Ca/Mg Maximum vs. Square Root of Rotation Velocity
Fig.III.C.16	Current Density Distribution along Flat Plate at -900mV and 125cm/sec
Fig.III.C.17	Current Density Distribution along Flat Plate at -900mV and 64cm/sec
Fig.III.C.18	Current Density Distribution along Flat Plate at -1000mV and 64cm/sec
Fig.III.C.19	Current Density vs. Time at Controlled Potentials and -900mV and 64cm/sec
Fig.III.D.1	Current Density vs. Time for Specimens Cut From Different Stock

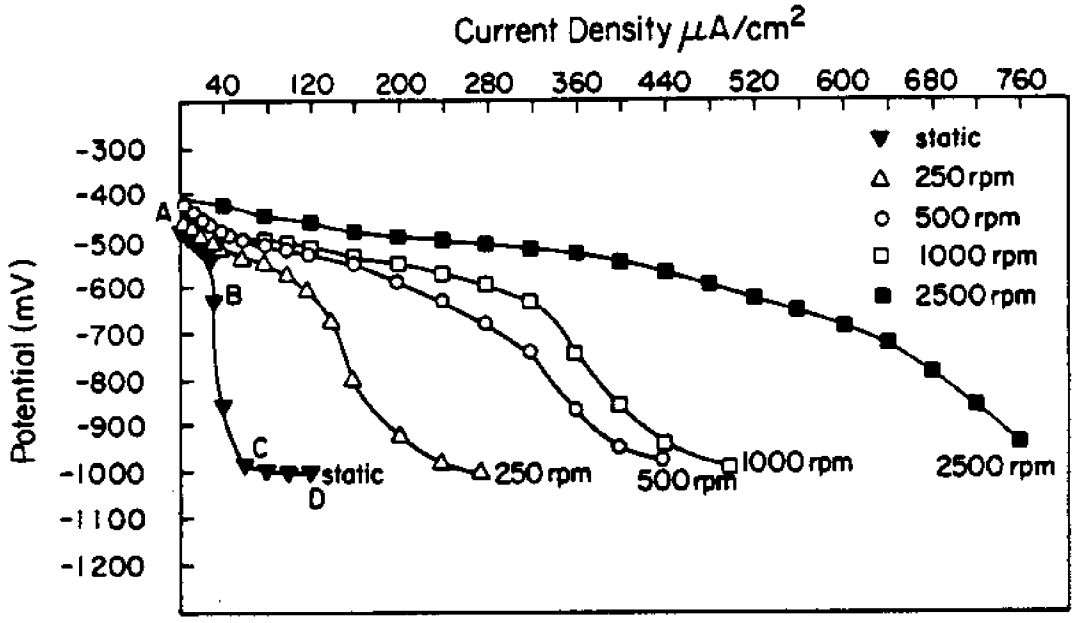

Fig.III c. 1

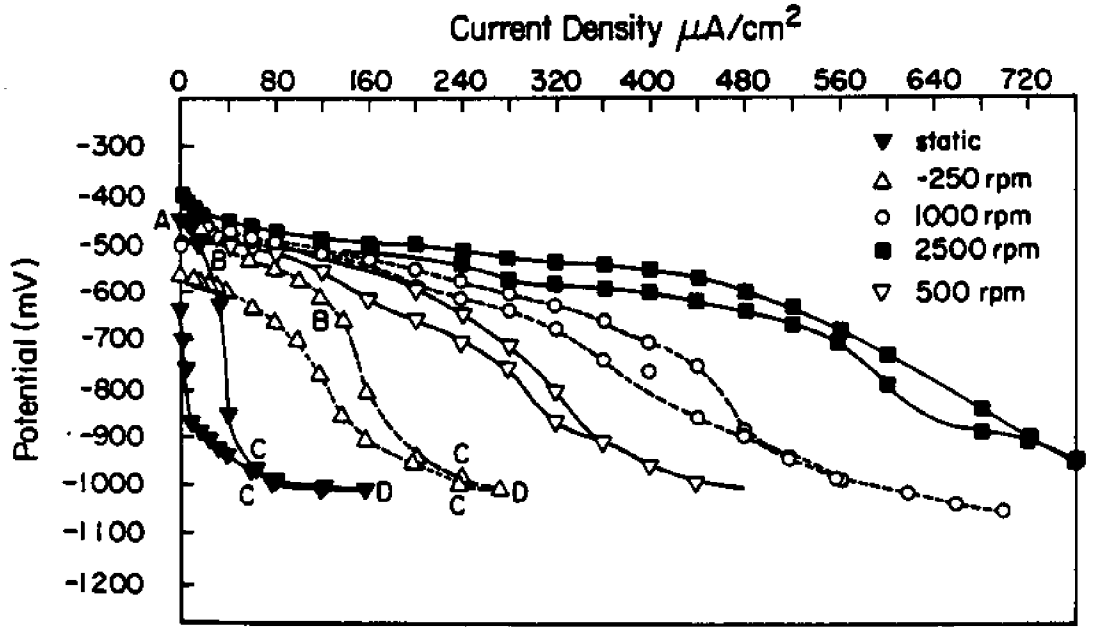

Fig.III c. 2

Fig. III c.3

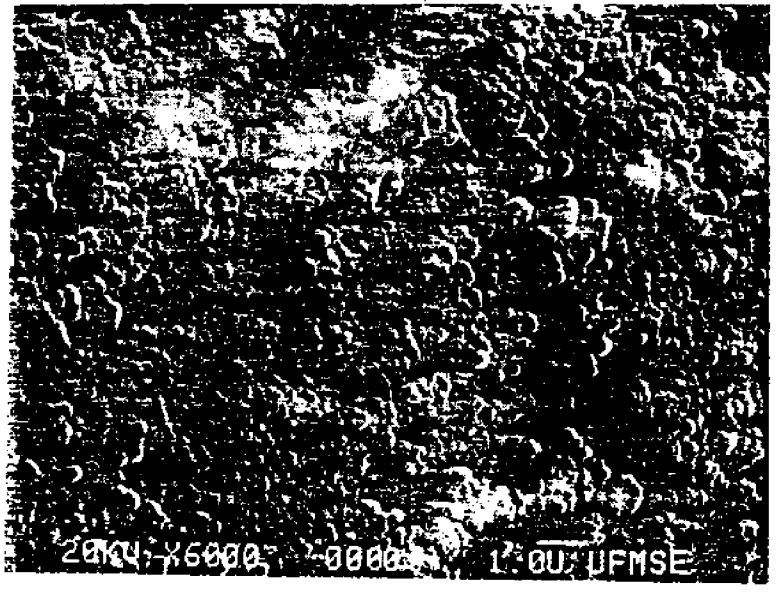

Fig. III c.4

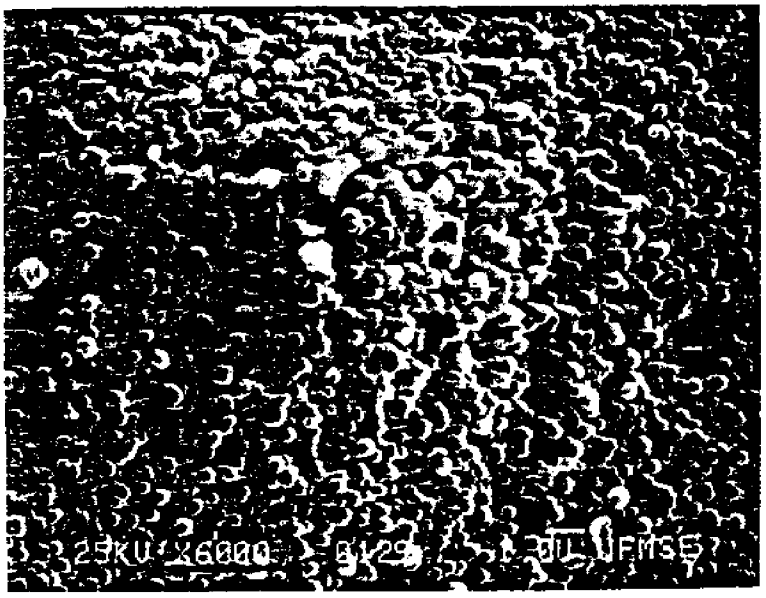

Fig. III c.5

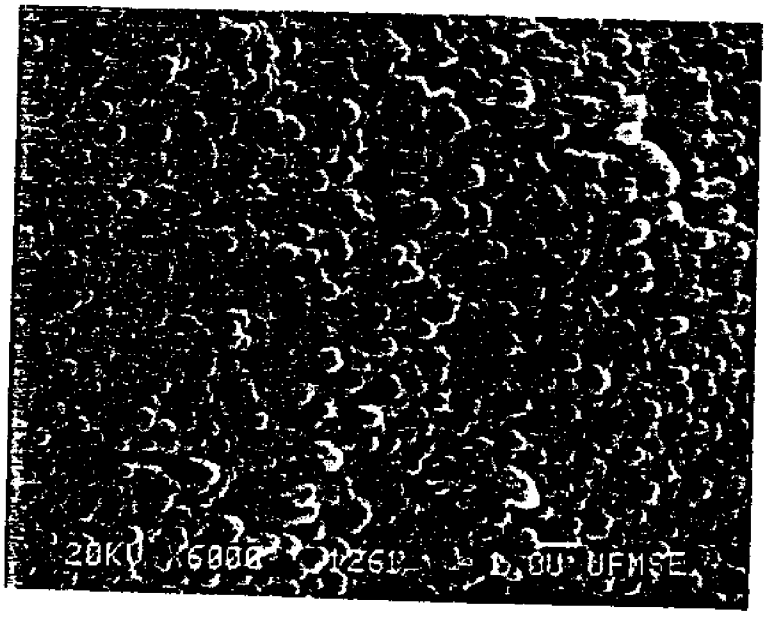

Fig. III c.6

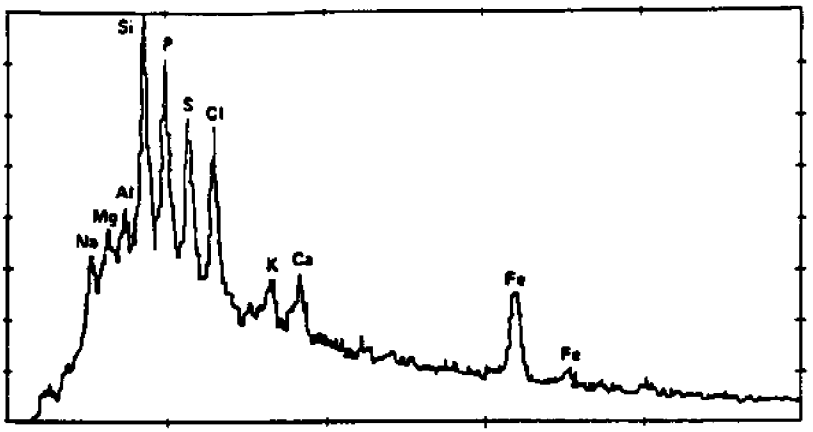

Fig. III c.7

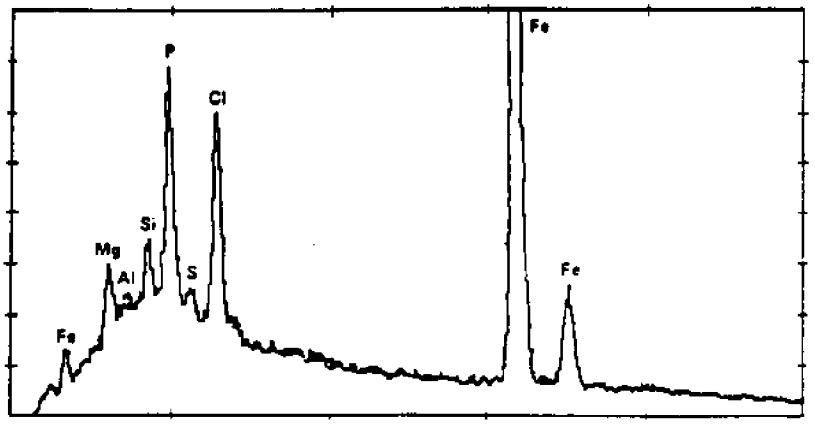

Fig. III c.8

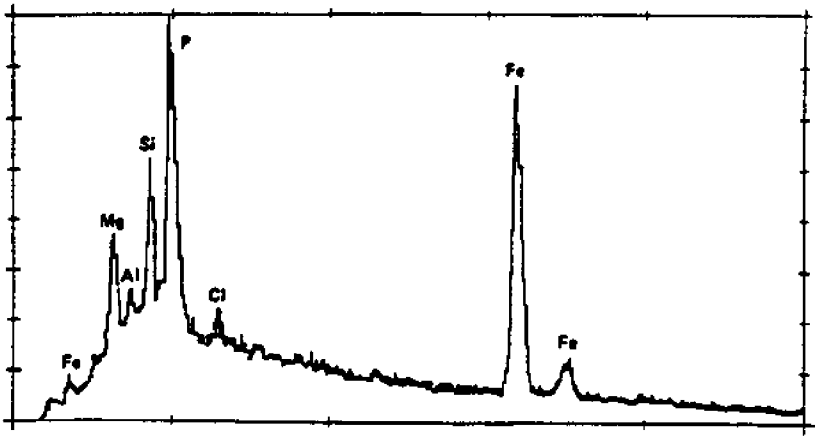

Fig. III c.9

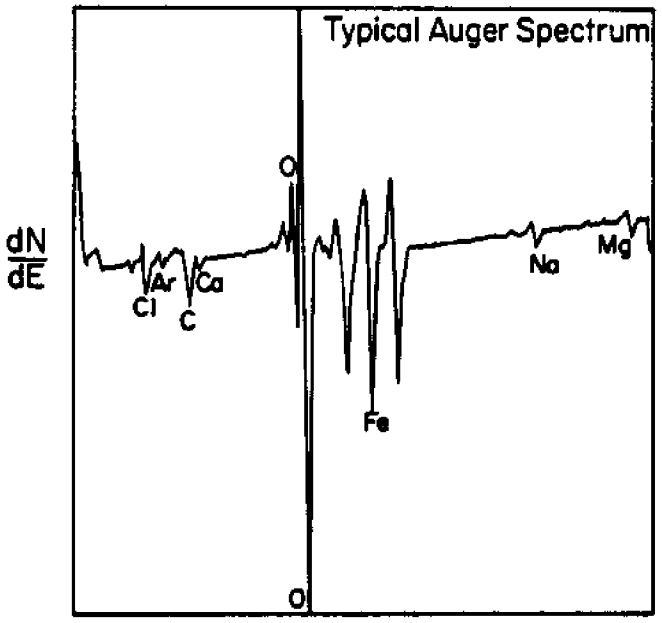

Fig. III c.10

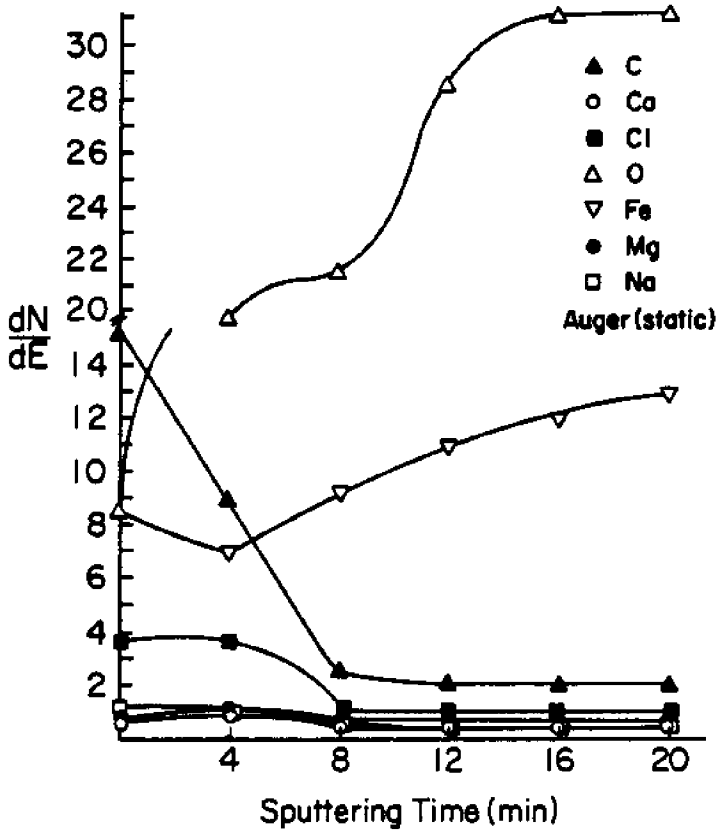

Fig. III c.11

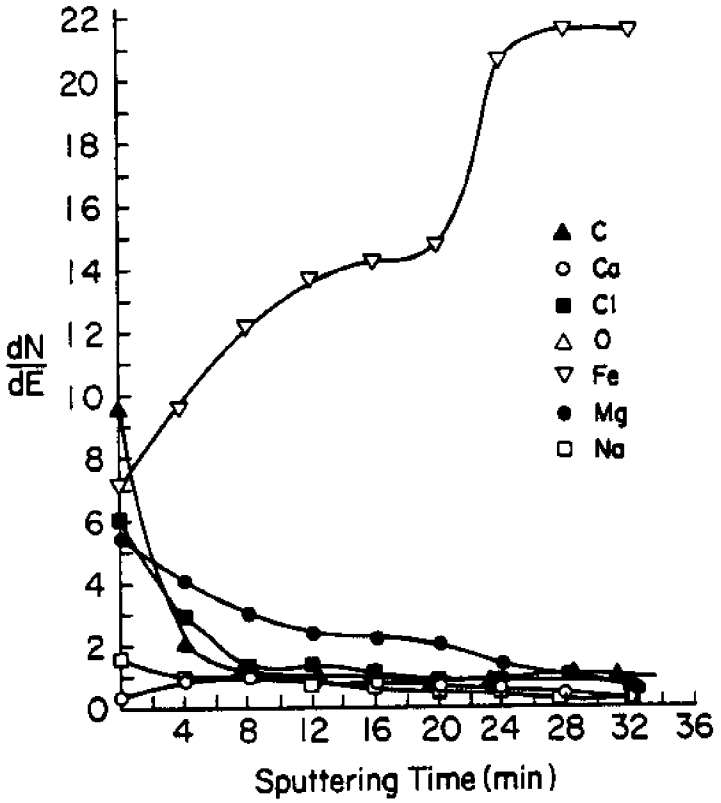

Fig.III c.12

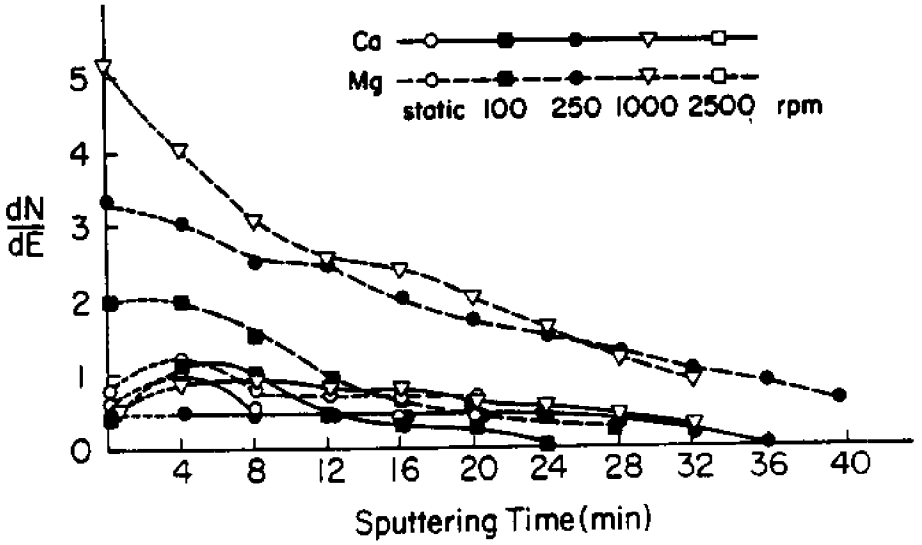

Fig.III c.13

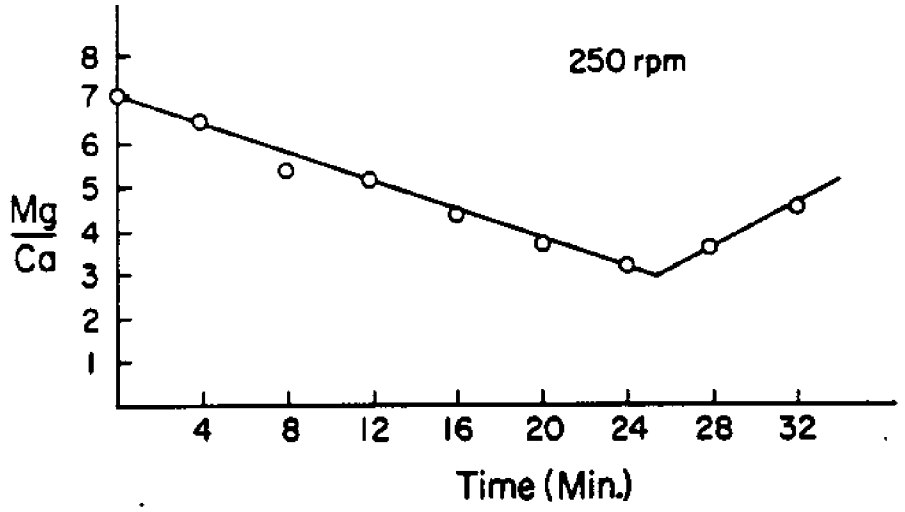

Fig.III c.14

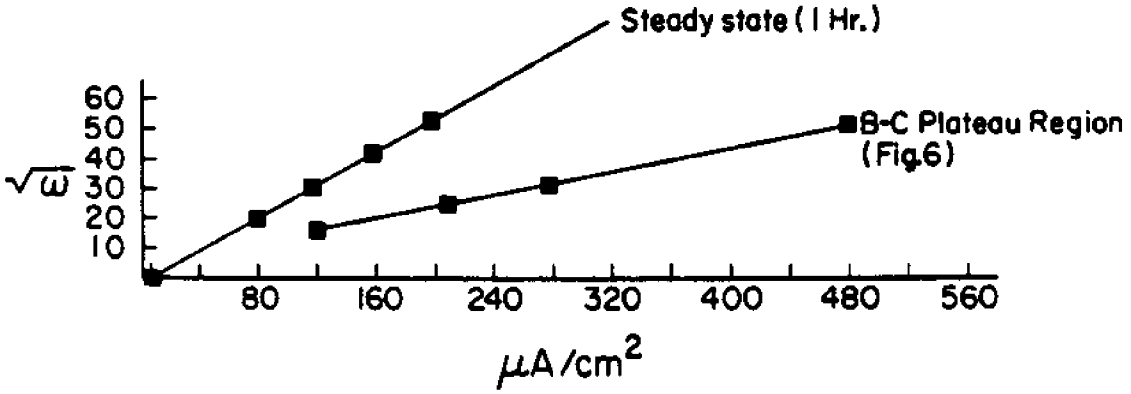

Fig.III c.15

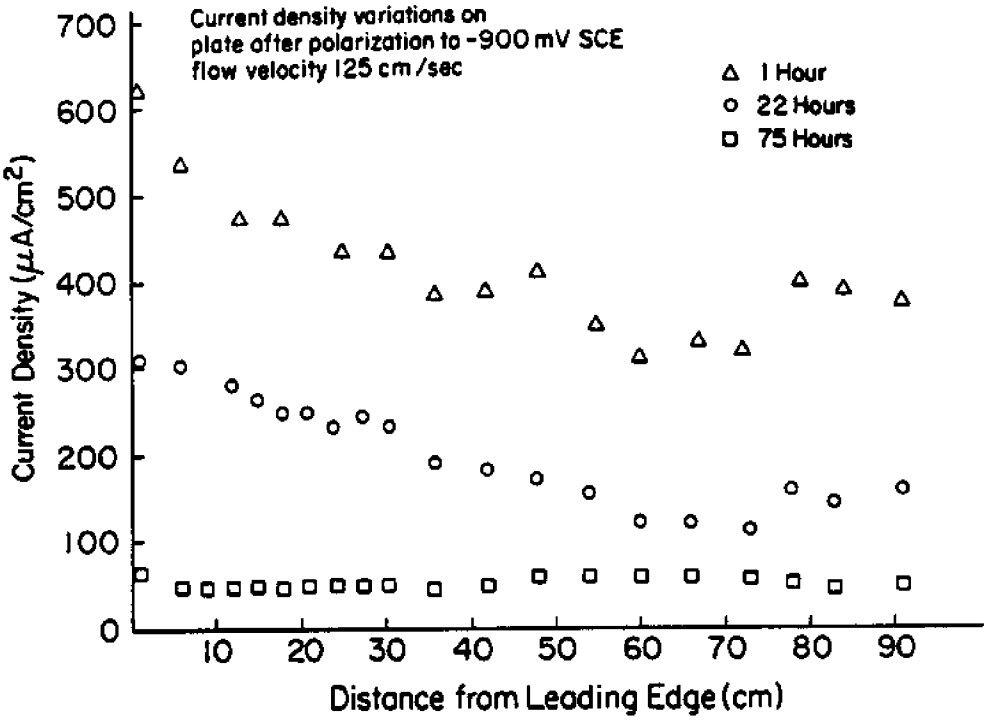

Fig.III c.16

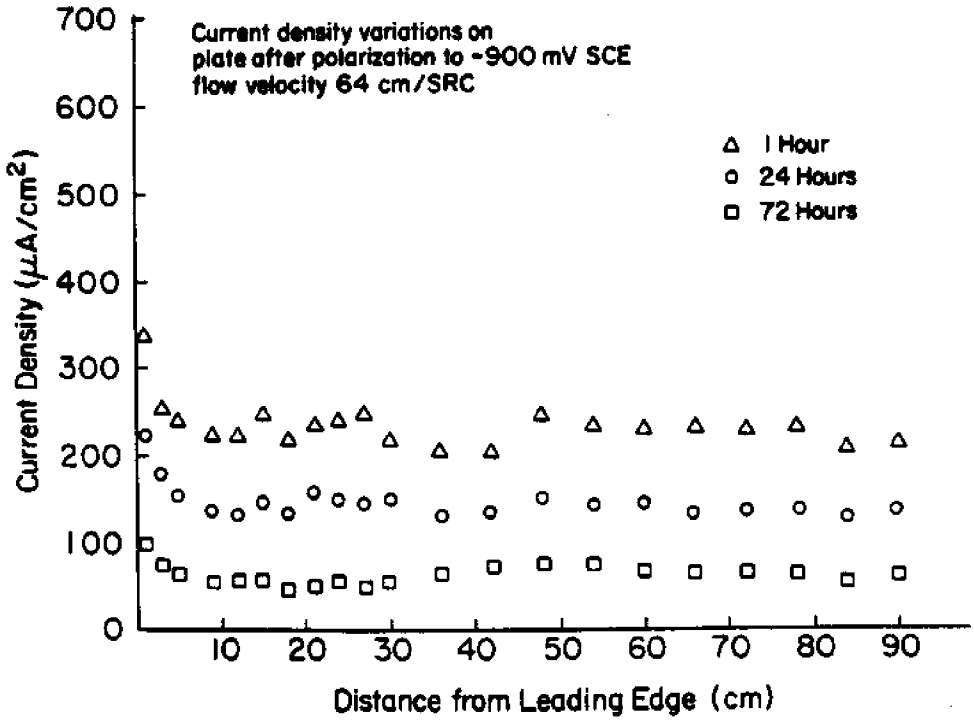

Fig.III c.17

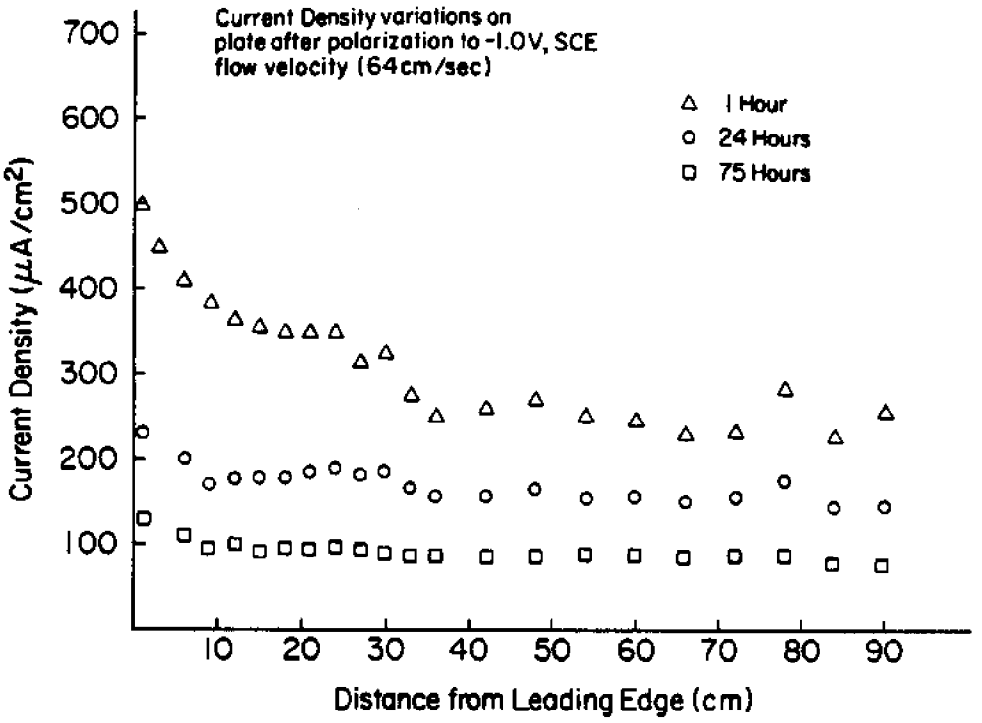

Fig.III c.18

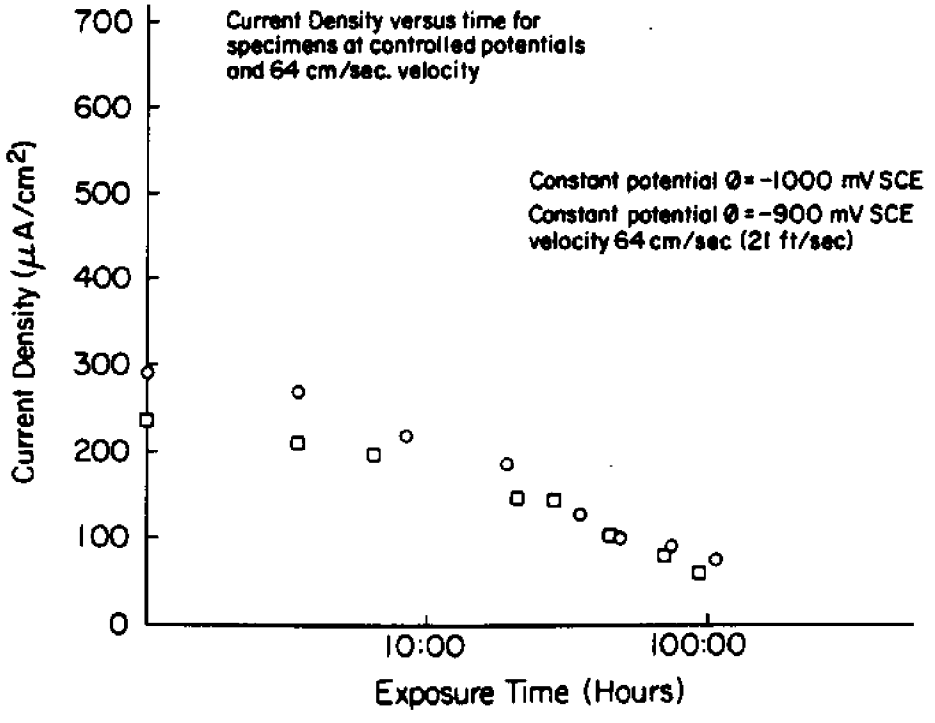

Fig.III c.19

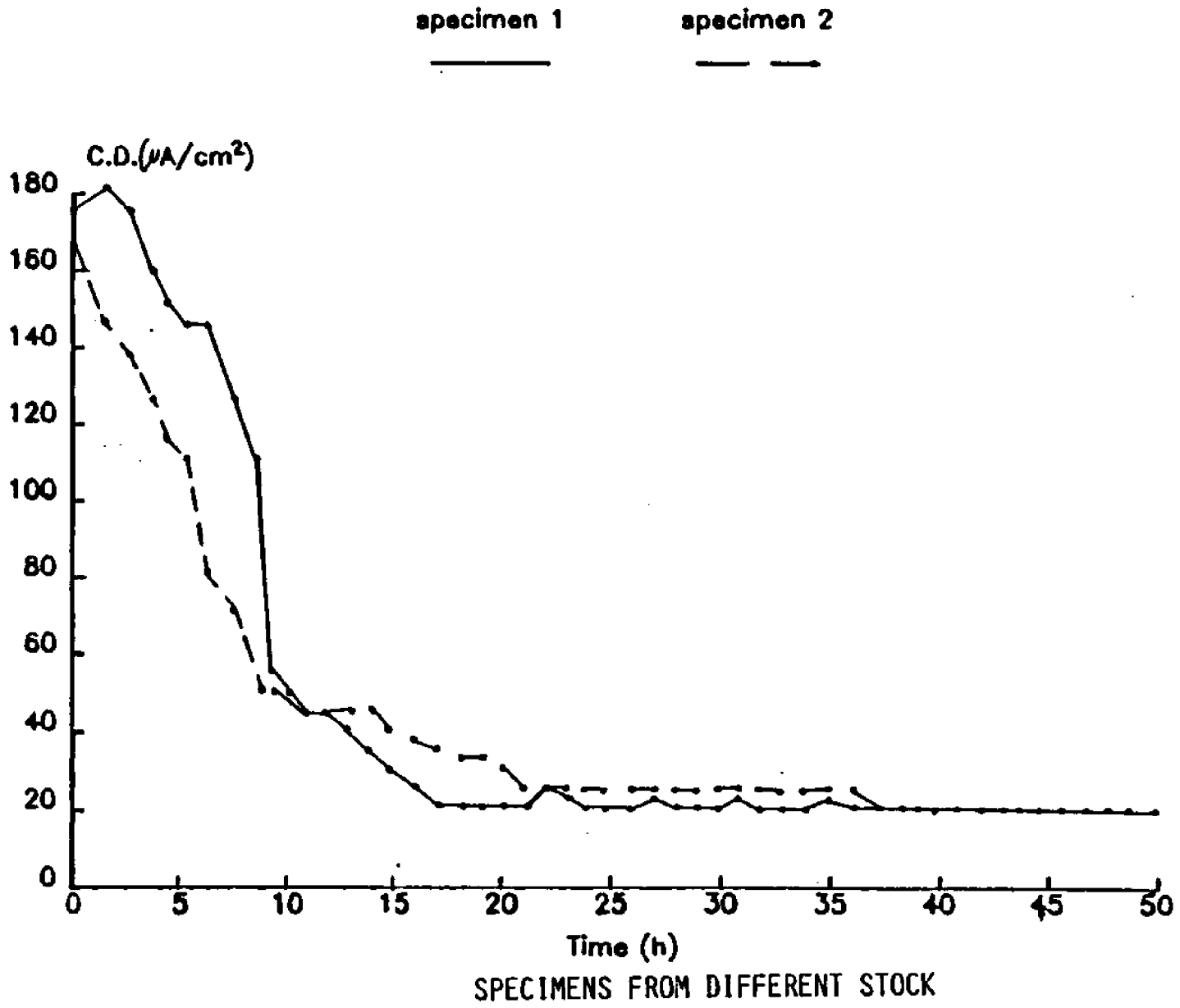
specimen 1
specimen 2
C.D.(μA/cm²)
180
160
140
120
100
80
60
40
20
0
0
5
10
15
20
25
30
35
40
45
50
Time (h)
SPECIMENS FROM DIFFERENT STOCK

FIG. III.D.1

III.F. DEPOSIT FORMATION WITHIN SIMULATED FATIGUE CRACKS

III.F. 1. Tests in 3.5% NaCl-Distilled Water. All of these experiments involved the lesser thickness (6.4 mm) specimen type. While variability in the results was encountered, still some general trends were apparent. Thus, Figures III.F.1 and III.F.2 illustrate the influence of cyclic frequency and velocity, respectively, upon potential profile within the simulated crack. While these data reflect a specific control potential of -0.780 volts (SCE), the same trends were apparent at other potentials as well. Thus, as a general rule plots of potential versus distance for data at different frequencies (Figure III.F.1) became more steep as frequency was increased, whereas plots for different velocities (Figure III.F.2) retained approximately the same III.F.2 slope. In most cases increasing velocity shifted potential within the crack to more noble (positive) values. Control potentials as negative as -1.100 volts were investigated, and it was determined that profile within the crack became more steep as potential was made increasingly cathodic.

Also apparent from these experiments was that potential within the simulated cracks varied sinusoidally with time such that potential was most positive when the crack was fully open and most negative when it was closed. Thus, periodicity of this variation was the same as for the fatigue cycle. The magnitude of applied current was also observed to vary with the same periodicity as the fatigue cycle, such that greatest current corresponded to maximum crack opening.

Of particular interest with regard to Figures III.F.1 and III.F.2 is deviation of the observed potential at the crack mouth from the control value. To investigate this a probe of the 0.25 mm ID Tygon tubing was employed to scan the potential profile on the boldly exposed specimen surface. Figure III.F.3 presents this data and reveals that, while the area of the specimen in close proximity to the reference electrode was maintained at or near the control potential, departures from this

prescribed value were apparent at more distant locations. This finding probably reflects the fact that the reference electrode was near the upper part of the specimen and was relatively remote to the region of the simulated crack. Because of this and the possibility that current density required at the crack region to maintain the prescribed potential differed in comparison to the overall, boldly exposed surface as described subsequently, the crack region may have been under at least partial galvanostatic control. While this was not intended in design of the experimental system, it may, in fact, more closely represent conditions which exist for actual marine structural systems than the potentiostatic control case. Possible explanations for the cyclic dependence of the magnitude of this depolarization are discussed subsequently. The data in Figure III.F.3 are for the crack in the most open position. These potentials also were periodic, such that a less severe profile was apparent when the crack was closed.

Also included in Figure III.F.3 are data for natural sea water. These exhibited the same trend as for the NaCl solution, but with less variation.

Tests in Sea Water. Figure III.F.4 illustrates typical current density versus exposure time behavior for simulated fatigue crack specimens in sea water for four cathodic potentials. While the initial current densities were ordered in proportion to the magnitude of polarization, as should be anticipated intuitively, the same was not the case once steady state was achieved. Presumably, the long-time current densities reflect the electrical resistance of the calcareous deposit, as the data of Klas (1958) has suggested. If this was the case, then the surface film formed at -0.900v. (SCE) was relatively unprotective and the steady-state current density to maintain this potential abnormally high. While the data in Figure III.F.4 probably reflect an influence of complex potential-current response of the simulated crack region, in all probability this introduced a relatively small departure of this data from what would result for smooth specimen (no simulated crack) tests.

This conclusion is based upon the fact that the reference electrode employed for potential control was relatively remote to the simulated crack region of the specimen. The fact that previous results (Wolfson et al, 1981) employing a different type of specimen also encountered the current decay trends in Figure III.F.4 support this contention.

The current density for tests in sea water was periodic in the same sense as described above for the 3.5% NaCl-distilled water experiments. In the sea water case, however, the amplitude of this variation decreased during the course of the exposure and was no longer detectable by the time the current density achieved steady state.

Figure III.F.5 is a SEM micrograph of the calcareous deposits formed on the boldly exposed surface of one of the present test specimens. EDAX analysis revealed that the predominant cation comprising this was calcium and that little or no magnesium was present. Deposits on boldly exposed surfaces at other potentials (either -0.900 or -1.000v. SCE), frequencies and nominal velocities were essentially the same. Hence, no distinction in the deposit formed upon specimens polarized at -0.900v. in comparison to that developed at other potentials was apparent for the magnifications employed.

The current density to maintain a prescribed potential in sea water was invariably less than in 3.5% NaCl-distilled water, presumably due to presence of the calcareous deposit in the former case. Figure III.F.6 illustrates this where cathodic polarization curves have been developed from the steady-state current densities to maintain the prescribed potentials in the above experiments. Data for specimens polarized in the NaCl solution at cyclic frequencies of 0.5 and 1.0 Hz., in addition to 0.1 Hz, revealed a trend whereby the cathodic polarization curve was shifted to higher current density with increasing frequency, although the effect of frequency was not as pronounced as in the case of current density changes that resulted from differences in nominal electrolyte velocity (Figure III.F.6)

Potential profiles in Figure III.F.7 (-0.780v.) appeared to be steeper in NaCl than sea water. At -1.000v. (Figure III.F.8) the profile near the crack mouth was particularly severe in NaCl and almost non-existent in sea water. In view of the relatively small potential variations (0.020-0.025v. maximum) which were apparent there, it cannot be concluded that differences in potential profile trends with electrolyte chemistry are significant. Considering, however, that they are, it may be reasoned that the profile developed in a particular case should be influenced by the following factors:

1. The net current available to the crack vicinity. This should be determined by the overall current demand for the specimen, geometry of the specimen and, hence, the degree of potentiostatic versus galvanostatic control, as determined by IR (voltage) drop considerations.

2. Polarization resistance of the material. This should be influenced by oxygen availability at the steel-electrolyte interface. Locally high hydrodynamic flow resulting from the cyclic ejection-ingestion of electrolyte may be influential here.

3. Calcareous deposit formation. This, in fact, may be important as it influences 1) and 2). For example, current density, effective exposed surface area and oxygen availability should be effected by these surface films.

III.F.2 Tests in Sea Water - 25.4 mm Specimens. Figures III.F.9 and III.F.10 present current density decay plots for the 25.4 mm thick simulated fatigue crack specimen, where the magnitude of nominal external surface polarization was -1.000 and -0.780v. (SCE), respectively. The current density data is reported at any time as a maximum and minimum value in accordance with a cyclic variation of this parameter with time.

The former (maximum current density) corresponded approximately to the most open position of the simulated crack, whereas the latter or minimum current density occurred with the crack near the most closed position. Frequency for the cyclic current density variation was the same as for the crack opening and closing. The generalized current density decay trend for this data was similar to what has been reported previously for steel specimens of various geometries cathodically polarized in sea water (Wolfson, et al, 1981). This has been related to accumulation with time of calcareous deposits and resultant oxygen concentration polarization.

Correspondingly, Figures III.F.11 and III.F.12 illustrate potential profile within the simulated crack for the above two levels of polarization. Analogous to the situation described above for current density potential within the crack also exhibited a cyclic time dependence of the same frequency as the crack opening and closing; and each of these two extremes are plotted in the above figures. Similar to what was reported above for 6.4 mm thick specimens potential within the crack was most positive when the crack was near its maximum open position and most negative when near the closed position. This trend in both the current density and potential data suggests greater current demand to maintain a prescribed potential within the simulated crack during the opening phase of the cycle, as opposed to closing. This behavior is attributed to enhanced availability of dissolved oxygen at the crack surface-electrolyte interface during the opening as contrasted with the closing phase of cyclic motion. It is projected that this resulted from ingestion into the crack of some aerated bulk solution during opening and consumption of oxygen thereafter. The generalized decrease in current density with exposure time has been attributed to formation of calcareous deposits and resultant oxygen concentration polarization. The possibility of at least partial galvanostatic, as opposed to potentiostatic, control within the simulated crack may also be important.

Examination of the simulated crack faces of specimens polarized to -0.780v subsequent to one week testing revealed a band of corrosion product positioned approximately 2-6 mm in from the crack mouth and extending the width of the specimen. Figure III.F.13 is a photograph illustrating this. The rust extended from this band to the mouth of the crack and even onto the external surface. However, the corrosion per se seemed to be limited to the relatively narrow region within the crack. This same corrosion was also apparent for the 6.4 mm specimens, as shown by Figure III.F.14.

An interesting aspect of the potential profile data (Figures III.F.11 and III.F.12 was occurrence of a peak approximately 4 mm in from the simulated crack mouth. This was observed for each of the two potentials investigated; however, these relatively positive potentials were noted only for the data with the crack in the most open position and these values became increasingly negative as the experiment progressed. Presence of the corrosion band within the simulated crack of the specimen polarized to -0.780v. was probably due to the relatively positive potential (~ -0.72v.) which existed here initially in conjunction with the peak in the potential profile data. No corrosion was observed in the case of the -1.000v. specimen, however, presumably because even the most positive potential was negative to the minimum value required to cause corrosion.

An important facet of rationalizing the potential data in Figures III.F.11 and III.F.12 involves determination of current density profile within the simulated crack; however, experiments have not yet been performed to accomplish this. At the more negative potential (-1.000v) a portion of the current density was probably associated with the hydrogen reduction reaction and the remainder with oxygen reduction. At the more positive potential (-0.780v.) the latter reaction alone should be involved. In either case, however, oxygen availability at the crack surface-electrolyte interface and along the length of the crack should be an important parameter in rationalizing the experimental observations.

While mass transport within static stress environmental cracks is expected to occur mostly by diffusion, convective mixing should also be important for applications involving cyclic stresses. For the latter situation (environmental fatigue) it may be reasoned that there are two determinants in rationalizing the concentration and distribution of various species in the crack electrolyte. The first of these pertains to mass transport conditions which are established within the crack itself in response to the cyclic ejection-ingestion process and the second to the extent of mixing (convective and diffusional) between the crack and bulk solutions as the former exits from and reenters the occluded cell on each cycle. With regard to the former (mass transport within the crack) it may be reasoned that both convective and diffusional mixing could be important for a cyclic crack electrolyte ejection-ingestion process that results in laminar flow, since ion migration is expected to be the predominant transfer mechanism normal to flow lines (perpendicular to the crack walls). However, movements parallel to streamlines (along the length of the crack) should be significantly enhanced by convection compared to the case where diffusion alone occurs. In situations where the ejection-ingestion flow is turbulent, however, mass transfer by convective mixing is expected to totally dominate that by diffusion in both directions (normal and parallel to the crack faces). No studies have been undertaken to define those conditions for which crack electrolyte flow is turbulent and where it is laminar.

Analyses performed to date with regard to the second determinant, crack electrolyte-bulk electrolyte mixing as the former is ejected from and ingested into the crack on each cycle, have assumed that such interchange is complete on each cycle, and so the chemistry of solution entering the crack is always the same as the bulk (Turnbull, 1980 and 1981). The motivation for this is derived from the relative simplification of the problem that results; however, it must be recognized that such a situation occupies but one end of a spectrum which extends

from complete mixing of electrolytes on each cycle to no mixing. An initial analysis of crack electrolyte-bulk electrolyte mixing has been performed (Hartt, 1978), which considers convective interchange alone and that such mixing occurs in proportion to momentum of the ejected-ingested electrolyte; and it was proposed that such mixing may be represented by Equation I.11.

The above comments are explicitly applicable to the present experimental results where several projections can be made. The first pertains to the likelihood that crack electrolyte-bulk electrolyte mixing on each cycle was not complete. Intuitive arguments may be given that this may be the case for any fatigue process with $R > 0$. In addition, the modest polarization profile within the simulated cracks (Figures III.F.11 and III.F.12) despite periodic, locally high electrolyte velocities suggests a relatively low oxygen availability compared to the concentration of this species in the bulk solution. Also, the experimental results indicate that oxygen availability within the crack was greatest during the ingestion phase of each cycle and decreased thereafter. This rationale indicates the difficulty of developing a model for current density profile within fatigue cracks and, in fact, leads to a conclusion that such information must at this time be obtained experimentally.

Second, it is projected that calcareous deposit formation rate within fatigue cracks which are cathodically polarized in sea water should be influenced by a) local current density, b) local velocity, c) crack electrolyte pH and pH profile normal to the metal surface and d) replenishment rate of ions involved in the precipitation reactions from interchange between the crack and bulk solutions. The significance of these factors in perspective of the preceding comments regarding potential and current distribution within cracks should be readily apparent. On the one hand the fact that current density within the occluded cell is low compared to the boldly exposed faces suggests that the pH increase for the former region may be modest. However, this may be offset by lack of replenishment (mixing) from the bulk solution. Locally high velocities within the crack itself

may serve not so much to lower surface pH but instead to compromise pH profiles such that pH of the entire crack electrolyte may be relatively uniform and high. This could lead to different chemistry, morphology and properties for deposits found within cracks, as opposed to those which occur on boldly exposed surfaces, in accordance with formation kinetics dictated by a) - d) above.

III.F.3 Rationalization of Potential Profiles. An analytical evaluation of the potential distribution within simulated fatigue cracks of the present experiments has been performed. This was based upon the crack geometry illustrated in Figure III.F.15. Thus, the potential profile is projected to be determined by 1) the net current entering the crack 2) IR drop along the crack and 3) polarization resistance. The charge conservation criterion requires that

$$I_x = I_{x+\Delta x} + 2dI_n; \qquad \text{(III.F.1}$$

where the various current density terms have been defined in Figure III.F.15. From Ohm's Law

$$I_x = k\delta_x \frac{d\phi}{dx}, \qquad \text{(III.F.2}$$

where k is specific conductivity and the crack width is unity. Similarly, the relationship between current and potential at x + Δx is

$$I_{x+\Delta x} = k\delta_x \left[\frac{d\phi}{dx} + \Delta x \frac{d^2\phi}{dx^2}\right]. \qquad \text{(III.F.3}$$

From Figure III.F.15 it may be reasoned that

$$\delta_{x+\Delta x} = \delta_x - 2\alpha\Delta x, \qquad \text{(III.F.4}$$

which upon substitution into III.F.3 yields

$$I_{x+\Delta x} = -k\delta_x\frac{d\phi}{xdx} - k\delta_x\frac{d^2\phi}{xdx^2}\Delta x + 2\alpha k\Delta x\frac{d\phi}{dx} + k\alpha\Delta x^2\frac{d^2\phi}{dx^2}. \quad \text{(III.F.5}$$

By neglecting the higher order term and considering that $dI_n = I_n\Delta x$, Equation III.F.1 can be reevaluated as

$$-k\delta_x\frac{d\phi}{xdx} = -k\delta_x\frac{d\phi}{xdx} - k\delta_x\frac{d^2\phi}{xdx^2}\Delta x + 2\alpha k\Delta x\frac{d\phi}{dx} + 21_n\Delta x. \quad \text{(III.F.6}$$

Simplifying and rearranging yields

$$\frac{d^2\phi}{dx^2} = \frac{2\alpha}{\delta_x}\frac{d\phi}{dx} + \frac{2}{k\delta_x}I_n. \quad \text{(III.F.7}$$

Based upon the geometry in Figure III.F.15 the relationship

$$\frac{2\alpha}{\delta_x} = \frac{1}{(0.635 - x)} \quad \text{(III.F.8}$$

is apparent, and so

$$\frac{d^2\phi}{dx^2} = \frac{1}{(0.635 - x)}\frac{d\phi}{dx} + \frac{F(\phi)}{k\alpha(0.635 - x)}, \quad \text{(III.F.9}$$

where $F(\phi) = I_n$ conforms to the applicable cathodic polarization curve. The problem thus involves solving Equation III.F.9 for potential as a function of distance into the crack. This was accomplished by transforming the equation to a set of n simultaneous, first-order differential equations and applying n Runge-Kutta formulae (James, 1977). Accordingly, Equation III.F.9 was rewritten as

$$\frac{dv}{dx} = \frac{v}{(0.635 - x)} + \frac{F(\phi)}{k\alpha(0.635 - x)} \text{ and} \qquad \text{(III.F.10}$$

$$\frac{dv}{dx} = v. \qquad \text{(III.F.11}$$

These were solved numerically using the Runge-Kutta technique, whereby .

$$\phi_{i+1} = \phi_i + hv_i + \frac{h}{6}(k_i + k_2 + k_3) \text{ and} \qquad \text{(III.F.12}$$

$$v_{i+1} = v_i + \frac{1}{6}(k_1 + 2k_2 + k_3 + k_4), \qquad \text{(III.F.13}$$

where

i and i + 1 indicate successive steps in the iteration process,

h is the increment in x and

k_1, k_2, k_3 and k_4 are given by the expressions

$$k_1 = hf\{x_i, \phi_i, v_i\}$$

$$k_2 = hf\{x_i + h/2, \phi_i + \frac{h}{2}v_i, v_i + \frac{k_1}{2}\},$$

$$k_3 = hf\{x_i + \frac{h}{2}, \phi_i + \frac{h}{2}v_i + \frac{h}{4}k_1, v_i + \frac{k_2}{2}\} \text{ and}$$

$$k_4 = hf\{x_i + h, \phi_i + hv_i + \frac{h}{2}k_2, v_i + k_3\}$$

for which $f = \frac{dv}{dx}$ (Equation III.F.10)

Inputting appropriate values for the parameters x_o, ϕ_o and v_o (the latter was assumed to be zero) and for $F(\phi)$ permitted the potential profile to be calculated. The latter parameter [$F(\phi)$] was defined according to the appropriate ϕ-i curve in Figure III.F.6, and this was represented mathematically in Equation III.F.9 by a cubic expression. Figure III.F.16 presents the results of this analysis in comparison to some of the data presented previously. This reveals not only a large difference between the analytically developed potential profiles and the experimental data but also a reversal in trend between the two. This is evidenced by the fact that the experimental data indicate that potentials are more positive with the crack open than closed, whereas Equation III.F.9 projects the opposite. The analytical results are intuitively realistic, in that they are consistent with presence of an IR drop along the relatively narrow confine of the simulated crack. The observation that the data did not conform to this trend suggests that some factor promoted polarization within the crack and that this was more dominant than IR drop, particularly with the crack in the most closed position. If one considers that the model, although simplistic, is a reasonable representation of the simulated crack potential distribution, then the most likely explanation for the distinction between the experimental and analytical results is inappropriateness of the assumed $F(\phi)$ term in Equation III.F.10.

An important factor with regard to rationalizing the experimental data (Figures III.F.1, III.F.2, III.F.7 and III.F.8) and analytical treatment (Equation III.F.9) may be dissolved oxygen concentration of the crack electrolyte. In all likelihood the concentration of this species was below that of the bulk solution, first, since reactions within the crack consumed oxygen and, second, because interchange between that portion of the crack electrolyte ejected on each cycle and the bulk solution was probably not complete. Turnbull (1980, 1982) has performed an indepth treatment of this problem and has calculated oxygen concentration profiles within corrosion fatigue cracks. Assumptions in this analysis were that, first, crack

electrolyte-bulk electrolyte interchange during each cycle was complete and, second, that kinetics of the oxygen reduction reaction were under activation polarization control. Assuming, however, that the crack electrolyte was air saturated and that current density upon the crack faces corresponded to nominal steady state values measured during the course of the experiments (Figure III.F.6), it was calculated that oxygen depletion should result in from two to five seconds. Also, based upon consideration of the crack geometry, twenty percent of the electrolyte was retained in the crack at maximum closure; and it is anticipated that this solution was not available for convective mixing with the bulk. Hence, it may be that oxygen concentration within these simulated cracks was, at least in some locations, less than the bulk solution value. This would result in low polarization resistance which, in turn, contributed to the relatively flat potential profiles in Figures 3.G.1 and 3.G.2. The observation that in some instances (for example, the sea water data in Figure III.F.1) potential became slightly more negative with increasing crack depth may also be indicative of this.

A second attempt to analytically evaluate potential profile within the simulated cracks was performed based upon reduced oxygen concentration in this local region. Thus, in the previous evaluation the $F(\phi)$ function considered that a current density of 14.5 x 10-2 mA/cm2 was required to polarize the crack face to -0.780v (Figure III.F.6). Figure III.F.17 reproduces the analytical results and experimental data for the crack closed case from Figure III.F.16. In addition, a second analytical curve is presented based upon Equation III.F.10 and a current density of 0.3 mA/cm2 to polarize to -0.780v. Upon correcting this curve to the depolarized crack mouth potential (approximately -0.776v.) it is seen that the predicted and experimental potential profiles are in excellent mutual agreement. Thus, it may be that because of relatively limited oxygen concentration in the crack electrolyte polarization

resistance was low and the crack faces were readily polarized. At the same time the fact that current density was low precluded occurrence of significant IR drop.

The experimental observation that potential within the crack was most positive when the crack was fully open may be explained in terms of cyclic variations in dissolved oxygen availability and the probability that the crack vicinity was under at least partial galvanostatic control. Thus, it may be reasoned that oxygen content of the crack electrolyte was greatest during ingestion or at maximum crack opening. Hence, it is not unexpected that potential at this time would be most positive. In the case of the variable frequency results (Figure III.F.1) potential profile was increasingly steep the higher the frequency. This may be due to the fact that at higher frequency 1) less time was available during each cycle for oxygen depletion within the crack and 2) convective mixing during the ejection-ingestion process should have been more complete. Note, however, that for much of the data (Figures III.F.2, III.F.7 and III.F.8) the potential profiles with the crack open and closed were essentially parallel to one another and the value differences reflect variations of potential at the crack mouth. Data for this latter location also indicate greater departure from the prescribed, control value for the crack open as opposed to closed. This is consistent with the earlier projection that electrolyte in this vicinity should be of greater oxygen concentration during ingestion as opposed to ejection.

An indication of the relative magnitude of ejection-ingestion flow was apparent from observation of calcareous deposits on the external surface adjacent to the crack. Thus, Figures III.F.18 and III.F.19 are scanning electron micrographs of specimens cycled for two weeks in flowing sea water and polarized to -1.000v. Frequency in the former case was 0.1 Hz and in the latter 1.0 Hz. Both micrographs are for the external surface adjacent to the crack. Note that for the lesser frequency an area relatively void of deposits existed within about 0.05 mm of the crack mouth. At 1.0 Hz this region extended

for more than 4.5 mm. Apparently, the flow that developed at 0.1 Hz was sufficient to mitigate significant deposit formation only in the immediate vicinity of the simulated crack mouth, and at 1.0 Hz this flow compromised deposit formation over a much broader area.

FIGURE CAPTIONS (Section III)

Figure III.F.1: Potential profile within a simulated fatigue crack in 3.5% NaCl for three frequencies. Nominal electrolyte velocity was 1.6 mm/sec.

Figure III.F.2: Potential profile within a simulated fatigue crack in 3.5% NaCl for three electrolyte velocities. Frequency was 0.1 Hz.

Figure III.F.3: Potential profile in the vertical direction on the external specimen surface, as determined by a 0.25 mm ID probe.

Figure III.F.4: Plot of current density versus exposure time for simulated fatigue crack specimens at four cathodic potentials.

Figure III.F.5: Scanning electron micrograph of calcareous deposits formed on the boldly exposed surface of a simulated fatigue crack specimen. 1100 X.

Figure III.F.6: Cathodic polarization curves for simulated fatigue crack specimens as developed from the steady state current density to maintain a prescribed potential.

Figure III.F.7: Comparison of the potential profile in sea water and 3.5% NaCl where the control value was -0.780v.

Figure III.F.8. Comparison of the potential profile in sea water and 3.5% NaCl where the control value was -1.000v.

Figure III.F.9. Current density decay for 25.4 mm thick simulated fatigue crack specimen polarized to -1.00v.

Figure III.F.10. Current density decay for 25.4 mm thick simulated fatigue crack specimen polarized to -0.78v.

Figure III.F.11. Potential profile within simulated fatigue crack at different exposure times for external surface polarized to -1.00v.

Figure III.F.12: Potential profile within simulated fatigue crack at different exposure times for external surface polarized to -0.78v.

Figure III.F.13: Corrosion product band extending across surface of simulated crack face from the 25.4 mm thick specimen.

Figure III.F.14: Photograph of simulated crack face after fatigue of one week in sea water at 0.1 Hz and -0.780v.

Figure III.F.15: Assumed crack geometry as applicable to the analytical evaluation of the potential profile within simulated fatigue cracks.

Figure III.F.16: Comparison of analytical and experimental results where the $F(\phi) = I$ relationship was taken as the appropriate cathodic polarization curve in Figure 6.

Figure III.F.17: Comparison of analytical results with experimental data for the crack closed situation, where it was assumed that current density within the crack was less than indicated by the appropriate polarization curve (Figure 6. The previous analytical result from Figure 16 is illustrated for comparison.

Figure III.F.18: Scanning electron micrograph of the boldly exposed surface of a simulated fatigue crack specimen. Note the region at the extreme upper right (near crack mouth) which is void of calcareous deposits. Frequency was 0.1 Hz. 190X.

Figure III.F.19: Scanning electron micrograph of the boldly exposed surface of a simulated fatigue crack specimen. Note the general absence of calcareous deposits. The crack mouth is just above the top of the photograph. Frequency was 1.0 Hz. 20X.

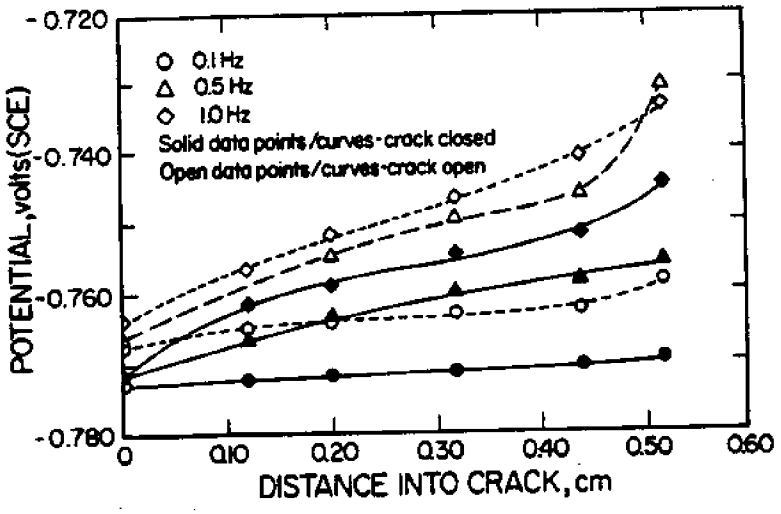

Figure III.F.1

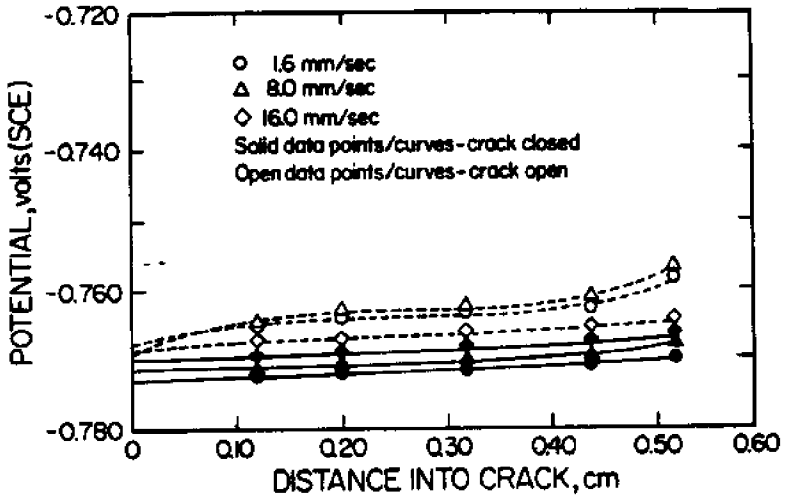

Figure III.F.2

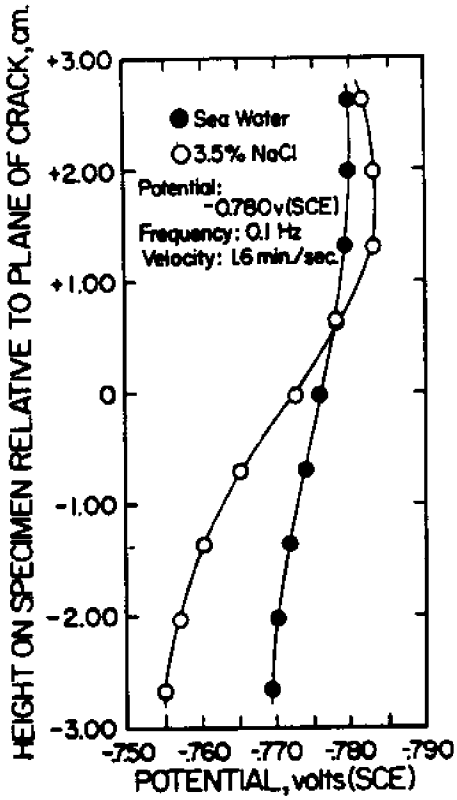

Figure III.F.3

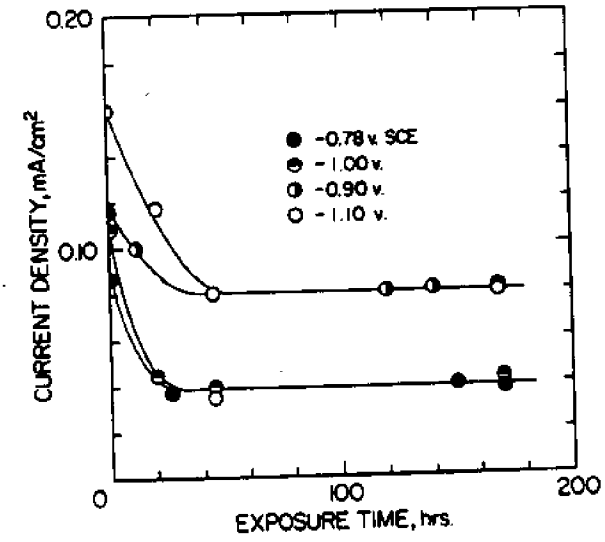

Figure III.F.4

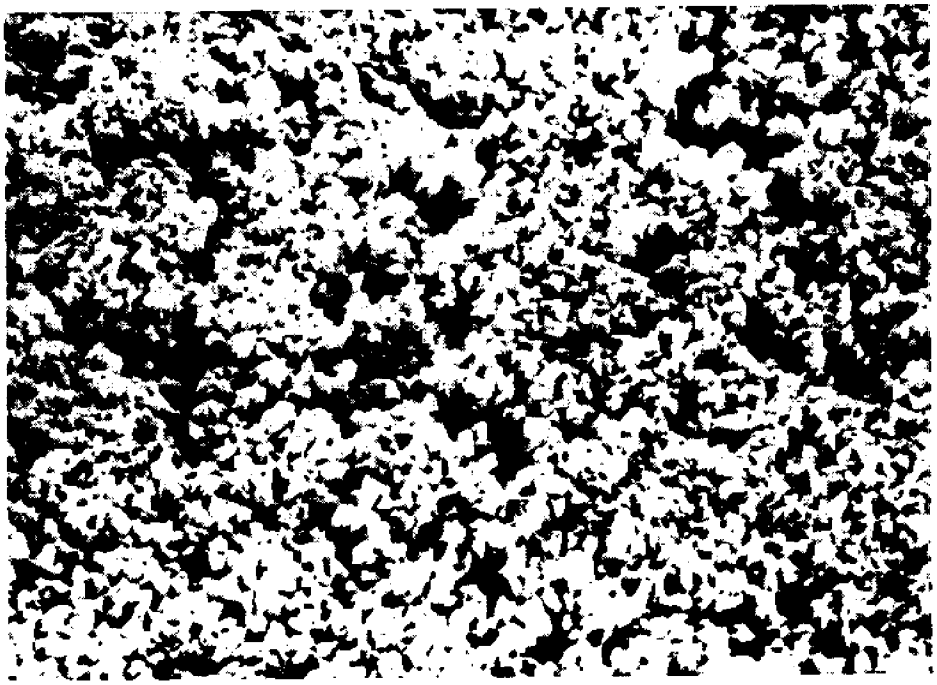

Figure III.F.5

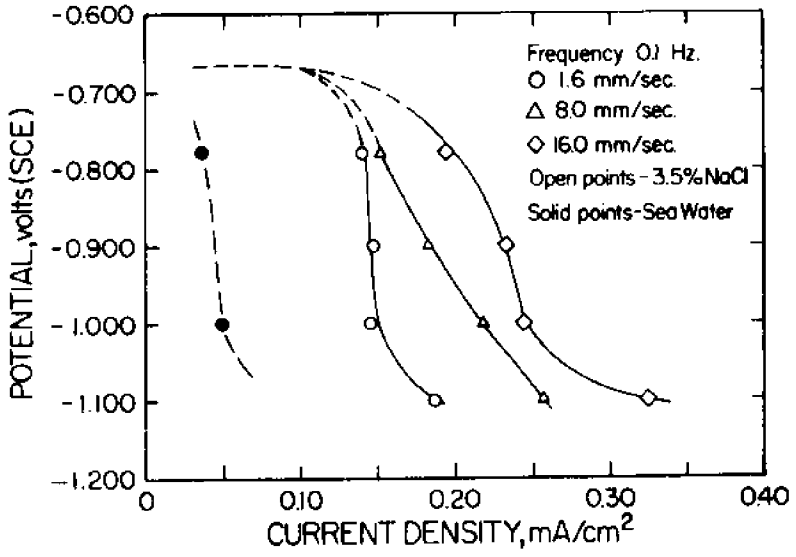

Figure III.F.6

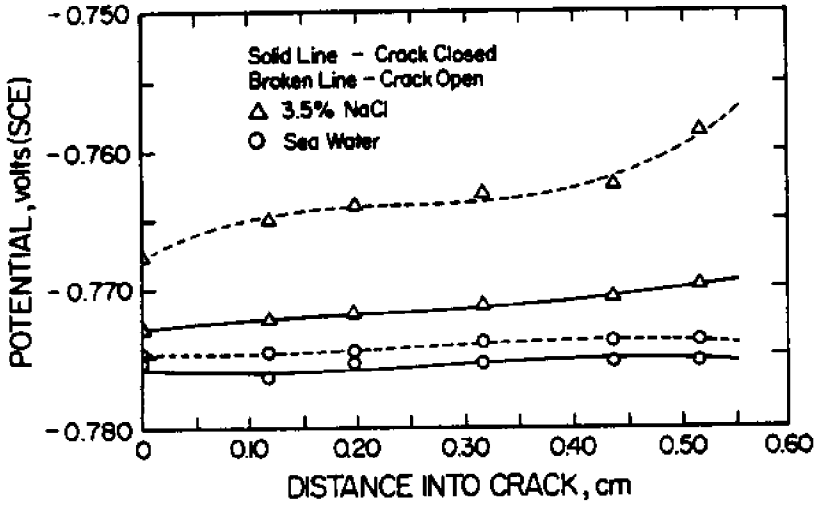

Figure III.F.7

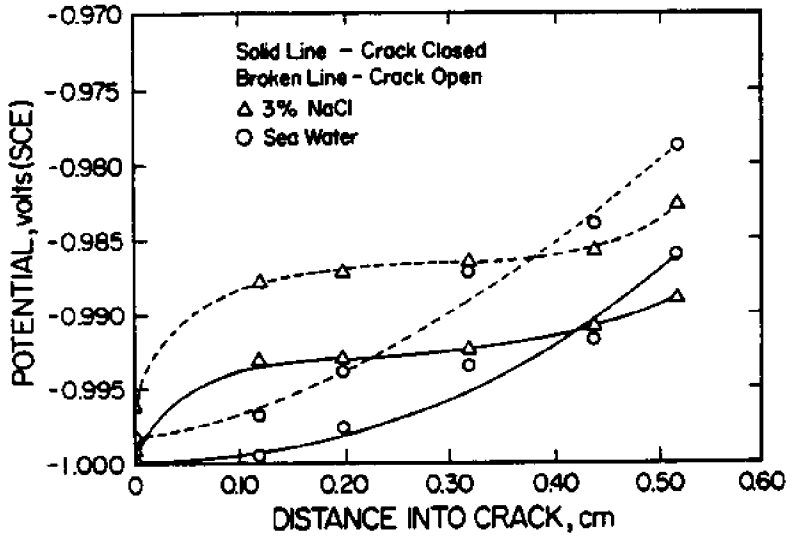

Figure III.F.8

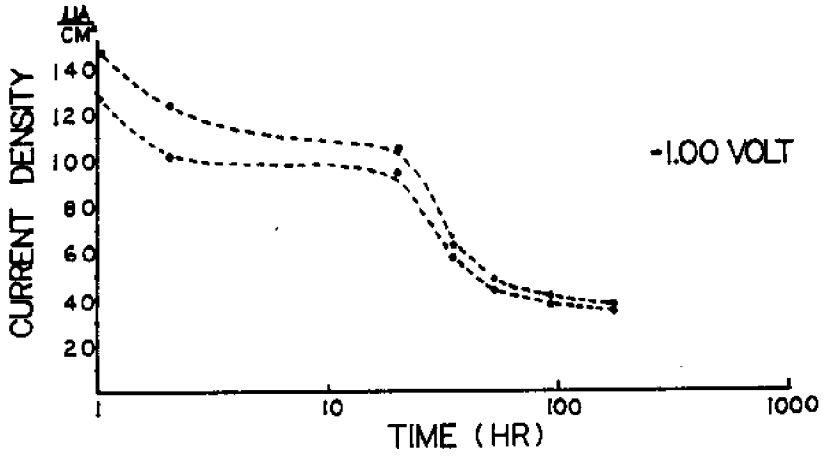

Figure III.F.9

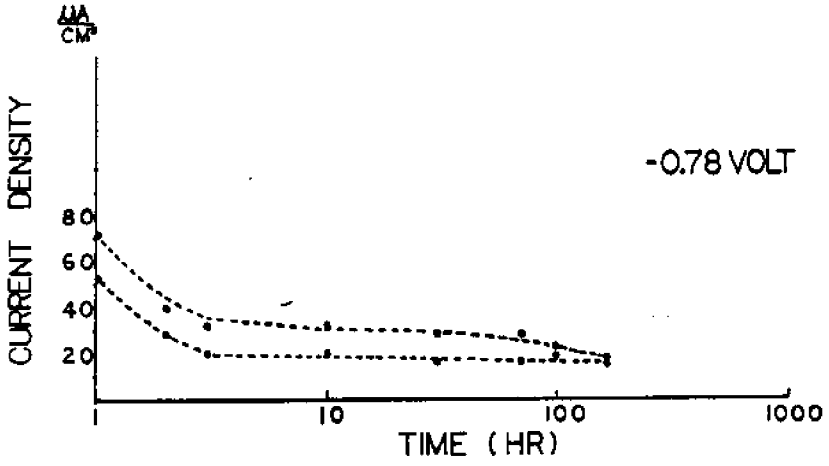

Figure III.F.10

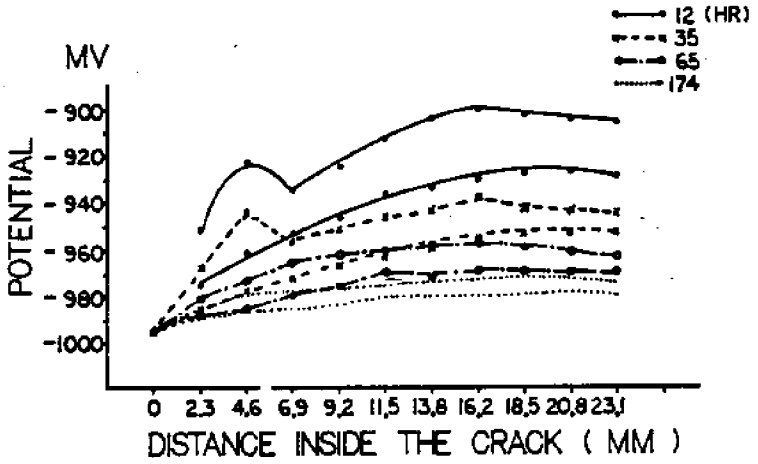

Figure III.F.11

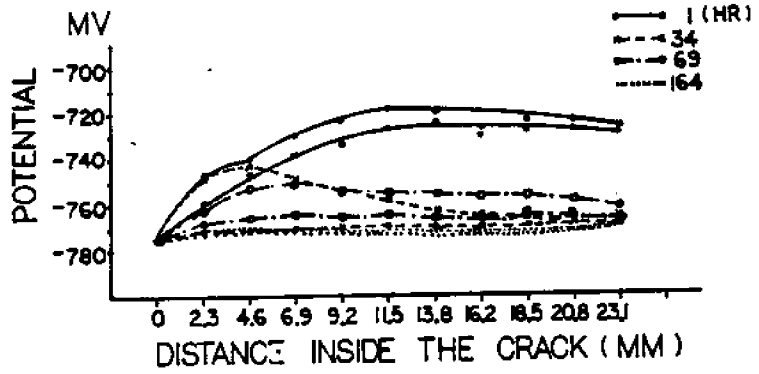

Figure III.F.12

Figure III.F.13

Figure III.F.14

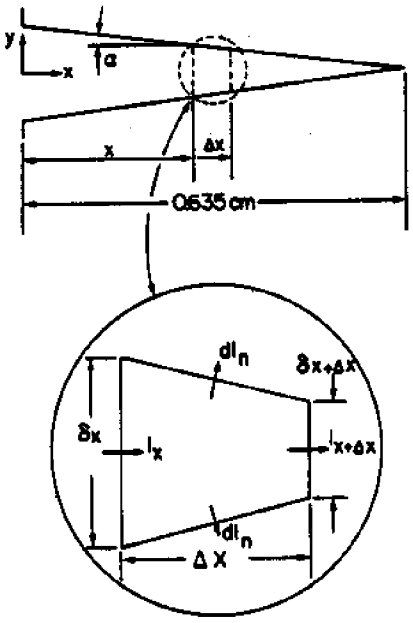

Figure III.F.15

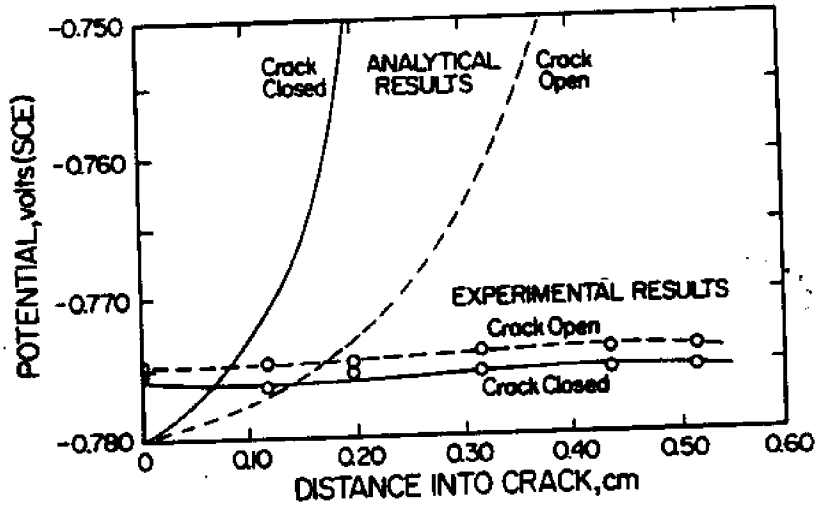

Figure III.F.16

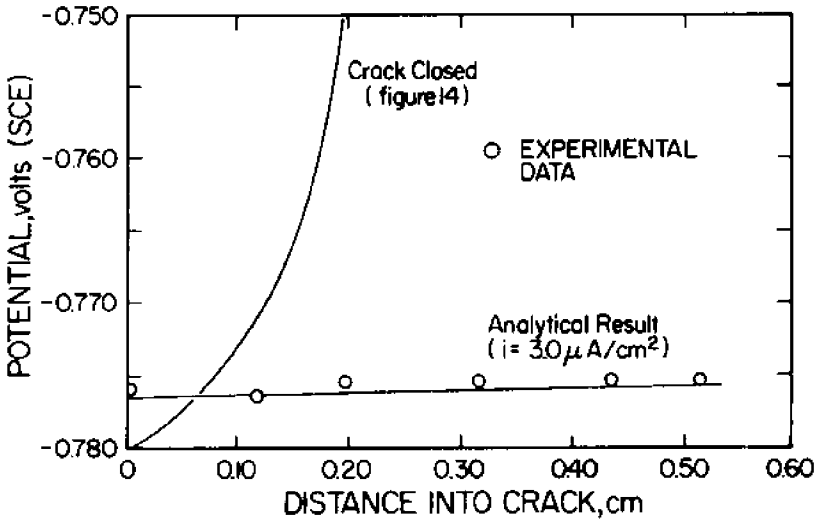

Figure III.F.17

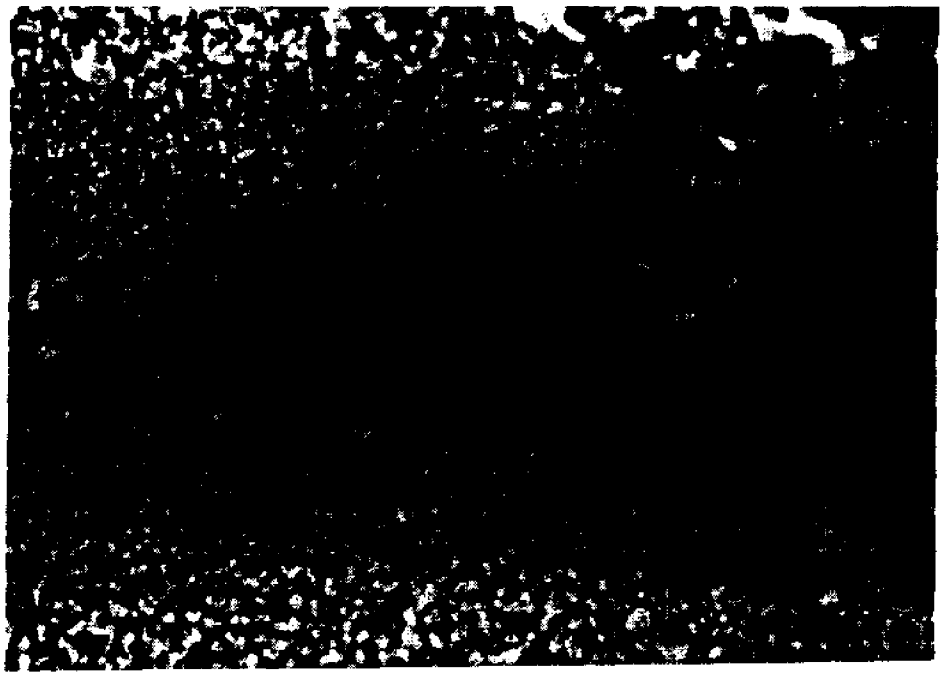

Figure III.F.18

Figure III.F.19